Jet Production at Hadron Colliders

by

Teppo T. Jouttenus

Submitted to the Department of Physics
in partial fulfillment of the requirements for the degree of

Doctor of Philosophy in Physics

at the

MASSACHUSETTS INSTITUTE OF TECHNOLOGY

June 2012

Author .....
Department of Physics
May 16, 2012

Certified by .....
Iain W. Stewart
Associate Professor
Thesis Supervisor

Accepted by .....
Krishna Rajagopal
Associate Department Head for Education

Jet Production at Hadron Colliders

by

Teppo T. Jouttenus

Submitted to the Department of Physics
on May 16, 2012, in partial fulfillment of the
requirements for the degree of
Doctor of Philosophy in Physics

Abstract

Hadronic jets feature in many final states of interest in modern collider experiments. They form a significant Standard Model background for many proposed new physics processes and also probe QCD interactions at several different scales. At high energies incoming protons produce beam jets. Correctly accounting for the beam and central jets is critical to precise understanding of hadronic final states at the Large Hadron Collider. We study jet cross sections as a function of the shape of both beam and central jets. This work focuses on measuring jet mass but our methods can be applied to other jet shape variables as well.

Measuring jet mass introduces additional scales to the collision process and these scales produce large logarithms that need to be resummed. Factorizing the cross section into hard, jet, beam, and soft functions enables such resummation. We begin by studying jet production at $e + e-$ collisions in order to focus on the effects of jet algorithms. These results can be carried over to the more complicated case of hadron collisions. We use the Sterman-Weinberg algorithm as a specific example and derive an expression for the quark jet function.

Turning to hadron colliders, we show how the N-jettiness event shape divides phase space into $N + 2$ regions, each containing one central or beam jet. Thus, N-jettiness works as a jet algorithm. Using a geometric measure gives central jets with circular boundaries. We then give a factorization theorem for the cross section fully differential in the mass of each jet, and compute the corresponding soft function at next-to-leading order (NLO). We use a method of hemisphere decomposition, which can also be applied to calculate N-jet soft functions defined with other jet algorithms.

Our calculation of the N-jettiness soft function provides the final missing ingredient to extend NLO cross sections to resummed predictions at next-to-next-to-leading logarithmic order. We study the production of an exclusive jet together with a Standard Model Higgs boson. Based on theoretical reasons and agreement between our calculation and data from the ATLAS collaboration, we argue that our results for the jet mass spectrum are a good approximation also for inclusive jet production and other hard processes.

Thesis Supervisor: Iain W. Stewart
Title: Associate Professor

Acknowledgments

I would like to thank my advisor Prof. Iain Stewart for all his work in helping me develop as a scientist. His guidance and example have been both helpful and inspiring. Most of the work in this thesis was done in collaboration with Dr. Frank Tackmann and Dr. Wouter Waalewijn and I am grateful for their help and support.

The Center for Theoretical Physics at MIT is a wonderful community and I wish to thank all of the staff, students, and faculty for helping to make my graduate studies an enjoyable and exciting experience.

Finally, I am indebted to my family, especially my parents Matti and Anne Jouttenus and my wife Maria. Their loving encouragement has kept me curious and helped me through those hard days that otherwise might have convinced me to give up. I hope to be able to love and support them as generously have done for me.

This work was supported by the Office of Nuclear Physics of the U.S. Department of Energy under the grant DE-FG02-94ER40818, and by an LHC Theory Initiative fellowship under the National Science Foundation grant PHY-0705682.

Contents

List of Figures

List of Tables

Chapter 1

Introduction

1.1 Searching for the Fundamental Laws

The question of how the world around us is put together has intrigued humans as far back as we have any records. The earliest known discussions about *atoms* or "indivisible particles" as the building blocks of matter come from ancient India and Greece around two and a half millennia ago. However, it was only during the past two centuries that chemistry and physics began to make headway in uncovering the fundamental structure of matter.

In the seventeenth and eighteenth centuries, chemists were able to isolate several different elements. It was subsequently observed that the elements always reacted in ratios of small integers. We can consider an example using two elements discovered early on, phosphorus and hydrogen. Phosphine is produced by mixing them in one-to-three ratio. If the elements are mixed in a ratio that is different from the required one, enough of the more abundant element will remain intact such that the amounts of elements participating in the reaction have the correct ratio. The atomic hypothesis sought to explain this fact by positing that each element consists of a unique type of atom and that different atoms combine to form molecules.

The patterns found in the properties of different elements led to the formulation of the periodic table where various atoms are ordered by their atomic weights and line up in columns characterized by similar chemical properties. The name atom proved to be a misnomer as it was discovered that atoms are not in fact indivisible. Their periodic properties follow from an internal structure, and it is possible to break atoms into their building blocks. The first building block to be isolated was the electron, discovered in

1897. Soon thereafter, it was shown that most of the mass of an atom is concentrated in a volume that is minuscule compared to the size of the atom itself. This massive core was named the nucleus and it was shown to carry positive charge. The lightest known nucleus was that of hydrogen, and in 1917 it was discovered that hydrogen nuclei can be extracted from the nuclei of other atoms. It was thus natural to assume that all nuclei are made up of hydrogen nuclei and later studies showed that the masses of all nuclei were indeed approximately integer multiples of the mass of the hydrogen nucleus. Since the hydrogen nucleus seemed to be a fundamental building block, it was given the name proton. The proton has an electric charge of same magnitude as the electron but with the opposite sign.

One problem with the model of building nuclei out of protons was that the total nuclear charge was always smaller than what it should be if the nucleus consisted of enough protons to produce the correct mass. It was proposed that the nucleus contained some electrons to cancel the charge of some of the protons.

Additional experiments with nuclei revealed a third building block in 1932—the neutron. It has approximately the same mass as the proton and received its name due to its lack of electric charge. It became clear that different nuclei are made up of a number of protons and neutrons. This model of the nucleus resolved several experimental puzzles that could not be explained if the nucleus were a collection of protons and electrons. After three and a half decades of intense research in the beginning of the twentieth century, physicists had uncovered the three matter particles that make up the atom: electron, proton, and neutron.

Knowing the building blocks of atoms, however, is not enough to understand the world around us. While studying the constituents of atoms, physicist were also exploring the ways that atoms stay together and interact with each other. The earliest theoretical attempts to understand the structure of the atom treated the nucleus as an immovable source of positive electric charge to which the negatively charged electrons were bound through the Coulomb interaction—the force that exists between any two charged objects. Experimentalists had discovered that the electrons in an atom occupied a discrete or quantized set of energy levels. Instead of being free to have any energy, they could choose only from a set of allowed values. In our macroscopic world this would correspond to an automobile that can only move at 10 mph, 20 mph, 30 mph etc. but not at any velocity between these values. The presence of energy levels could be explained by ascribing to electrons wave-like properties and describing bound electrons as standing wave-patterns around the stationary

nucleus. A familiar example of standing waves is the vibration of a guitar string. The length of the string determines the fundamental pitch of the plucked string, and plucking the string harder can only generate integer multiples of the fundamental frequency. The discrete energy levels of electrons could emerge as a consequence a similar restriction.

The theory that resulted from the observations of the energy levels of electrons in atoms and of other quantized phenomena is called quantum mechanics. It postulates that electrons and other matter particles have a wave-like nature. Despite being an approximate version of our modern understanding, it can explain the structure of atoms and molecules remarkably well [60]. It is possible to include the movement of nuclei in this early version of quantum mechanics but the detailed interactions holding the nucleus together were unknown and unaccounted for.

The energy levels of atoms can be detected most directly by observing that individual atoms emit light in a characteristic pattern of discrete wavelengths. Right after the turn of the century, it was postulated that light was also made up of discrete packets—or quanta—which were named photons. When an atom changes from one energy level to another, a photon is emitted or absorbed. These photons travel at a constant speed relative to any observer whether the observer is stationary or moving. The creation and annihilation of particles as well as movement at the speed of light are phenomena described by Einstein's theory of special relativity. The early version of quantum mechanics, which was developed to describe the energy levels of atoms, does not include such relativistic effects but it can be generalized to encompass them. This more inclusive theory is called quantum electrodynamics or QED.

QED takes as its starting point the concept of a field and postulates that fields can only interact locally. Local interaction means that the value of one field at a given location can only influence the values of other fields at that same location. The interaction of electrons and other charged particles over wide distances is explained in terms of the photon field. In the framework of QED, an electron is described as a localized disturbance in the electron field which can cause a disturbance in the photon field at the same location. The disturbance in the photon field then travels at the speed of light until it reaches another electron with which it interacts. In most situations, this complicated procedure of interacting field disturbances can be described sufficiently accurately by assuming that charged particles can interact with each other instantaneously over arbitrary distances. However, increasingly precise

measurements have validated the approach of QED as a more fundamental description of reality. We say that the interaction between charged particles is mediated by exchanging photons.

Unlike the classical fields of electromagnetism, these electron and photon fields have an inherently granular or quantized structure. They manifest themselves as a collection of quanta which in certain circumstances can be visualized as localized particles but at other times can be spread across a wide volume of space. The quantized fields of QED resolve the question of whether we should think of light and matter as waves or as particles. In fact, photons and electrons are neither. They are examples of a new kind of an object—a field quantum—which shares some familiar properties with waves and others with particles. Nevertheless, for the sake of clarity we shall use the term particle to refer to these objects.

The framework of QED puts photons and electrons—light and matter—on a more even footing: both are described as particles that can interact with each other. In order to preserve causality or the requirement that cause precedes effect, we must introduce a new particle called positron. It is the antiparticle of the electron and has all the same properties except that its electric charge has the opposite sign. Since the proton has a much larger mass than the electron, it was clear that the positron was something fundamentally different. QED can describe all processes involving photons, electron, and positrons to an amazing accuracy. However, it can do much more if we are willing to follow the approach of the early quantum theorists and include the nuclei as a collection of black boxes with known masses, charges, and a few other parameters that experimentalists had learned to measure. Combining QED and Newton's theory of gravity is sufficient to explain virtually all of our daily observations about the physical world in terms of the interactions of photons, electrons, positrons, and nuclei. However, the developers of QED knew that nuclei had an internal structure, and after the great success of explaining atomic structure with a self-consistent and predictive theory, they pressed on to explore the new challenges at the core of the atom.

Up to this point we have followed a broadly historical path through the discoveries of physics. In the interest of brevity, however, we shall proceed with a more selective approach since after the development of QED the pace of new discoveries becomes much faster. Our purpose is to introduce only those concepts that are helpful as context for the rest of this work.

The theory that emerged to describe the inner structure of the nucleus is called quantum

chromodynamics or QCD. It resembles QED in many ways but there are also some key differences. Both are examples of a quantum field theory, where the basic building blocks are quantized fields. In QED the basic matter field is the field of the electron, whereas in QCD the matter fields are called quarks. We can describe our everyday world quite accurately by including only two of them, the up quark and the down quark. In QED the interaction is mediated by photons and the corresponding particle in QCD is called the gluon, which was named after its ability to "glue" together several quarks. The quarks interact with each other by exchanging gluons in a manner somewhat analogous to electrons interacting with each other by exchanging photons. A key difference, however, is that gluons interact also with each other. This self-interaction has many consequences but the most dramatic one is that we have never directly observed individual quarks or gluons. The self-interaction of gluons binds themselves as well as the quarks into such tight packages that we believe they can never exist in isolation long enough to be observed. In contrast, the QED interactions become weaker at large distances and do not prevent the observation of isolated electrons or positrons.

The most familiar combinations of quarks are the proton and neutron, which receive their electric charge from two up quarks and one down quark for the proton, and one up quark and two down quarks for the neutron. In addition, the proton and neutron contain gluons that bind these quarks together as well as trace amounts of other particles which we will mention later. Collectively, all the particles made up of quarks and gluons are called hadrons and the term parton is used to refer to either a quark or a gluon inside a hadron.

When one tries to break hadrons apart by colliding them, lots of new particles are created but the quarks and gluons involved in the process are always organized into new hadrons before we can discern them individually. Luckily, it is possible to infer the properties of individual partons by observing the characteristics of such collisions as well as collisions of hadrons with electrons.

If we combine the ingredients of electrons, positrons, photons, up-quarks, down-quarks, and gluons, we are able to make remarkably accurate experimental predictions. The quest for deeper understanding of the building blocks of the universe, however, was far from over once these particles were discovered. When we dig deeper, there is a dizzying array of variation besides these basic building blocks. The electron has two heavier cousins called muon and tau. Like the electron, each has one unit of negative charge but their masses

are roughly 200 and 3500 times larger, respectively. All of us are constantly bombarded by a stream of muons that are produced when cosmic rays collide with air molecules in the upper atmosphere. However, they interact with us weakly enough that it takes sensitive equipment to detect them. Taus live for such a short time that we can only see them indirectly. After a tau is produced at a high energy collision, either through cosmic rays or in a particle accelerator, it decays to other particles in a way that enables us to identify the mother particle.

The decays of muons and taus involve the so-called weak force. Its perceived weakness comes from the fact that the force mediators have large masses, as far as fundamental particles are concerned. These force mediators are called weak bosons and they are analogous to photons in QED. The difference comes from the fact that photons are massless particles and can travel infinite distances, whereas the range of the weak bosons is inversely proportional to their large masses. Because they can only create a force between particles in close proximity, their influence is quite limited. However, they play a key role in radioactive decay and the fusion processes that give power to the Sun.

Electron, muon, and tau are collectively called charged leptons and each is accompanied by a neutral lepton called a neutrino. Neutrinos are the lightest particles with a mass[1] that we know of. Because they lack electric charge, they only interact through the weak force and gravity. At the particle level, gravity is even feebler than the weak force and therefore neutrinos pass effortlessly through thousands of lightyears of solid matter [37]. Trillions of neutrinos are streaming through us every second since they are copiously produced in nuclear reactions in the Sun.

In addition to the additional leptons, particle physicists have discovered four additional quarks named strange, charm, bottom, and top. The order of magnitude of their masses ranges from 10 % of the proton mass for the strange quark to 170 times the proton mass for the top. This can be compared with the masses of the up and down quarks, which are a fraction of a percent of the proton mass. We know that even inside ordinary protons and neutrons, strange, charm, bottom, and top quarks are created and destroyed in a constant dance of virtual particles. If we examine a proton with a fast enough probe, we can see traces of them as well as all other particles that exist. Furthermore, the heavier quarks create a whole zoo of additional hadrons which live long enough to be detected but are too

[1]Technically speaking, we only know that at least two of the three neutrinos have a mass.

unstable to act as building blocks for matter as we see it around us.

Let us review the particles that have been experimentally detected up to date. There are the six leptons: electron, muon, and tau together with their corresponding neutrinos. The number of quarks is also six: down, up, strange, charm, bottom, and top. Each one of the matter particles has a corresponding antiparticle, equal in every other way except having an opposite charge. Unless otherwise specified, from now on when we talk of particles such as electrons or quarks, we implicitly refer also to their antiparticles. There are also the three forces with their force carriers: electromagnetism carried by photons and described by QED, the strong force carried by gluons and described by QCD, and the weak force carried by weak bosons and described by another quantum field theory. The key difference between quarks and leptons is that quarks feel the electromagnetic, weak, and strong force, whereas leptons only feel the electromagnetic and weak force.

Quarks, leptons, and the force carriers have been combined into an elegant structure called the Standard Model (SM) of particle physics. It does not include gravity but since gravitational effects are unimportant at the energies of current particle accelerators, SM has been phenomenally successful in predicting the results of particle physics measurements for the last four decades. For more details about the history of SM and its predictive power, see Refs. [20, 60]. However, SM relies on a key ingredient that has not yet been observed. This is called the Higgs boson and it explains why quarks and charged leptons have a mass. It is possible that there could be another mechanism in place that explains these masses but postulating the Higgs boson is arguably the simplest solution. Because the Higgs boson is the last missing piece of SM, searching for it has been a key goal of the particle physics community for decades.

Despite the success of SM, great effort has been spent to explore the possibility of physics beyond SM. Besides the exclusion of gravity, there are several other theoretical reasons to suspect that SM does not tell the whole story of fundamental physics. From the experimental perspective, cosmological observations seem to suggest the existence of additional particles—although we do not yet have any direct evidence of them. We shall not concern ourselves with the multitude of possible ways to extend SM. However, it is important to understand how such theoretical efforts can be judged experimentally in order to see the full importance of the work described here.

In the early days of particle physics, several new particles—such as the muon—were

discovered by observing tracks in a cloud chamber. When a charged particle enters a cloud chamber, it produces ions from the supersaturated vapor inside by dislodging some of the electrons of the vapor molecules. The ionized molecules create a visible track of bubbles that shows the path of the charged particle. As years of intense research have passed, it is becoming increasingly unlikely that experimentalists could discover a new particle by observing its track or other direct evidence. Instead, various indirect methods have been developed to infer the existence of new particles based on measurements of other particles involved in a particle collision.

Most theories of physics beyond SM are tested by searching for particles that are heavier than anything we have observed up to this point. This leads to two challenges. First, producing these hypothetical heavy particles requires concentrating enormous amounts of energy into a small volume in order to create the conditions for the materialization of the new particles. The standard approach to doing this in a controlled manner is to build large particle accelerators that take lighter particles such as protons or electrons and give them enough energy that they travel close to the speed of light. When such particles are collided, they may produce new, heavier particles. The limiting factor is cost: accelerating particles to high energy requires large assemblies of expensive components. Currently, the most powerful accelerator in existence is the Large Hadron Collider (LHC) located at CERN, on the border of Switzerland and France. The main component of LHC is a 17-mile circular underground tunnel where protons are currently accelerated to an energy of 4 TeV, about four thousand times their rest mass. The experimentalists plan to increase this energy at least to 7 TeV, granting an unprecedented access to the world of subatomic particles.

There is another challenge that comes from the large mass of the proposed new particles: they disintegrate instantaneously after being produced. Their mass contains enough energy to turn the particle into many lighter particles and nature is always looking for ways to distribute large concentrations of energy into several smaller packets. In the same way as with the tau leptons, we seek to collect evidence for the existence of particles beyond SM by looking for patterns in the lighter particles that would be produced by the decay of a new heavy particle. The easiest way to infer the existence of a heavy particle would be if it decayed directly to an electron and antielectron (positron) or a muon and antimuon. Such pairs of high energy leptons are relatively straightforward to distinguish from all the particles flying around after a collision. The combined energy of the leptons pair would give

information about the mass of the new particle and detecting a large number of pairs could determine the mass accurately.

However, many models of new physics contain particles that do not decay directly to a pair of leptons. Oftentimes they produce a longer decay chain that may also involve quarks and gluons. Such models can be tested with less data than those where the new particles do not feel the strong interactions of QCD. This is because the LHC collides protons—which are essentially collections of quarks and gluons—and these partons turn most easily into other particles that have QCD interactions. Hence, any such particles could be observed sooner than others that only interact with ordinary matter through the weak or electromagnetic force.

There is a price to be paid, though. At the fundamental level, all of nature's interactions proceed in two directions; if a particle can easily be produced from quarks and gluons, it is also likely to decay into them. This is a challenge because it is much more difficult to make accurate measurements of quarks and gluons than of electrons and muons.

Ultimately, we want to take advantage of all the different ways to discover new particles. This is usually done by performing different analyses that focus on various ways for the particles to decay. In the end, theses analyses are combined in order to maximize the likelihood of discovery. In this work, we shall focus on collisions involving energetic quarks or gluons.

1.2 Defining and Measuring Jets

Although individual quarks and gluons have never been observed, they can leave visible signatures in the pattern of outgoing particles. This collection of outgoing particles is called the final state of the collision. If a particle collision produces an energetic quark or gluon, the QCD interactions will turn it into many more quarks and gluons which subsequently combine into hadrons. Most of the energy is carried by those hadrons that are approximately collinear with the original parton. Thus, an energetic parton produces what is called a hadronic jet: a collinear collection of hadrons resembling a jet of water spraying out of a garden hose.

Jets feature in many final states of interest at the LHC. They form a background for many new physics processes and also provide probes for QCD interactions at several different

scales. In this section, we shall explore different ways to define and measure the properties of jets.

To understand jets, it is helpful to briefly review the main components of a general purpose particle detector such as the CMS and ATLAS detectors at CERN. The innermost component is the tracker, which records the path of charged particles. Because the whole detector is permeated by a magnetic field, the charged particles follow curved trajectories. Measuring the curvature of the trajectories allows the determination of the charge and momentum of the particles. After the tracker, there are the electromagnetic and hadronic calorimeters that measure the energy of the particles. Photons and electrically charged particles leave energy in the electromagnetic calorimeter. The hadronic calorimeter measures mainly the energy of hadrons since most other particles have either been stopped in the electromagnetic calorimeter or do not interact with the detecter enough to be observed. Muons, however, are heavy enough to escape the electromagnetic calorimeter. Since the muon does not have strong interactions, it also goes through the hadronic calorimeter mostly unscathed. To take advantage of these special properties of the muon, there are a collection of muon chambers placed as the outermost layer of the detector. Since all other charged particles are mostly stopped by the calorimeters, the muon chambers give a very clean way to detect muons.

We are mainly interested in the tracker and the hadronic calorimeter since they help us observe the energy and momentum of particles inside hadronic jets. The curved path of the particles recorded by the tracker is shown in red in Fig. 1-1(a). The green and blue bars show how much energy is deposited in the calorimeters. This event display is from a collision in the CMS detector [31]. Another CMS event [32] with multiple jets is shown in Fig. 1-1(b) with the beam direction perpendicular to the image plane. The green tracks from the tracker coincide with the large energy deposits in the calorimeters and the shaded triangles represent jets.

Although these two figures makes it easy to visualize the detector, it is often more convenient to think of jets by cutting the cylindrical shape of the calorimeter open and spreading it as a flat surface. This produces the so-called (η, ϕ)-plane, where η is the pseudorapidity, which measures the angle with respect to the beam, and ϕ is the azimuthal angle. Pseudorapidity is related to the angle between the jet and the beam axis θ by the relation $\eta = -\ln[\tan(\theta/2)]$. Instead of using pseudorapidity η, the jet direction can also be

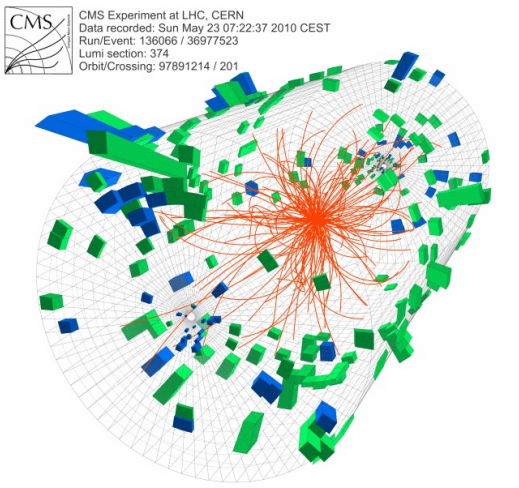

(a) The amount of energy deposited in different parts of the calorimeters is visualized with the height of the bar [31].

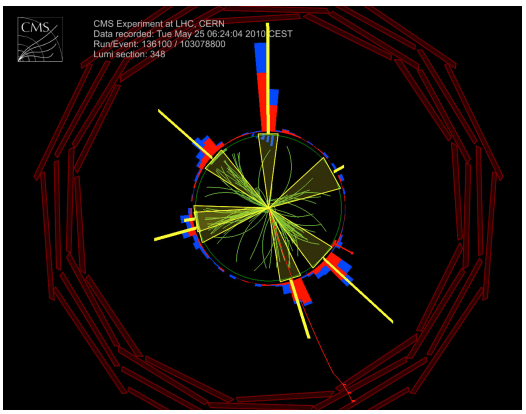

(b) The coincidence of the tracks and energy deposits is evident from a view along the beam pipe [32].

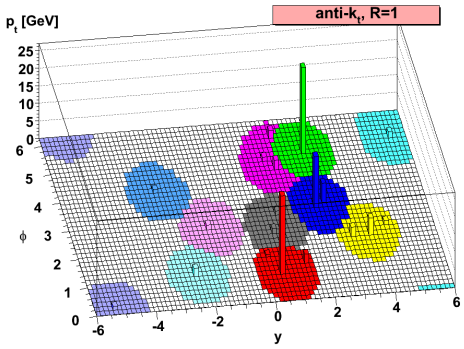

(c) The cylindrical shape of the calorimeter can be represented by a flat surface. [19].

Figure 1-1: Different representations help give a full picture of the characteristics of jets.

measured with rapidity y, which equals pseudorapidity for massless particles. In general, rapidity is given be $y = \frac{1}{2}\ln[(E + p_z)/(E - p_z)]$, where E is the energy of the particle and p_z is the component of the momentum along the beam direction, which is taken to be the z-axis. Fig. 1-1(c) shows simulated particles in (y, ϕ)-plane ordered into jets, which are represented by different colors [19]. Here the vertical axis is slightly different and shows the transverse momentum instead of the energy in a given cell. Using (y, ϕ) or (η, ϕ)-plane is convenient since the soft particles in the event are distributed approximately uniformly in these coordinates.

The last figure also illustrates a specific jet definition called the anti-k_t jet algorithm. Since a hadronic collision produces copious amounts of soft (low-energy) particles in all directions, the boundaries between different jets are not uniquely defined. In order to talk about jets, one must specify a jet algorithm that takes the output of a detector or a theoretical calculation and organizes them into jets.

A simple way to define jets would be to choose a set of jet directions and to fix a jet angle. A jet would then be defined to consist of all those particles whose direction is within the jet angle from the jet direction. The jet directions can be set to start from some initial seed values and they are varied to find directions that coincide with the direction of the total momentum of all the particles inside the jet. However, such a simple algorithm is not what is called infra-red and collinear-safe. This means that an additional emission of a low-energy (infra-red) or collinear particle can significantly change the final configuration of jets. This is highly undesirable since there is no theoretical way to predict the exact pattern of infra-red or collinear particles. Furthermore, intuitively it is clear that adding one low-energy particle to the final state should not make much of a difference to the jet pattern and neither should the splitting of an energetic particle into two energetic particles continuing into the same direction.

The first demonstrably infra-red and collinear-safe jet algorithm was the Sterman-Weinberg (SW) algorithm [52]. The SW algorithm defines a dijet event as one where all but a fraction β of the total energy is contained within a pair of oppositely directed cones of half-angle δ. The definition can also be extended for more jets if one specifies a way to determine the direction of the different jet axes. The SW algorithm is an example of a class called cone algorithms, which are named based on their shape. Even though the SW algorithm has been studied extensively due to its early introduction and simple definition, many of the current experimental studies use instead the Seedless Infrared Safe Cone (SISCone) algorithm [49]. In addition to being infrared safe, SIScone algorithm gives jets that are not sensitive to the initial seeds chosen in the jet search procedure.

Another class of jet algorithms are the recombination algorithms, which use a procedure to combine particles together one by one until in the end there remains a collection of jets and some particles which are left outside of the jets. Commonly used recombination algorithms include the k_t, Cambridge-Aachen, and the anti-k_t algorithm. Both cone and recombination algorithms have different strengths and weaknesses, depending on how one

wants to analyze jets. However, as we will explain in the next subsection, both classes present some challenges for performing precise theoretical calculations.

From theoretical point of view, there is a different and very convenient way to define jets in a dijet event. We can define hemisphere jets, where the phase space of the final state is divided into two hemispheres and all the particles in a given hemisphere form a jet. Initially, this might seem drastically different from cone or recombination algorithms. However, we are often interested in narrow jets, i.e. jets where the invariant mass of all the particles inside the jet is small. In this limit, the differences between different jet definitions become small, and calculations can be simplified by choosing the simplest possible jet definition as a reasonable starting point. However, the hemisphere jet algorithm can only be applied to dijet events.

In order to put different jet algorithms into use, we turn our attention to jet cross sections. A cross section for a given process measures the likelihood of that process taking place. In analogy with classical mechanics, we can represent the likelihood of a reaction by the size of the colliding objects. The larger the objects, the more likely they are to interact. This analogy gives the concept of quantum mechanical cross section both its name and units, which are length-squared.

A jet cross section quantifies the likelihood of a given jet process taking place. We can fix a number of jets, say N, and calculate the probability of producing at least N jets in a given collision. This is called an inclusive cross section. Alternatively, we may require that an event has exactly N jets as defined by a chosen jet algorithm. Calculating such a probability will give an exclusive cross section.

The measurement of exclusive jet cross sections, where one identifies a certain number of signal jets but vetoes additional jets, is an important aspect of Higgs and new-physics searches at the LHC and Tevatron. In such searches, the experimentalists often analyze the data separated into bins of different numbers of jets. This is done because the relative contributions of various signal and background channels often vary with the number of hard jets in the event. Hence, it is important to optimize the analyses for each jet bin. An important example is the Higgs search at the Tevatron and LHC [1, 21, 48], where they analyze the data separately for $H + 0$ jets, $H + 1$ jet, and $H + 2$ or more jets. The gluon fusion channel dominates the zero jet bin whereas the vector boson fusion channel contributes strongly to the two jet bin.

Reliable theoretical calculations of exclusive jet cross sections are essential to take full advantage of experimental data. The complication compared to the calculation of an inclusive N-jet cross section, where one sums over any additional jets, comes from the fact that the veto on additional jets imposes a restriction on the energetic initial- and final-state radiation off the primary hard partons, as well as on the overall soft radiation in the event. This restriction on additional emissions leads to the appearance of large Sudakov double logarithms in the perturbation theory. For example, if one uses a cut on the perpendicular momentum $p_T^{\rm cut}$ to implement the jet veto in an event with center-of-mass energy Q, the perturbative series will contain terms proportional to $\ln^2(p_T^{\rm cut}/Q)$. This is a well-known phenomenon and is due to an incomplete cancellation of infrared contributions between virtual corrections and restricted real radiation. For this reason, the calculation of exclusive jet cross sections is traditionally carried out with parton-shower Monte Carlo programs, where the parton shower allows one to resum the most singular leading double logarithms. In order to go beyond such leading logarithmic resummation, alternative tools must be used. We shall present one powerful approach in the next section.

1.3 Soft-Collinear Effective Theory

In many processes, the large Sudakov double logarithms produce a sizeable effect and it is important to resum them beyond leading logarithmic order. An analytic approach to calculate exclusive jet cross sections is possible using factorization and the methods of soft-collinear effective theory (SCET) [4, 6, 11, 12]. SCET provides powerful tools to study processes with a specific number of hard jets. It allows one to factorize the N-jet cross section into individually calculable pieces and resum the large logarithmic contributions to obtain a convergent perturbative series. The advantage of this approach is that the resummation can be carried out to much higher orders than is possible with parton showers. In addition, it is much easier than in a parton-shower program to include higher-order virtual corrections, and to correctly reproduce the inclusive cross section in the limit when the jet-veto cut is eliminated.

Schematically, the cross section for $pp \to N$ jets (plus some nonhadronic final state

which we suppress for now) can be factorized as [5, 7, 54]

$$\sigma_N = H_N \times \Big[B_a B_b \prod_{i=1}^{N} J_i \Big] \otimes S_N \,, \tag{1.1}$$

where $\times$ stands for normal multiplication whereas $\otimes$ represents a convolution. Later in this section, we will give concrete examples that illustrate what variables the different factors depend on. This formula directly applies to observables that implement a veto on additional jets which restricts the phase space to the exclusive N-jet region (assuming that Glauber effects cancel as they do in Drell-Yan [24]). The hard function H_N encodes hard virtual corrections to the underlying partonic $2 \to N$ process, the beam functions $B_{a,b}$ contain the parton distributions and perturbative collinear initial-state radiation from the colliding hard partons, and the jet functions J_i describe energetic collinear final-state radiation from the primary N hard partons produced in the collision. The soft function S_N describes the soft radiation in the event that couples to the in- and outgoing hard partons. Since the collinear and soft radiation are not separately observable, the soft function is convolved with the beam and jet functions. The veto on additional jets restricts the collinear initial-state radiation, the final-state radiation, and the soft radiation, which means the precise definition of the required beam, jet, and soft functions depends on the veto variable. The schematic representation in Eq. (1.1) can also be applied to e^+e^- collisions if we remove the beam functions.

In order to set the context of the work presented in this thesis, we will give here some examples of different factorization theorems. A simple application of Eq. (1.1) is the process of e^+e^- into dijets. In this case we have the factorization theorem [33, 42]

$$\frac{1}{\sigma_0} \frac{\mathrm{d}\sigma}{\mathrm{d}m_a^2 \, \mathrm{d}m_b^2} = H_{e^+e^-}^{2j}(Q,\mu) \int_{-\infty}^{\infty} \mathrm{d}k^+ \mathrm{d}k^- \, J_n(m_a^2 - Qk^+, \mu) J_{\bar{n}}(m_b^2 - Qk^-, \mu) S_{\mathrm{hemi}}(k^+, k^-, \mu) \,, \tag{1.2}$$

where σ_0 is the corresponding Born-level cross section, $m_{a,b}$ are the masses of the jets, Q^2 is the invariant mass squared of the e^+e^--system, vectors $n, \bar{n}$ label the jet directions, μ is the factorization scale, and S_{hemi} is the hemisphere soft function which encodes the soft radiation from two back-to-back hemisphere jets. We can heuristically think of $J_i(m^2, \mu)$ as describing the probability of producing enough collinear radiation to contribute m to the

mass of a jet. Similarly, $S_{\rm hemi}(k^+, k^-, \mu)$ corresponds to the probability of radiating enough soft particles to contribute $\sqrt{Qk^+}$, $\sqrt{Qk^-}$ to the masses of the two jets.

Another equally simple example is the inclusive Drell-Yan cross section [18, 24, 25]

$$\frac{1}{\sigma_0}\frac{\mathrm{d}\sigma}{\mathrm{d}Q^2\mathrm{d}Y} = \sum_{i,j}\int\frac{\mathrm{d}\xi_a}{\xi_a}\frac{\mathrm{d}\xi_b}{\xi_b}\frac{1}{Q^2}H_{ij}^{\rm incl}\Big(\xi_a,\xi_b,Y,Q^2,\mu\Big)\,f_i(\xi_a,\mu)\,f_j(\xi_b,\mu)\,, \tag{1.3}$$

where now Q^2 gives the invariant mass squared of the final-state lepton pair and Y is their rapidity. The sum is performed over partons $i,j = \{g,u,\bar{u},d,\ldots\}$, and $f_i(\xi_a)$ is the parton distribution function (PDF), which gives the probability of finding parton i inside the proton with momentum fraction ξ_a along the proton direction. Since we only measure Q^2 and Y, and stay away from the threshold limit, the hard function $H^{\rm incl}$ contains an inclusive sum over all soft radiation as well as the collinear radiation from the incoming protons. Only when additional measurements are made do we need to specify separate beam and soft scales. The introduction of these scales produces large logarithms that need to be summed.

In order to study the case of an exclusive 0-jet cross section, we must add beam functions. A beam function describes the probability of radiating collinear particles into a beam jet that is produced by an incoming hadron. A beam jet resembles a central jet but it lies along a beam direction. We can write the beam function in a factorized form

$$B_i(t,x,\mu) = \sum_j\int_x^1\frac{\mathrm{d}\xi}{\xi}\,\mathcal{I}_{ij}\Big(t,\frac{x}{\xi},\mu\Big)f_j(\xi,\mu), \tag{1.4}$$

where we sum over partons $j = \{g,u,\bar{u},d,\ldots\}$, t is the virtuality of the parton participating in the hard collision, x is its momentum fraction, $\mathcal{I}_{ij}$ are Wilson coefficients that can be calculated in perturbation theory, and f_j is the standard PDF as before. At tree level, $\mathcal{I}_{ij}^{\rm tree}(t,x/\xi,\mu) = \delta_{ij}\,\delta(t)\,\delta(1-x/\xi)$ and we see that the tree level beam function reduces to the PDF

$$B_i^{\rm tree}(t,x,\mu) = \delta(t)\,f_i(x,\mu)\,. \tag{1.5}$$

Inclusive beam functions can be employed by using a simple event-shape variable called beam thrust τ_B [54] to veto central jets. Beam thrust is the analogue of thrust for beam jets. If we consider the limit of small jet masses in the $e^+e^- \to$ jets process, then thrust is the sum of the squared masses of the jets scaled by the invariant mass squared of the process. Same applies for beam thrust, except that we consider a hadronic collision with

two beam jets and no central jets. Then we can write the following expression for beam thrust

$$\tau_B \approx \frac{m_a^2 + m_b^2}{Q^2} + \mathcal{O}\Big(\frac{m_a^2}{Q^2}, \frac{m_b^2}{Q^2}\Big)\,, \tag{1.6}$$

where Q^2 is the invariant mass squared of the final state particles.

The 0-jet cross section defined using beam thrust has been studied for Drell-Yan production in Ref. [57] and for Higgs production in Ref. [17]. The factorization theorem for the cross section of Higgs production with a jet veto is for example relevant for the $H \to WW^*$ search channel, where a jet veto is needed to remove the large $t\bar{t} \to WWb\bar{b}$ background. The use of an event shape for the jet veto makes a resummation of large logarithms to next-to-next-to-leading logarithmic (NNLL) order possible.

The factorization theorem for the cross section of Drell-Yan production with no jets can be written as

$$\begin{aligned}\frac{1}{\sigma_0}\frac{\mathrm{d}\sigma}{\mathrm{d}Q^2\mathrm{d}Y\,\mathrm{d}B_a^+\,\mathrm{d}B_b^+} &= \sum_{ij}\frac{1}{Q^2}H_{ij}(Q^2,\mu)\int \mathrm{d}k_a^+\,\mathrm{d}k_b^+ \\ &\quad\times B_i(2E_a(B_a^+ - k_a^+), x_a, \mu)B_j(2E_b(B_b^+ - k_b^+, x_b, \mu)S_{\mathrm{ihemi}}(k_a^+, k_b^+, \mu),\end{aligned} \tag{1.7}$$

where B_a^+, B_b^+ can be related to the masses of the beam jets and $E_{a,b}$ are the energies of the beams. The structure of Eq. (1.7) is very similar to Eq. (1.2). The different hard interaction is encoded in the hard function and the difference between incoming beam jets and outgoing final state jets is accounted for by replacing the jet functions with the beam functions.

The generalization of beam thrust to processes with N jets is N-jettiness, $\mathcal{T}_N$, introduced in Ref. [55]. It is designed such that in the limit $\mathcal{T}_N \to 0$ the final state consists of N narrow central jets plus two narrow beam jets along the beam axis (for hadron collisions). N-jettiness is defined as

$$\mathcal{T}_N = \sum_k \min_i \Big\{\frac{2q_i \cdot p_k}{Q_i}\Big\} \equiv \sum_i \mathcal{T}_N^i\,, \tag{1.8}$$

where k runs over all the hadrons in the final state, i runs over a, b for the two beams and $1, \ldots, N$ for the final-state jets, p_k is the momentum of the k^{th} particle, the q_i are massless reference momenta for the jets and beams, and the Q_i are normalization factors which we discuss in more detail in Chap. 3.

The minimization in Eq. (1.8) chooses the value of i that gives the smallest value for

$q_i \cdot p_k$. In other words, it assigns each particle to the jet or the beam that it is closest to. If an event has $N+2$ pencil-like central and beam jets, then none of the particles will contribute to the sum because its distance from the jet it belongs to is zero. Particles that are collinear to one of the jet directions will have small distance to that direction and make a small contribution. Because each term in the sum is proportional to the momentum of the particle, soft particles will give a small contribution no matter which direction they are in. Hence, demanding that $\mathcal{T}_N$ takes a small value restricts the final state particles to be either soft or collinear to one of the central or beam jet directions.

The contribution from each jet or beam sector is denoted by $\mathcal{T}_N^i$, and as will be shown in Chap. 4, it is closely connected to the mass of the jet or the beam. For e^+e^- collisions, the terms for the beams are absent and we continue to let N refer to the number of jets. The complexity of the calculation for the e^+e^- $(N+2)$-jettiness is equivalent to N-jettiness for pp collisions. We will discuss N-jettiness in more detail in Chap. 3 and present a factorization theorem that extends Eq. (1.7) to the case of N jets in Chap. 4.

Factorization for N-jettiness can be contrasted with factorization for more common jet algorithms. We illustrate the effect of jet algorithms with the process e^+e^- into three jets as derived in Refs. [29, 30]

$$\begin{aligned}\frac{\mathrm{d}\sigma}{\mathrm{d}m_1\,\mathrm{d}E_{1,2,3}\,\mathrm{d}^2\vec{n}_{1,2,3}} &= \frac{\mathrm{d}\sigma^{(0)}}{\mathrm{d}E_{1,2,3}\,\mathrm{d}^2\vec{n}_{1,2,3}} H^{3j}_{e^+e^-}(n_{1,2,3}; E_{1,2,3}) \int \mathrm{d}m_1^J \mathrm{d}m_1^S \delta(m_1 - m_1^J - m_1^S) \\ &\quad \times \int \frac{\mathrm{d}n_1\cdot k_1}{2\pi} \int \frac{\mathrm{d}n_2\cdot k_2}{2\pi} \int \frac{\mathrm{d}n_3\cdot k_3}{2\pi} \int \frac{\mathrm{d}^4 r}{(2\pi)^4} \\ &\quad \times J_{n_1,2E_1}(m_1^J, n_1\cdot k_1) J_{n_2,2E_2}(n_2\cdot k_2) J_{n_3,2E_3}(n_3\cdot k_3) S_{\mathrm{alg}}(m_1^S, r)\,,\end{aligned} \tag{1.9}$$

where one of the jets has mass m_1 and two of the jets are only constrained by the parameters of the jet algorithm. The energies and directions of the three jets are denoted by E_i and $\vec{n}_i$, respectively.

When the cross section for jets defined by a traditional jet algorithm is factorized, the perturbative corrections are complicated by: the presence of non-global logarithms [2, 3, 26, 28], the potential for soft radiation to be strongly influenced by the number of energetic partons in the jets, and by cuts on soft radiation that introduce additional soft scales that must be handled within factorization [29, 30]. Depending on the kinematics of the event, these effects can contribute additional corrections to Eq. (1.9). Jet functions for

jet algorithms in $e^+e^- \to$ jets have been calculated at next-to-leading order (NLO) in Refs. [30, 39]. The second of these is the basis of Chap. 2 of this thesis. In Ref. [30] the soft function for $e^+e^- \to$ jets was calculated at NLO, where a cut on the total energy outside the jets was used as the jet veto. Using N-jettiness avoids these issues that complicate the structure of perturbation theory.

For an N-jettiness cross section calculation using Eq. (1.1), the last needed ingredient for an evaluation of generic processes at NNLL is the one-loop N-jettiness soft function, S_N, the computation of which is detailed in Chap. 4. The hard function in Eq. (1.1) can be obtained from the corresponding QCD fixed-order calculation, many of which are now known to NLO. The beam and jet functions are again the inclusive beam and jet functions (which are known to one [17, 35, 45, 57] and two loops [13, 14], respectively). This is the case since N-jettiness does not restrict the collinear radiation inside a jet. Furthermore, since N-jettiness itself covers all of phase space, no additional restriction on the radiation outside of jets or beams is needed.

1.4 Outline

In Chap. 2 we focus on the the calculation of the quark jet function with a realistic jet algorithm. We start by treating the case of a general jet algorithm. Next, we review the SW jet algorithm and give the result for the corresponding jet function. We plot the renormalized SW quark jet function as well as the hemisphere quark jet function to illustrate the difference between the two cases.

We describe N-jettiness in more detail in Chap. 3 and address the broader question of soft radiation in hadron colliders in Chap. 4. In Sec. 4.1, results are given for the fully differential $\mathcal{T}_N^i$ factorization theorem, and for renormalization group consistency equations for the N-jettiness soft function. Sec. 4.2 contains details of the NLO calculation of S_N, including developing a simple method that uses a set of overlapping hemispheres to extract UV divergences and the corresponding induced logarithmic terms. The remaining $\mathcal{O}(\alpha_s)$ terms are then given by finite integrals that do not involve the UV regulator, and we will refer to these as the non-hemisphere contributions. This hemisphere decomposition is not specific to the N-jettiness observable, and we show how it can be applied in general. For the N-jettiness soft function we reduce the non-hemisphere contributions to well-behaved

one-dimensional numerical integrals (some details are relegated to appendices).

In Chap. 5 we combine our calculation of the 1-jet soft function with the hard, beam, and jet functions to study the phenomenology of jet mass distributions. We focus on normalized cross sections, which removes most of the dependence on the hard function. The case of Higgs production with one exclusive jet will be used as the main example. We find that the position of the peak in the jet mass spectrum agrees with the recent results from the ATLAS collaboration.

Chapter 2

Realistic Dijets at Lepton Colliders

Because there is no unique way to determine which particles should be combined into a jet, both experimental and theoretical work on jets must start with a choice of a jet definition. In the framework of SCET, the choice of jet algorithm affects both the jet and the soft function, as well as the beam functions if the beam jets are defined with a jet algorithm. Much of the SCET work has considered hemisphere jets since they provide an easy starting point. In this chapter, we derive a formalism to calculate the quark jet function defined with a realistic jet algorithm to $\mathcal{O}(\alpha_s)$ and to leading order in power counting. We focus on the quark jet function since in the process $e+e-$ into dijets, the leading order contribution consists of quark jets. By realistic algorithm we mean one that would be considered useful by an experimentalist.

Our results apply for any jet algorithm that can be formulated in terms of theta functions depending on the momenta of the final state particles and that can be regularized using dimensional regularization. As an example, we look at the SW algorithm, which has been considered using SCET in Refs. [8, 10, 22, 59]. We calculate the full quark jet function J_i, including the finite part, as a function of the invariant mass of the jet. The work in this chapter was first presented in Ref. [39].

2.1 Quark Jet Function with a Generic Algorithm

Our goal is to derive a formalism to accommodate any jet algorithm that can be expressed in terms of phase space cuts. In this section, we outline the derivation for an expression for the jet function in the presence of a jet algorithm. Although our calculation for the jet function

applies for any number of jets, we will present it in the context of dijets. Even when there are more In this case, there are only two collinear directions, and it is convenient to define some notation specifically for this chapter. We denote the direction of the quark jet axis by a unit vector $\vec{n}$ and choose a coordinate system such that $\vec{n} = (0, 0, 1)$. It is convenient to work in the light cone coordinates with basis vectors $n^\mu = (1, \vec{n})$ and $\bar{n}^\mu = (1, -\vec{n})$ satisfying $n^2 = \bar{n}^2 = 0,\ n \cdot \bar{n} = 2$. Because our jets are back-to-back, the vector $\bar{n}$ both completes the set of basis vectors and labels the antiquark jet direction. We denote the quark and antiquark jet functions by $J_n(s)$ and $J_{\bar{n}}(s)$, respectively. The power expansion is performed in terms of a parameter λ, which characterizes the ratio of the transverse and the collinear momentum in a jet.

In our chosen coordinate system, any momentum can be decomposed as

$$p^\mu = n{\cdot}p\,\frac{\bar{n}^\mu}{2} + \bar{n}{\cdot}p\,\frac{n^\mu}{2} + p_\perp^\mu \equiv (n{\cdot}p,\, \bar{n}{\cdot}p,\, p_\perp) \equiv \left(p^+,\, p^-,\, p_\perp\right). \tag{2.1}$$

The momentum of a collinear parton i in n-direction scales as $p_i \sim Q(\lambda^2, 1, \lambda)$ so we can write $p_i^0, p_i^3 = \frac{1}{2}p_i^- + \mathcal{O}(\lambda)$. The invariant mass-squared is given by Q^2 and the total jet momentum is $p_n + r_n = (Q, r_n^+, 0)$, where p_n is the large label momentum and r_n is the smaller residual momentum. Thus, the invariant mass of the jet is given by $s \equiv (p_n + r_n)^2 = Qr_n^+ \sim Q^2\lambda^2$. Because of the specific observable we consider, namely the jet invariant mass, we are free to use the coordinate system specified above, which removes all dependence on the total transverse momentum $p_n^\perp$. For a general observable, we would also need to include $p_n^\perp$. To define a jet algorithm, we also need to consider the momenta of the final state partons. At $\mathcal{O}(\alpha_s)$, momentum conservation and the on-shell condition for the final state partons make it possible to write all the momenta in the problem in terms of the jet momentum components $p_n^- = Q$ and r_n^+ together with the gluon four-momentum p_g.

The jet function can be written in terms of the gauge invariant quark jet field $\chi_n = W_n^\dagger \xi_n$, and it is also convenient to use $\chi_{n,\omega} = \delta(\omega - \bar{n}\cdot\mathcal{P})(W_n^\dagger\xi_n)$, where $\bar{n}\cdot\mathcal{P}$ gives the large label momentum of the combination $W_n^\dagger\xi_n$. The collinear Wilson line is defined as

$$W_n(x) = \sum_{\text{perms}} \exp\left[-\frac{g}{\bar{n}{\cdot}\mathcal{P}}\bar{n}{\cdot}A_n(x) \right], \tag{2.2}$$

where A_n is the collinear gluon field and the sum is taken over the permutations of the

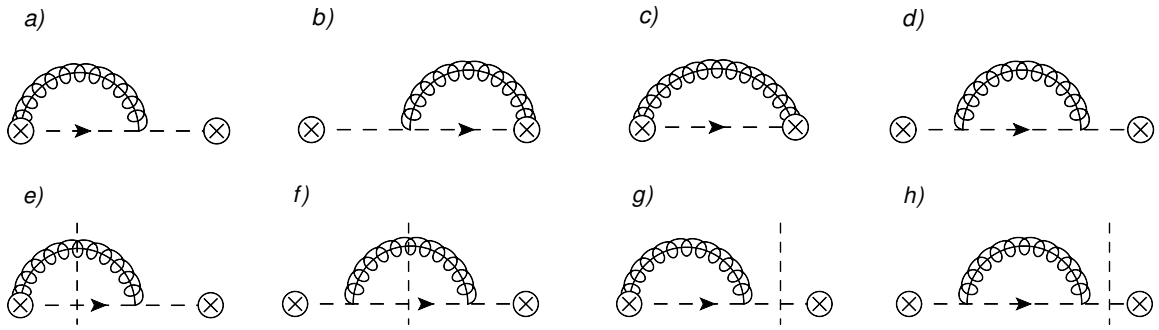

Figure 2-1: The Wilson line diagrams (a) and (b) give identical contributions. Diagram (c) vanishes in Feynman gauge. Diagram (d) gives the wavefunction renormalization contribution. Diagrams (e) and (f) show the real cuts and diagrams (g) and (h) show the virtual cuts. The mirror image of (h) gives the other virtual cut of (d).

locations that the gluons attach to.

We will use the term inclusive jet function to refer to the case where no jet algorithm is applied and denote it by $J_n^{(\mathrm{inc})}$. It is discussed in Ref. [9, 14] and we define it as

$$\begin{aligned} J_n^{(\mathrm{inc})}(s,\mu) &= \frac{-1}{8\pi N_c Q}\,\mathrm{Disc}\int \mathrm{d}^d x\, e^{ir_n\cdot x}\,\mathrm{tr}\langle 0|\mathrm{T}\{\overline{\chi}_{n,Q}(0)\frac{\bar{n}\!\!\!/}{2}\chi_n(x)\}|0\rangle \\ &= \frac{1}{8\pi N_c Q}\sum_{X_n}\int \mathrm{d}^d x\, e^{ir_n\cdot x}\,\mathrm{tr}\langle 0|\frac{\bar{n}\!\!\!/}{2}\chi_n(x)|X_n\rangle\langle X_n|\overline{\chi}_{n,Q}(0)|0\rangle, \end{aligned} \tag{2.3}$$

where N_c is the number of colors, Disc denotes the discontinuity in the imaginary part, $d = 4-2\epsilon$, the trace is over color and spin, and T stands for time ordering. Because of charge conjugation symmetry, the antiquark jet function $J_{\bar{n}}(s)$ does not have to be considered separately. We write J_n as a sum over final states in order to implement a jet algorithm. The final states are restricted according to a constraint function $F(a_i)$, which defines an algorithm in terms of parameters a_i and depends on the momenta of the particles in $|X_n\rangle$. Thus, $F(a_i)$ is also a function of the operators $\hat{p}_j$ which have the final state momenta p_j as eigenvalues. In this section, we will work with a generic $F(a_i,\hat{p}_j)$ and in Sec. 2.2 we will give a concrete example when we specialize to the SW algorithm. Inserting the constraint function gives the algorithm-dependent jet function

$$J_n^F(s,\mu) = \frac{1}{8\pi N_c Q}\sum_{X_n}\int \mathrm{d}^d x\, e^{ir_n\cdot x}\,\mathrm{tr}\langle 0|\frac{\bar{n}\!\!\!/}{2}\chi_n(x)F(a_i,\hat{p}_j)|X_n\rangle\langle X_n|\overline{\chi}_{n,Q}(0)|0\rangle. \tag{2.4}$$

Eq. (2.4) is valid at any order in α_s, but the functional form of $F(a_i,\hat{p}_j)$ changes from order

to order. Following the discussion of Hornig et al. on angularity jet functions in Ref. [38], we implement the needed phase space restrictions on the final states by introducing an F-discontinuity, where the standard Cutkosky cutting rules are modified by inserting a factor of $F(a_i, \hat{p}_j)$ into the cut propagators. The diagrams that contribute to J_n^F at one loop are shown in Fig. 2-1 (a) - (d). We note that diagram (c) vanishes in Feynman gauge. At this order, we can cut through the loop or a single quark propagator, which we call "real" and "virtual" cuts, respectively. Diagrams (e) and (f) give the real cuts and (g) and (h) show the virtual cuts. The virtual cuts are independent of the algorithm and are contained in a proper interpretation of the inclusive jet function. Hence, the algorithm-dependent contribution is given by taking the real cuts and inserting $F(a_i, \hat{p}_j)$ to the cut propagators. In order to use the known results from the literature more conveniently, we add and subtract the inclusive jet function on the second line.

$$\begin{aligned} J_n^F(s) &= \frac{-1}{8\pi N_c Q}\mathrm{Disc}_F \int \mathrm{d}^d x\, e^{ir_n\cdot x}\, \mathrm{tr}\langle 0|\mathrm{T}\{\overline{\chi}_{n,Q}(0)\bar{\not{n}}\chi_n(x)\}|0\rangle \\ &= J_n^{(\mathrm{inc})}(s) + \frac{-1}{8\pi N_c Q}\mathrm{Disc}\int \mathrm{d}^d x\, e^{ir_n\cdot x}\, \mathrm{tr}\langle 0|\mathrm{T}\{\overline{\chi}_{n,Q}(0)\,(F(a_i,\hat{p}_j)-1)\,\bar{\not{n}}\chi_n(x)\}|0\rangle \\ &\equiv J_n^{(\mathrm{inc})}(s) + \Delta J_n^F, \end{aligned} \tag{2.5}$$

where we have introduced notation ΔJ_n^F for the algorithm dependent contribution. Note that setting $F = 1$ in Eq. (2.5) leads to $\Delta J_n^F = 0$ leaving only the inclusive contribution, as expected. To find an expression for ΔJ_n^F, we use the modified cutting rules to add a factor of $F(a_i, \hat{p}_j)$ and to replace the gluon and quark propagators in the loop by delta functions $\delta\left(p_g^- p_g^+ + \left(p_g^\perp\right)^2\right)$ and $\delta\left(p_q^- p_q^+ + \left(p_q^\perp\right)^2\right)$. Using the momentum conservation relation $p_q + p_g = (Q, r^+, 0)$ and the above delta functions, the phase space integrals over the gluon momentum components p_g^+ and $p_g^\perp$ can be performed to give the relations

$$p_g^+ = -\frac{\left(p_g^\perp\right)^2}{p_g^-}, \qquad \left(p_g^\perp\right)^2 = -\frac{p_g^-(Q-p_g^-)s}{Q^2}. \tag{2.6}$$

These relations must be used when writing the constraint function. Finally, the calculations can be simplified by a change of variables $y \equiv p_g^-/Q$.

In a factorization theorem the contribution of soft quarks and gluons is encoded in the soft function. In order to avoid double-counting when the loop momentum of a collinear field in the jet function becomes soft, a zero-bin subtraction must be performed [44]. This means

that we remove from the jet function the contribution of those phase space configurations that include a soft final state particle. The naive collinear result without the subtraction is obtained by summing over the contributions from the real cut Feynman diagrams in Fig. 2-1, diagrams (e) and (f), (and counting diagram (e) twice to account for its mirror image). This gives

$$\Delta\tilde{J}_n^F(s) = \frac{\alpha_s C_F}{4\pi} A(\epsilon) \frac{1}{\mu^2} \left(\frac{\mu^2}{s}\right)^{1+\epsilon} \int_0^1 \mathrm{d}y \; \frac{1}{y^\epsilon} (1-y)^{-\epsilon} \left(\frac{4(1-y)}{y} + y(d-2)\right) (F(a_i, y) - 1), \tag{2.7}$$

where Eq. (2.6) has been used to write F as a function of y and the algorithm parameters a_i, the tilde denotes that the zero-bin subtraction has not been performed, and $A(\epsilon) = 1 - \frac{\pi^2\epsilon^2}{12} + \mathcal{O}(\epsilon^3)$. For the SW algorithm, we will see that after the zero-bin has been subtracted, ΔJ_n is finite as $\epsilon \to 0$ so we will eventually take $A(\epsilon) = 1$. There is a zero-bin contribution both for the gluon and the quark becoming soft but only the former contributes at leading order in power counting. Furthermore, as the soft gluon wavefunction renormalization vanishes in Feynman gauge, we only need to consider a zero-bin for the gluon in Fig. 2-1 (e). To obtain the zero-bin result, we assign scaling $p_g \sim Q\lambda^2$ [44] to all components of the gluon momentum. The effect of the zero-bin scaling to algorithm constraints is discussed in detail in App. A. The end result is that instead of Eq. (2.6), the replacement rules for the zero-bin piece are

$$p_g^+ = \frac{s}{Q}, \qquad \left(p_g^\perp\right)^2 = -p_g^- p_g^+ = -\frac{p_g^- s}{Q}, \qquad p_q^- = Q, \qquad p_q^+ = 0, \qquad p_q^\perp = 0. \tag{2.8}$$

Using these relations, the zero-bin contribution to ΔJ_n^F is

$$\Delta J_{n0}^F(s) = \frac{\alpha_s C_F}{4\pi} A(\epsilon) \frac{1}{\mu^2} \left(\frac{\mu^2}{s}\right)^{1+\epsilon} \int_0^\infty \mathrm{d}y \; \frac{4}{y^{1+\epsilon}} (F_0(a_i, y) - 1), \tag{2.9}$$

where $F_0(a_i, y)$ denotes that the constraints are written using Eq. (2.8). For a sufficiently inclusive jet algorithm such as the hemisphere algorithm, the zero-bin contribution remains a scaleless integral that vanishes in dimensional regularization. However, a more restrictive algorithm can introduce a scale that gives a nontrivial zero-bin subtraction and we will see that this is what happens for the SW case.

2.2 Sterman-Weinberg Algorithm

As explained in Chap. 1, the SW algorithm defines a dijet event in terms of the cone half-angle δ and energy fraction of the soft radiation β. We will keep only the leading order in $\delta \sim \beta \sim \lambda$, including both power and logarithmic dependence. As will be seen later, to leading order in β the final result for the jet function is independent of β, even if we pick $\delta \sim \lambda,\ \beta \sim \lambda^2$. It would seem logical to also consider $\delta \sim \lambda^2,\ \beta \sim \lambda$ but as has been pointed out in Ref. [53], one should require $\sin(\delta) > \beta/(1-\beta)$ in order to preserve the back-to-back orientation of the two jets. To lowest order in the parameters, this corresponds to $\delta > \beta$. Finally, one could consider $\delta, \beta \sim \lambda^2$ but then it would be more natural to define a new expansion parameter $\lambda' \equiv \lambda^2$ and set $\delta, \beta \sim \lambda'$. Thus, the natural possibilities to consider are $\delta \sim \beta \sim \lambda$ or $\delta \sim \lambda,\ \beta \sim \lambda^2$ and our results for the jet function are valid for both cases. For the sake of definiteness, we will take $\delta \sim \beta \sim \lambda$ with the understanding that $\sin(\delta) > \beta/(1-\beta)$.

When we apply the SW algorithm to the jet function, the question at one loop is whether the n-collinear quark and gluon create one or two jets. If both partons lie within δ from the jet axis or if one of the partons has energy $E_i < \beta\, Q$, only a single jet is produced. As stated before, a soft quark would contribute only at higher order in the power counting so we have two regions of phase space to consider: a "cone" region where both particles lie inside the cone and an "outside-cone" region where the gluon is not inside the cone and has energy $E_g < \beta\, Q$. We take the jet axis to lie along the $\vec{n}$-direction and then the cone region corresponds to the momenta of both partons lying within δ of $\vec{n}$.

The invariant mass s of the jet is related to how far apart the final state particles are spread. At one loop and using the on-shell condition for massless partons, we find that $s = p_g^- p_q^- \sin^2(\phi/2) \approx p_g^- p_q^- (\phi/2)^2$ where ϕ is the angle between the quark and the gluon. If no jet algorithm is applied, in the center-of-mass frame momentum conservation implies $s \leq (Q/2)^2$. In the SW algorithm with the gluon inside the cone, the maximum value is reached when $p_g^- = p_q^- = Q/2$ and $\phi = 2\delta$, which gives $s \leq (Q\delta/2)^2$. This constraint is satisfied by the naive contribution to the jet function which only has support for $s \leq (Q\delta/2)^2$. However, the standard approach to the gluon zero-bin subtraction is to utilize the result obtained in the zero-bin limit everywhere, and hence there is no upper limit on p_g^- or on s. It may be possible to use the freedom in defining a zero-bin subtraction

scheme to define a non-minimal subtraction where one would obtain a jet function which is nonzero only for $s \leq (Q\delta/2)^2$. We leave this question to future work. When the gluon is outside the cone, the maximum is reached when $y = 2\beta$ and $\phi = \pi$, which gives $s \leq 2\beta\, Q^2$. However, because of the power counting $s \sim Q\lambda^2$, this condition is always satisfied to leading order.

The constraints for the SW algorithm are illustrated in Fig. 2-2 in terms of the variables p_g^- and $p_g^\perp$. Fig. 2-2 (a) describes the phase space for the naive collinear contribution. If there were no jet algorithm, $p_g^\perp$ would be integrated all the way to infinity in the full range $0 \leq p_g^- \leq Q$. For the SW algorithm, the region defined by $p_g^- \leq 2\beta\, Q$ and $2|p_g^\perp|/p_g^- \geq \delta$ corresponds to a gluon being emitted outside the cone, and the triangular region at the bottom of the figure gives the cone contribution. The corresponding constraint function $F_{\rm SW}$ is given by

$$\begin{aligned} F_{\rm SW} &= \theta\left(\tan\delta - \frac{|p_g^\perp|}{|p_g^3|}\right)\theta\left(\tan\delta - \frac{|p_q^\perp|}{|p_q^3|}\right) + \theta\left(\frac{|p_g^\perp|}{|p_g^3|} - \tan\delta\right)\theta\left(\beta Q - p_g^0\right) \\ &= \theta\left(y - \frac{4s}{4s+Q^2\delta^2}\right)\theta\left(\frac{Q^2\delta^2}{4s+Q^2\delta^2} - y\right) + \theta\left(\frac{4s}{4s+Q^2\delta^2} - y\right)\theta\left(2\beta - y\right) + \mathcal{O}(\lambda,\delta,\beta) \\ &= \theta\left(y - \frac{4s}{4s+Q^2\delta^2}\right)\theta\left(\frac{Q^2\delta^2}{4s+Q^2\delta^2} - y\right) + \theta\left(2\beta - y\right) + \mathcal{O}(\lambda,\delta,\beta), \end{aligned} \tag{2.10}$$

where Eq. (2.6) was used in getting to the second line, and the first theta function in the second term is always satisfied at leading order in the power counting. This is because $4s/(4s+Q^2\delta^2) \sim \lambda^0$ but $y \sim \lambda$ in the second term due to $\beta \sim \lambda$. We note that the two theta functions in the first term imply $\theta(Q^2\delta^2/4 - s)$ and thus limit the maximum allowed jet mass.

The zero-bin phase space is shown in Fig. 2-2 (b). Without the algorithm, the integration region would extend to infinity for both p_g^- and $p_g^\perp$. As explained in App. A, the zero-bin scaling only affects the jet algorithm through the conditions in Eq. (2.8). This results in a zero-bin constraint function

$$\begin{aligned} F_{0,\rm SW} &= \theta\left(\tan\delta - \frac{|p_g^\perp|}{|p_g^3|}\right) + \theta\left(\frac{|p_g^\perp|}{|p_g^3|} - \tan\delta\right)\theta\left(\beta Q - p_g^0\right) \\ &= \theta\left(y - \frac{4s}{Q^2\delta^2}\right) + \theta\left(2\beta - y\right) + \mathcal{O}(\lambda,\delta,\beta), \end{aligned} \tag{2.11}$$

where we again used the fact that $4s/(Q^2\delta^2) \sim \lambda^0$ to eliminate the first theta function in

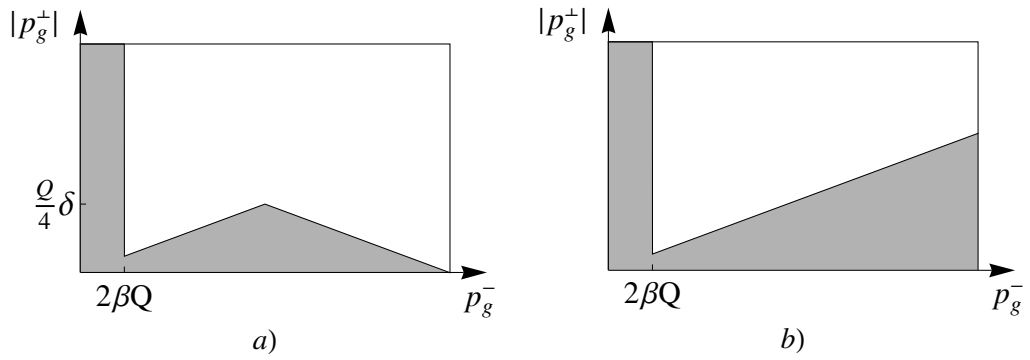

Figure 2-2: Phase space regions for the SW algorithm. Naive collinear (a) and zero-bin (b). The region at the left-hand side of the figures corresponds to a gluon outside the cone with energy $E_g \leq \beta Q$. The region at the bottom of the figures describes the region where both partons are inside the cone. For the zero-bin contribution, p_g^- is integrated all the way to infinity.

the second term. (This result for the constraint function in the zero-bin region agrees with Ref. [30].) We note that the conditions from Eq. (2.8) eliminate the second theta function in the first term. This theta function constrained the quark to be inside the cone. Its absence can be understood physically by remembering that in the gluon zero-bin, the quark carries all of the label momentum and is automatically inside the cone. In this case, there is no upper limit on the jet mass s.

2.3 Results

We are now ready to apply our general result for the case of the SW algorithm. For both y and s/μ^2, we have used the following distribution identity

$$\frac{\theta(y)}{y^{1+\epsilon}} = -\frac{\delta(y)}{\epsilon} + \left[\frac{\theta(y)}{y}\right]_+ - \epsilon\left[\frac{\theta(y)\ln(y)}{y}\right]_+ + \mathcal{O}(\epsilon^2), \tag{2.12}$$

where $[\theta(y)\ln^n(y)/y]_+$ denote plus functions, which we define such that they give zero when integrated from 0 to 1. The different possible definitions and their relationship with one another are discussed for example in Appendix B of Ref. [43].

Combining Eqs. (2.7) and (2.10) we find for the naive collinear contribution

$$
\begin{aligned}
&\Delta\tilde{J}_n^{\mathrm{SW}}(s)\\
&\quad=\frac{\alpha_s C_F}{4\pi}A(\epsilon)\theta\left(\delta^2-\frac{4s}{Q^2}\right)\left\{\delta(s)\left[\frac{2}{\epsilon^2}-\frac{4}{\epsilon}\left\{\ln 2\beta+\frac{1}{2}\ln\left(\frac{Q^2\delta^2}{4\mu^2}\right)\right\}+2\ln^2 2\beta\right.\right.\\
&\qquad\left.-\ln^2\left(\frac{Q^2\delta^2}{4\mu^2}\right)\right]+\frac{4}{\mu^2}\left[\frac{\mu^2\theta(s)}{s}\right]_+\left\{\ln 2\beta+\ln\left(\frac{Q^2\delta^2}{4\mu^2}\right)+\frac{6s}{4s+Q^2\delta^2}\right\}\\
&\qquad\left.-\frac{4}{\mu^2}\left[\frac{\mu^2\theta(s)\ln\left(s/\mu^2\right)}{s}\right]_+\right\}+\frac{\alpha_s C_F}{4\pi}\theta\left(\frac{4s}{Q^2}-\delta^2\right)\frac{4}{\mu^2}\left[\frac{\mu^2\theta(s)}{s}\right]_+\left\{\frac{3}{4}+\ln 2\beta\right\}.
\end{aligned}
\tag{2.13}
$$

Eqs. (2.9) and (2.11) give the corresponding zero-bin contribution

$$
\begin{aligned}
&\Delta J_{n0}^{\mathrm{SW}}(s)\\
&\quad=\frac{\alpha_s C_F}{4\pi}A(\epsilon)\theta\left(\delta^2-\frac{4s}{Q^2}\right)\left\{\delta(s)\left[\frac{2}{\epsilon^2}-\frac{4}{\epsilon}\left\{\ln 2\beta+\frac{1}{2}\ln\left(\frac{Q^2\delta^2}{4\mu^2}\right)\right\}+2\ln^2 2\beta\right.\right.\\
&\qquad\left.-\ln^2\left(\frac{Q^2\delta^2}{4\mu^2}\right)\right]+\frac{4}{\mu^2}\left[\frac{\mu^2\theta(s)}{s}\right]_+\left\{\ln 2\beta+\ln\left(\frac{Q^2\delta^2}{4\mu^2}\right)\right\}-\frac{4}{\mu^2}\left[\frac{\mu^2\theta(s)\ln\left(s/\mu^2\right)}{s}\right]_+\Bigg\}\\
&\qquad+\frac{\alpha_s C_F}{4\pi}\theta\left(\frac{4s}{Q^2}-\delta^2\right)\left\{\frac{4}{\mu^2}\left[\frac{\mu^2\theta(s)}{s}\right]_+\left\{\ln 2\beta+\ln\left(\frac{Q^2\delta^2}{4\mu^2}\right)\right\}\right.\\
&\qquad\left.-\frac{4}{\mu^2}\left[\frac{\mu^2\theta(s)\ln\left(s/\mu^2\right)}{s}\right]_+\right\}.
\end{aligned}
\tag{2.14}
$$

The total algorithm-dependent part ΔJ_n is given by the difference of Eqs. (2.13) and (2.14) and reads

$$
\Delta J_n^{\mathrm{SW}}(s)=\frac{\alpha_s C_F}{4\pi}\theta\left(\delta^2-\frac{4s}{Q^2}\right)\frac{24}{4s+Q^2\delta^2}+\frac{\alpha_s C_F}{4\pi}\theta\left(\frac{4s}{Q^2}-\delta^2\right)\left\{\frac{3}{s}+\frac{4}{s}\ln\left(\frac{4s}{Q^2\delta^2}\right)\right\}.
\tag{2.15}
$$

Using the definition of the plus function [43], it can be seen that when $[\theta(y)\ln^n(y)/y]_+$ is integrated against a function $f(y)$ such that $f(0)=0$, we can ignore the plus function prescription because it only makes a difference at $y=0$. Hence, we do not need to use plus functions in Eq. (2.15). We note that the outside-cone region for the gluon cancels between the collinear and the zero-bin contributions and hence there is no β-dependence in the final result. This cancellation has been discussed in the literature [22] and has to take place since the purpose of the zero-bin subtraction is to remove any soft contribution from

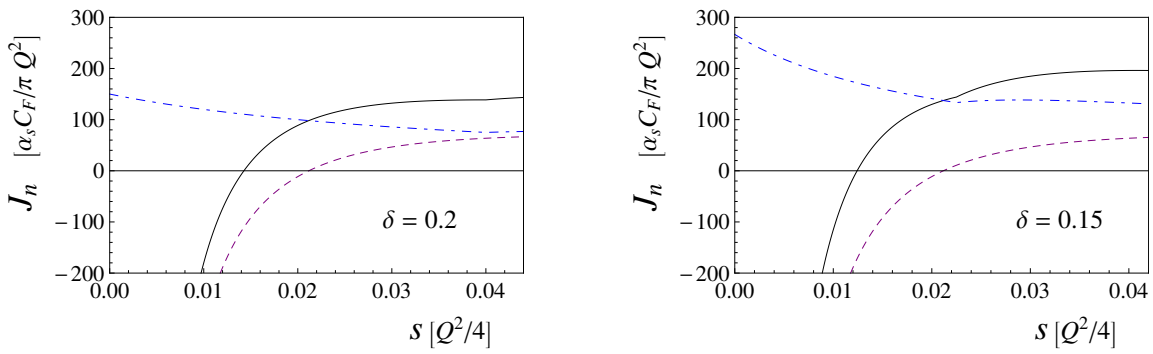

Figure 2-3: The renormalized jet function in units of $\alpha_s(\mu)C_F/\pi Q^2$, where we choose $\mu = 0.1 \times Q/2$. The SW (solid black line) and the inclusive (dashed purple line) jet functions are plotted as well as the difference of the two (dash-dotted blue line) for $\delta = 0.2$ (left) and $\delta = 0.15$ (right).

the collinear diagrams and the gluon must be soft to be outside the cone. We have also grouped the terms according to whether s is limited to be less or greater than $(Q\delta/2)^2$.

We will now give an explicit expression for the full SW jet function. To do so, we need the inclusive jet function $J_n^{(\mathrm{inc})}$, which can be found in the literature [9, 14]. Using the notation of Ref. [34], it can be written as

$$\begin{aligned} J_n^{(\mathrm{inc})}(s,\mu) =& \delta(s) + \frac{\alpha_s C_F}{4\pi}\Bigg\{\delta(s)\left(\frac{4}{\epsilon^2}+\frac{3}{\epsilon}+7-\pi^2\right) \\ & - \frac{4}{\mu^2}\left[\frac{\mu^2\theta(s)}{s}\right]_+\left(\frac{1}{\epsilon}+\frac{3}{4}\right) + \frac{4}{\mu^2}\left[\frac{\mu^2\theta(s)\ln\left(s/\mu^2\right)}{s}\right]_+\Bigg\}. \end{aligned} \tag{2.16}$$

The SW jet function is given by the sum of Eqs. (2.15) and (2.16). Since the jet algorithm does not modify the $1/\epsilon$-poles, the anomalous dimension is

$$\gamma_{J_n}^{\mathrm{SW}}(s,\mu) = -\frac{\alpha_s C_F}{4\pi}\left\{\frac{8}{\mu^2}\left[\frac{\mu^2\theta(s)}{s}\right]_+ - 6\,\delta(s)\right\}. \tag{2.17}$$

The renormalized SW jet function in $\overline{\mathrm{MS}}$-scheme is given by

$$\begin{aligned} J_{n,\mathrm{ren}}^{\mathrm{SW}}(s,\mu) = \delta(s) + \frac{\alpha_s C_F}{4\pi}\Bigg\{ & \delta(s)\left(7-\pi^2\right) - \frac{3}{\mu^2}\left[\frac{\mu^2\theta(s)}{s}\right]_+ + \frac{4}{\mu^2}\left[\frac{\mu^2\theta(s)\ln(s/\mu^2)}{s}\right]_+ \\ & + \theta\left(\delta^2-\frac{4s}{Q^2}\right)\frac{24}{4s+Q^2\delta^2} + \theta\left(\frac{4s}{Q^2}-\delta^2\right)\left[\frac{3}{s}+\frac{4}{s}\ln\left(\frac{4s}{Q^2\delta^2}\right)\right]\Bigg\} \end{aligned} \tag{2.18}$$

The most important result of this chapter is the renormalized SW jet function in Eq. (2.18).

It is plotted in Fig. 2-3 for $\delta = 0.2$ and $\delta = 0.15$ while keeping $s \neq 0$. We have chosen the jet scale to be $\mu = 0.1 \times (Q/2)$. The SW and the inclusive jet functions are denoted by the solid black line and the dashed purple line, respectively. The jet function is continuous, but the derivative of the algorithm dependent contribution given in Eq. (2.15) changes sign at $s = (Q\delta/2)^2$, where one theta function turns off and the other turns on. We note that the algorithm contribution denoted by the dash-dotted blue line is always positive.

Comparing the algorithm contributions in Fig. 2-3 for the two values of the cone angle, one can see a change in shape. For $\delta = 0.15$, small values of s — which correspond to narrow jets — contribute more than large values of s. For $\delta = 0.2$, the algorithm contribution is flatter, signifying a more equal contribution from jets of different size. This makes physical sense since a broader cone allows contributions from wider jets. Unlike the shape, the overall normalization of the algorithm contribution does not follow from physical intuition — we might have naively expected that increasing the cone angle would give a larger value for the magnitude of the jet function. However, care must be taken in assigning physical meaning to the normalization of a jet function computed in an unphysical subtraction scheme ($\overline{\text{MS}}$), which is also illustrated by the fact that the inclusive jet-function has a zero at finite s. Different renormalization schemes include different constant pieces in the jet function and make its magnitude scheme dependent. Additionally, it should be remembered that a jet algorithm also affects the soft function, which must be combined with jet functions to see the full δ dependence of the cross section.

It is also interesting to integrate Eq. (2.18) over s up to s_{max}. We call this the integrated jet function $\bar{J}^{\text{SW}(s_{\text{max}})}_{n,\text{ren}}(\mu)$ and it is given by

$$\begin{aligned}
\bar{J}^{\text{SW}(s_{\text{max}})}_{n,\text{ren}}(\mu) \equiv& \int_0^{s_{\text{max}}} \mathrm{d}s\, J^{\text{SW}}_{n,\text{ren}}(s,\mu) \\
=& 1 + \theta\left(\delta^2 - \frac{4s_{\text{max}}}{Q^2}\right)\frac{\alpha_s C_F}{4\pi}\left\{7 - \pi^2 - 3\ln\left(\frac{s_{\text{max}}}{\mu^2}\right) + 2\ln^2\left(\frac{s_{\text{max}}}{\mu^2}\right)\right. \\
&\left. + 6\ln\left(\frac{4s_{\text{max}} + Q^2\delta^2}{Q^2\delta^2}\right)\right\} + \theta\left(\frac{4s_{\text{max}}}{Q^2} - \delta^2\right)\frac{\alpha_s C_F}{4\pi}\left\{7 - \pi^2\right. \\
&\left. - 3\ln\left(\frac{Q^2\delta^2}{4\mu^2}\right) + 2\ln^2\left(\frac{Q^2\delta^2}{4\mu^2}\right) + 6\ln 2 + 4\ln\left(\frac{s_{\text{max}}}{\mu^2}\right)\ln\left(\frac{4s_{\text{max}}}{Q^2\delta^2}\right)\right\}. \qquad (2.19)
\end{aligned}$$

The renormalized NLO contribution to the integrated jet function is plotted in Fig. 2-4 as a function of s_{max} and we have again chosen the jet scale to be $\mu = 0.1 \times (Q/2)$. On the

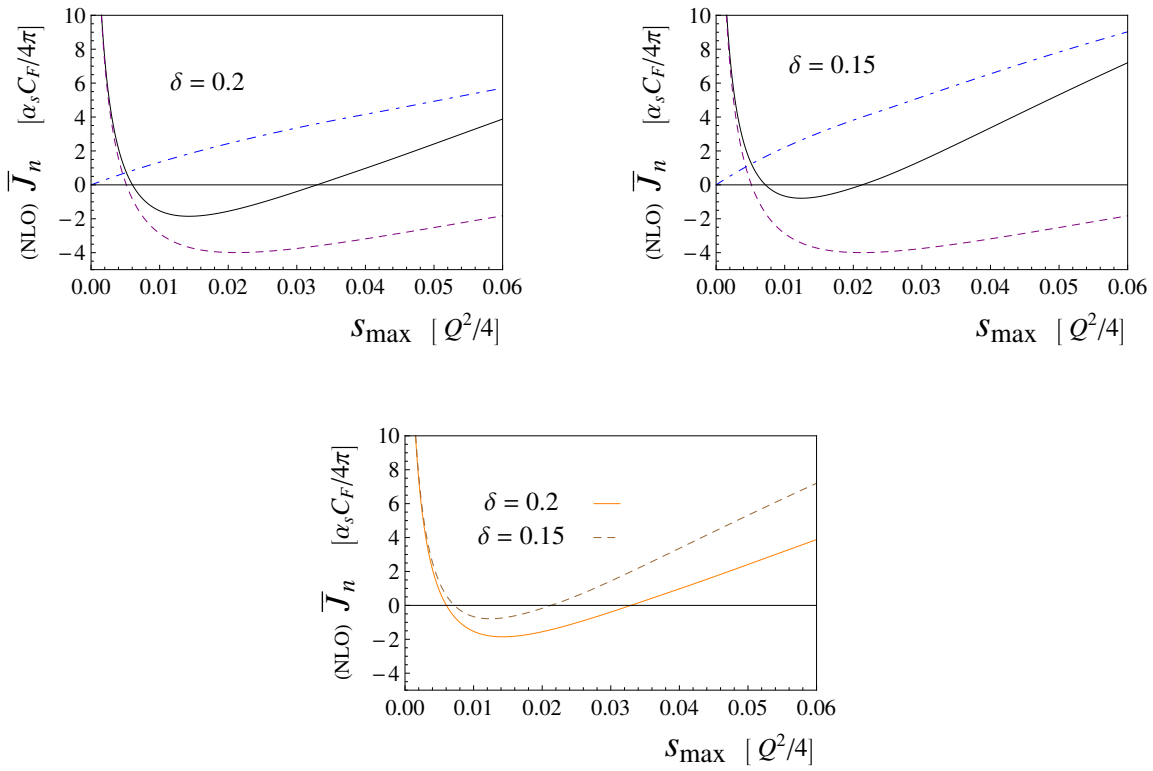

Figure 2-4: The renormalized NLO contribution to the integrated jet function is plotted in units of $\alpha_s(\mu)C_F/4\pi$, where we choose $\mu = 0.1 \times Q/2$. On the first row we plot the SW (solid black line) and the inclusive (dashed purple line) integrated jet functions as well as the difference of the two (dash-dotted blue line) for $\delta = 0.2$ (left) and $\delta = 0.15$ (right). On the second row we compare the integrated SW jet functions for the two values of δ.

first row of Fig. 2-4, we plot the jet function for the SW case and the inclusive case, as well as the difference of the two, for $\delta = 0.2$ and $\delta = 0.15$. Since the difference between the SW and the inclusive jet functions was always positive in Fig. 2-3, we can see that the difference between the integrated SW and inclusive jet functions in Fig. 2-4 increases monotonically as a function of $s_{\max}$. On the second row of Fig. 2-4, the integrated SW jet functions for the two different values of δ are compared. As with the differential jet function, the individual integrated jet function cannot be directly connected to any measured quantity. Only the total cross section, which combines the jet function with the hard, soft, and possibly beam functions, carries physical meaning.

The calculation of the quark jet function defined with a jet algorithm was completed independently by two separate groups. The other group reported their work in Refs. [29, 30], where they also calculated the necessary soft function and plotted the full differential cross section. To see the effect of the jet angle on the full cross section, we show a figure from their paper, which is obtained by plotting Eq. (1.9). They denote the jet angle by R, which corresponds to our δ, and their calculation is done as a function of angularity, denoted by τ_a. Different values of a correspond to different relative weights to particles in calculating τ_a depending on their distance from the jet axis: the larger the value of a, the more weight is given to the particles far away from the jet axis. The choice $a = 0$ corresponds to jet mass, $\tau_0 = s/Q^2$. In Fig. 2-5, we see the differential cross section as a function of τ_a for a quark jet with τ_0 corresponding to the central, blue line. The values corresponding to the different curves from top to bottom are $a = -\frac{1}{2}, -\frac{1}{4}, 0, \frac{1}{4}, \frac{1}{2}$. We can see that decreasing the jet angle moves the peak to the left, which makes intuitive sense as smaller jet angle restricts the jet mass to be smaller.

We shall return to the topic of differential jet cross sections in Chap. 5, where we investigate jets defined by 1-jettiness in the context of hadron colliders. Before doing so, we will investigate the properties of N-jettiness jets in more detail in the next chapter.

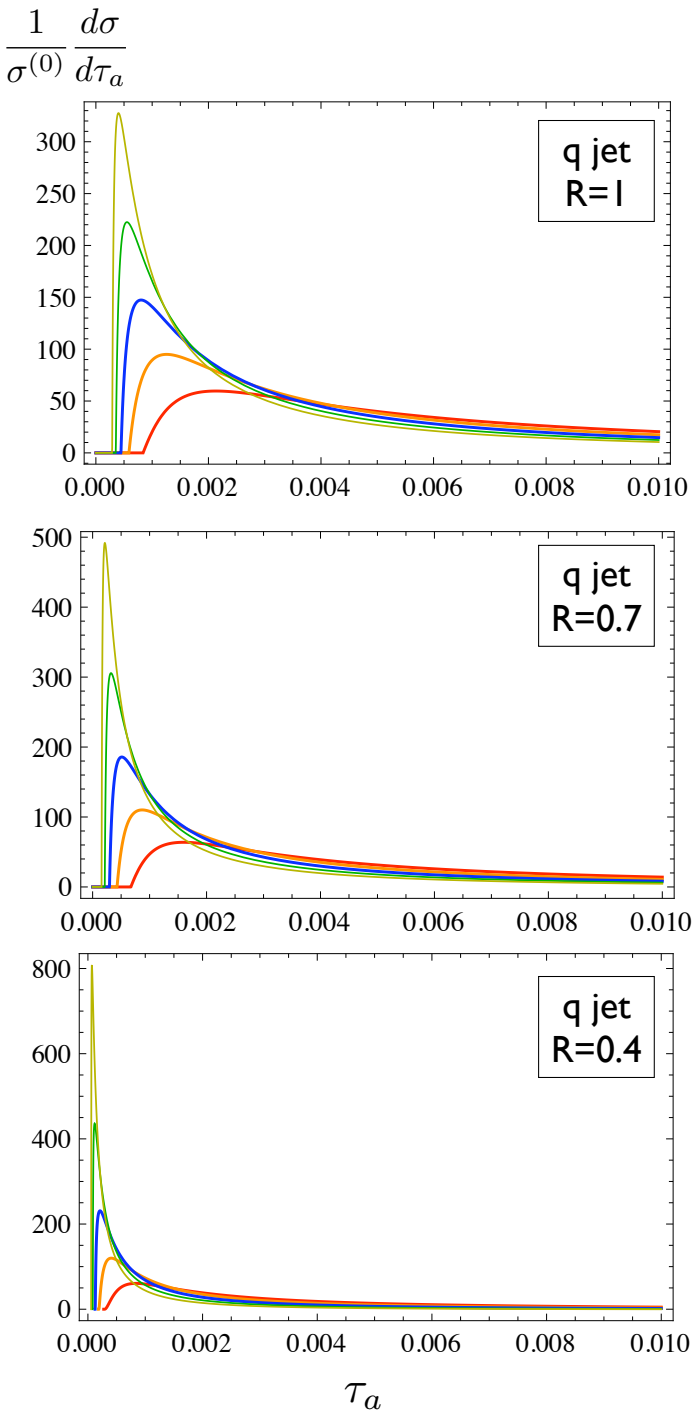

Figure 2-5: Decreasing the jet angle R moves the peak of the differential cross section to the left. The different curves correspond to different values of a. From top to bottom, the values are $a = -\frac{1}{2}, -\frac{1}{4}, 0, \frac{1}{4}, \frac{1}{2}$. Plotted here is a quark jet.

Chapter 3

N-jettiness

We introduced an event shape called N-jettiness in Chap. 1. In this chapter, we shall explore how N-jettiness divides the final state phase space into jet and beam regions and thus functions as a jet algorithm. The work in this chapter was first presented in Ref. [40].

For convenience, we will repeat the definition here:

$$\mathcal{T}_N = \sum_k \min_i \Big\{ \frac{2q_i \cdot p_k}{Q_i} \Big\} \equiv \sum_i \mathcal{T}_N^i \,. \tag{3.1}$$

As stated in Chap. 1, k runs over all the hadrons in the final state, i runs over a, b for the two beams and $1, \ldots, N$ for the final-state jets, p_k is the momentum of the k^{th} particle, the q_i are massless reference momenta for the jets and beams, and the Q_i are normalization factors. For each jet we can take

$$q_i^\mu = \omega_i \, (1, \vec{n}_i) \,, \tag{3.2}$$

where ω_i is the jet energy, and $\vec{n}_i$ is the jet direction. The ω_i and $\vec{n}_i$ can be predetermined with a suitable jet algorithm, and the choice of algorithm only gives power-suppressed effects, as explained in Ref [55]. Alternatively, using a minimization procedure to determine the $\vec{n}_i$ makes N-jettiness a true jet algorithm [58]. For the beams we have

$$q_a^\mu = \frac{1}{2} x_a \, E_{\text{cm}} (1, \hat{z}) \,, \qquad q_b^\mu = \frac{1}{2} x_b \, E_{\text{cm}} (1, -\hat{z}) \,, \tag{3.3}$$

where E_{cm} is the center-of-mass energy, $\hat{z}$ points along the beam axis, and $x_{a,b}$ are the

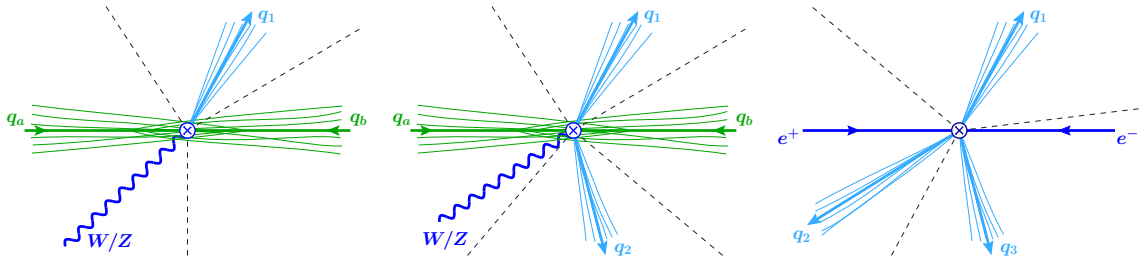

Figure 3-1: Jet and beam reference momenta for 1-jettiness (left), 2-jettiness (middle) and e^+e^- 3-jettiness (right). In the middle plot the jets and beams do not necessarily lie in a plane.

light-cone momentum fractions of the colliding hard partons. The latter are defined as

$$x_a E_{\rm cm} = Q\, e^{Y}\,, \qquad x_b E_{\rm cm} = Q\, e^{-Y}\,, \tag{3.4}$$

where Q^2 and Y are the total invariant mass-squared and rapidity of the hard interaction. They are determined from the observed final state by

$$\begin{aligned} Q^2 &= x_a x_b E_{\rm cm}^2 = (q_1 + \cdots + q_N + q)^2\,, \\ 2Y &= \ln\frac{x_a}{x_b} = \ln\frac{(1,-\hat{z})\cdot(q_1+\cdots+q_N+q)}{(1,\hat{z})\cdot(q_1+\cdots+q_N+q)}\,. \end{aligned} \tag{3.5}$$

Here q^μ denotes the total momentum of the non-hadronic final state if one is present.

The choice of the q_i^μ is illustrated in Fig. 3-1 for 1-jettiness (left panel), 2-jettiness (middle panel), and e^+e^- 3-jettiness (right panel). For the first two cases q^μ is given by the momentum of the W/Z. In SCET the q_i^μ's become the large label momenta on the collinear fields, which can be thought of as the momenta of the partons in the hard interaction. The minimum in Eq. (1.8) divides the total phase space into $N+2$ regions, one for each beam and jet, as indicated by the dashed lines in Fig. 3-1. This is how $\mathcal{T}_N$ acts as a jet algorithm, and we can consider distinct measurements on each of these jets. The simplest example is $\mathcal{T}_N^i$ which is essentially the same as measuring the invariant mass of the jet. This correspondence will be made precise in Chap. 4.

The Q_i in Eq. (1.8) are dimension-one variables that characterize the hardness of the jets. Different choices for the Q_i correspond to choosing different distance measures in the minimization in $\mathcal{T}_N$. For example, for fixed $Q_i = Q$, the distance measure is just the invariant mass, $2q_i\cdot p_k$. The resulting jet and beam regions in this case are illustrated for 2-

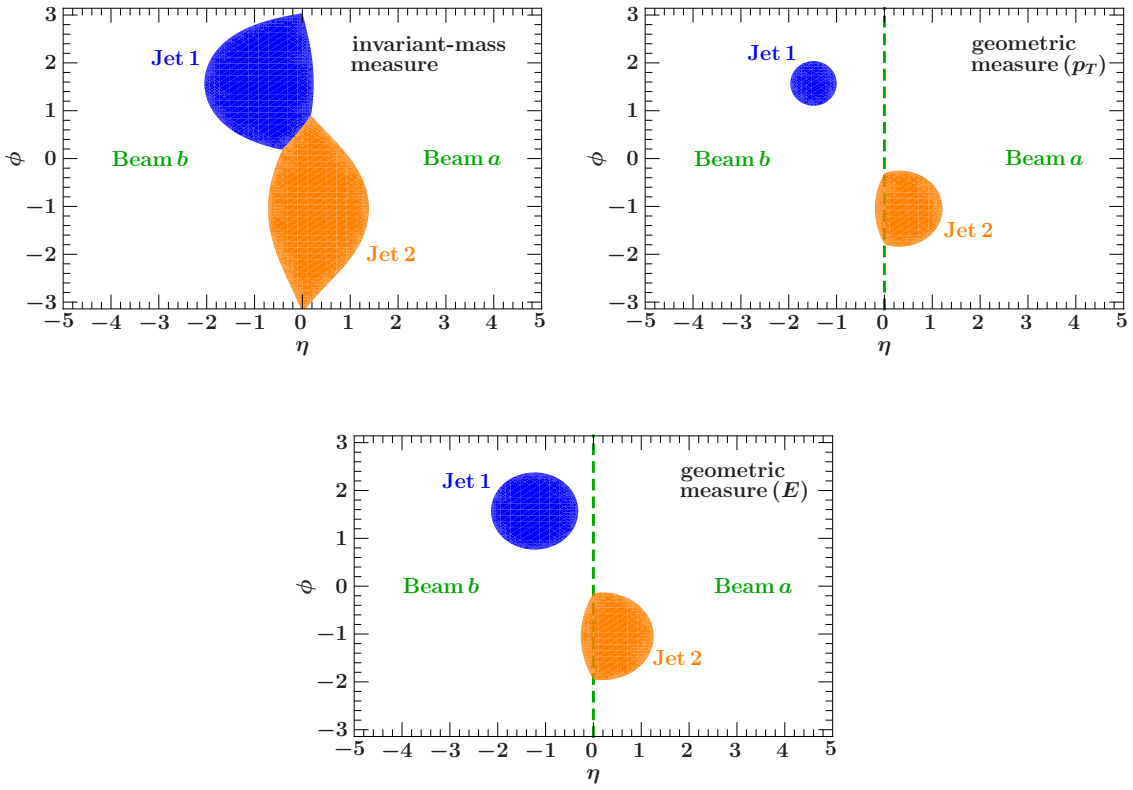

Figure 3-2: The jet and beam regions for two jets using 2-jettiness. On the top left we use the invariant-mass measure $Q_i = Q$. On the top right we use geometric measure (p_T) with $Q_i = |\vec{q}_{iT}|$ for the jets and $Q_{a,b} = x_{a,b}E_{\rm cm}$ for the beams. On the bottom we use geometric measure (E) with $Q_i = E_i$ for the jets and $Q_{a,b} = x_{a,b}E_{\rm cm}$ for the beams.

jettiness in the top left panel of Fig. 3-2. Choosing the jet transverse momentum $Q_i = |\vec{q}_{iT}|$ for the jets, gives the geometric measure (p_T), which is boost-invariant along the beam axis,

$$\begin{aligned}\frac{2q_i \cdot p_k}{|\vec{q}_{iT}|} &= |\vec{p}_{kT}|\,(2\cosh\Delta\eta_{ik} - 2\cos\Delta\phi_{ik}) \\ &\approx |\vec{p}_{kT}|\left[(\Delta\eta_{ik})^2 + (\Delta\phi_{ik})^2\right]. \end{aligned} \tag{3.6}$$

Here, $\Delta\eta_{ik} = \eta_i - \eta_k$, $\Delta\phi_{ik} = \phi_i - \phi_k$ are the differences in (pseudo)rapidity and azimuthal angle between the direction of jet i and particle k. The second line is valid in the limit of small $\Delta\eta$ and $\Delta\phi$. Equation (3.6) results in approximately circular boundaries for the jet regions, as illustrated in the top right panel of Fig. 3-2. In this case only the $\vec{n}_i$ part of q_i^μ enters. Another way to have circular boundaries is to employ geometric measure (E), which is similar to the (p_T) case except that we use $Q_i = E_i$ for the jets. This is demonstrated in the bottom panel of Fig. 3-2. Comparing to Fig. 1-1(c), we can see that the geometric

measure (E) resembles anti-k_t algorithm when the jet is somewhat removed from $\eta = 0$ since in those regions both have circular jets of constant size as a function of η.

For the beams we have

$$\frac{2q_a \cdot p_k}{Q_a} = \frac{Q}{Q_a} |\vec{p}_{kT}| \, e^{Y - \eta_k} \,, \tag{3.7}$$

with $Y - \eta_k \to -Y + \eta_k$ for $a \to b$. Here two potential choices for $Q_{a,b}$ are $Q_{a,b} = Q$, giving the invariant-mass distance measure, or $Q_{a,b} = Qe^{\pm Y} = x_{a,b} E_{\rm cm}$, which gives

$$\frac{2q_{a,b} \cdot p_k}{Q_{a,b}} = |\vec{p}_{kT}| e^{\mp \eta_k} \,. \tag{3.8}$$

We will carry out our analysis and one-loop calculations keeping Q_i arbitrary, enabling various choices to be explored using our results. From an experimental point of view certain choices will be more advantageous than others. For example, the second choice above for $Q_{a,b}$ is useful if the total rapidity cannot be measured because there are missing-energy particles in the final state.

For convenience we define the dimensionless reference momenta and their invariant products

$$\hat{q}_i^\mu = \frac{q_i^\mu}{Q_i} \,, \qquad \hat{s}_{ij} = 2\hat{q}_i \cdot \hat{q}_j \,. \tag{3.9}$$

We can then rewrite Eq. (1.8) as follows,

$$\begin{aligned} \mathcal{T}_N &= \sum_i \mathcal{T}_N^i \equiv \sum_i 2\hat{q}_i \cdot P_i \\ P_i^\mu &= \sum_k p_k^\mu \prod_{j \neq i} \theta\big(\hat{q}_j \cdot p_k - \hat{q}_i \cdot p_k\big) \,, \end{aligned} \tag{3.10}$$

where P_i^μ is the total four-momentum in region i. The $\mathcal{T}_N^i$ are thus given by the small light-cone component of the P_i measured along their respective collinear directions $\hat{q}_i$. In Chap. 4 we will explore the factorization theorem that is fully differential in the $\mathcal{T}_N^i$.

Chapter 4

Soft Radiation at Hadron Colliders

Chap. 2 focused on the production of jets in $e+e-$ collisions, but the expression derived for the jet function can also be used with hadron colliders, provided that we define the jets in the same way. However, the most complicated part of calculating the cross section for a multi-jet process is deriving an expression for the soft function.

The soft function ties together the beams and the jets in the event through the radiation of soft gluons. As reviewed in Chap. 1, there are several complications associated with factorization for traditional jet algorithms and these are mainly connected with the calculation of the soft function. Using N-jettiness to determine the jet boundaries and to define an exclusive jet cross section gives us better control over the factorization and the resummation of large logarithms. In this chapter, we shall describe the calculation of the N-jettiness soft function which allows us to perform NNLL-resummation for exclusive N-jet production. The work in this chapter was first presented in Ref. [40].

4.1 Setup of the Calculation

We shall begin this section by giving the factorization theorem for the individual N-jettiness contributions. This will be followed by an analysis of the renormalization group running and the one-loop renormalization of the soft function.

4.1.1 N-Jettiness Differential in Jet Regions

The factorization theorem for $\mathrm{d}\sigma/\mathrm{d}\mathcal{T}_N$ was given in Ref. [55], and is derived in a straightforward manner from SCET, see Refs. [5, 7, 54] (with an assumption so far implicit in all

N-jet factorization formulae about the cancellation of Glauber gluons). Instead of measuring $\mathcal{T}_N$, the manipulations leading to the factorization theorem are no more difficult when we consider the fully differential cross section, where we measure each individual $\mathcal{T}_N^i$. The value of $\mathcal{T}_N^i$ determines the transverse mass of region i relative to the direction $\vec{n}_i$ since

$$\begin{aligned} M_{iT}^2 &= P_i^2 + \vec{P}_{i\perp}^2 = (\bar{n}_i \cdot P_i)(n_i \cdot P_i) \\ &= 2q_i \cdot P_i \left[1 + \mathcal{O}(\lambda^2)\right] \\ &= Q_i \mathcal{T}_N^i \left[1 + \mathcal{O}(\lambda^2)\right], \end{aligned} \tag{4.1}$$

where $n_i^\mu = (1, \vec{n}_i)$, $\bar{n}_i^\mu = (1, -\vec{n}_i)$. In the last line we used $\bar{n}_i \cdot q_i = \bar{n}_i \cdot P_i + \mathcal{O}(\lambda^2)$, where $\lambda^2 \sim \mathcal{T}_N^i/Q$ and the power corrections depend on how the magnitude of q_i is fixed.

If the label vector $\vec{n}_i$ is chosen to be aligned with the direction of the jet three-momentum $\vec{P}_i$ such that $\vec{n}_i \cdot \vec{P}_i/|\vec{P}_i| \sim 1 + \mathcal{O}(\lambda^4)$ then $\vec{P}_{i\perp}^2 = 0 + \mathcal{O}(\lambda^4)$ and the transverse mass is the same as the invariant mass.

$$M_i^2 = P_i^2 = Q_i \mathcal{T}_N^i \left[1 + \mathcal{O}(\lambda^2)\right]. \tag{4.2}$$

Thus the differential $\mathcal{T}_N^i$ spectrum corresponds to the spectrum in the invariant mass for jet i, where $M_i^2 \to 0$ for a pencil like jet of massless partons.

In the limit where all the $\mathcal{T}_N^i$ are assumed to be parametrically comparable but small compared to $Q_i \sim Q$, the factorized form for the cross section is

$$\begin{aligned} &\frac{\mathrm{d}\sigma}{\mathrm{d}\mathcal{T}_N^a \, \mathrm{d}\mathcal{T}_N^b \cdots \mathrm{d}\mathcal{T}_N^N} \\ &\quad = \int \mathrm{d}x_a \mathrm{d}x_b \int \mathrm{d}^4 q \, \mathrm{d}\Phi_L(q) \int \mathrm{d}\Phi_N(\{q_J\}) \, M_N(\Phi_N, \Phi_L) \\ &\qquad \times (2\pi)^4 \delta^4\big(q_a + q_b - q_1 - \cdots - q_N - q\big) \\ &\qquad \times \sum_\kappa \int \mathrm{d}t_a \, B_{\kappa_a}(t_a, x_a, \mu) \int \mathrm{d}t_b \, B_{\kappa_b}(t_b, x_b, \mu) \prod_{J=1}^N \int \mathrm{d}s_J \, J_{\kappa_J}(s_J, \mu) \\ &\qquad \times \vec{C}_N^{\kappa\dagger}(\Phi_N, \Phi_L, \mu) \widehat{S}_N^\kappa \left(\mathcal{T}_N^a - \frac{t_a}{Q_a}, \mathcal{T}_N^b - \frac{t_b}{Q_b}, \left\{ \mathcal{T}_N^j - \frac{s_j}{Q_j} \right\}, \{\hat{q}_i\}, \mu \right) \vec{C}_N^\kappa(\Phi_N, \Phi_L, \mu) \,. \end{aligned} \tag{4.3}$$

Here, $\Phi_N(\{q_J\})$ denotes the N-body massless phase space for the N reference jet momenta $\{q_J\}$, while $\Phi_L(q)$ is the "leptonic" phase space for any additional nonhadronic particles in the final state, whose total momentum is q. The measurement function $M_N(\Phi_N, \Phi_L)$

enforces all N jets to be energetic and well enough separated so that $\hat{s}_{ij} \gg \mathcal{T}_N/Q$. The index κ runs over all relevant partonic channels, with $\kappa_a, \kappa_b, \ldots, \kappa_N$ denoting the individual parton types. In the soft function arguments, the index j runs over all the jets $j \in \{1, \ldots, N\}$ and the index i also includes the beams $i \in \{a, b, 1, \ldots, N\}$.

The hard Wilson coefficient $\vec{C}_N^\kappa$ is a vector in the appropriate color space of the external hard partons in each partonic channel. It only depends on the hard phase-space variables Φ_N and Φ_L. The soft function $\widehat{S}_N^\kappa$ is a matrix in the same color space. We can rewrite the color contraction as

$$\vec{C}_N^\dagger \widehat{S}_N \vec{C}_N = \mathrm{tr}(\vec{C}_N \vec{C}_N^\dagger \widehat{S}_N) = \mathrm{tr}(\widehat{H}_N \widehat{S}_N)\,, \tag{4.4}$$

so the hard function $\widehat{H}_N = \vec{C}_N \vec{C}_N^\dagger$ is also a color-space matrix.

We want to compute the N-jettiness soft function

$$\widehat{S}_N^\kappa\big(k_a, k_b, k_1, \ldots, k_N, \{\hat{q}_i\}, \mu\big)\,. \tag{4.5}$$

The k_i are the soft contributions to the $\mathcal{T}_N^i$, so from Eq. (3.10) we have

$$k_i = 2\hat{q}_i \cdot \Bigg[\sum_{k \in \mathrm{soft}} p_k \prod_{j \neq i} \theta\big(\hat{q}_j \cdot p_k - \hat{q}_i \cdot p_k\big)\Bigg]\,, \tag{4.6}$$

where the sum now only runs over soft momenta. As indicated by the second to last argument in Eq. (4.5), the soft function still depends on all the reference momenta $\{\hat{q}_i\}$, because they enter in the definition of the measured soft momentum components in Eq. (4.6). The soft function is defined by the vacuum matrix element

$$\widehat{S}_N^\kappa\big(k_a, k_b, k_1, \ldots, k_N, \{\hat{q}_i\}\big) = \Big\langle 0 \Big| \widehat{Y}^{\kappa\dagger}(\{\hat{q}_i\}) \prod_i \delta(k_i - 2\hat{q}_i \cdot \hat{P}_i)\, \widehat{Y}^\kappa(\{\hat{q}_i\}) \Big| 0 \Big\rangle\,, \tag{4.7}$$

where the $\hat{P}_i$ denotes the momentum operator that picks out the total momentum in region i. Here, $\widehat{Y}^\kappa(\{\hat{q}_i\})$ denotes a product of eikonal Wilson lines in the $\hat{q}_i$ directions in the appropriate path-ordering and color representation of the external partons in the partonic channel κ. The $\widehat{Y}^{\kappa\dagger}$ and $\widehat{Y}^\kappa$ are matrices multiplied in color space. We take their overall normalization to be such that the tree level result for $\widehat{S}_N^\kappa$ is $\mathbf{1} \prod_i \delta(k_i)$, where $\mathbf{1}$ is the color identity operator (see Eq. (4.14) below).

In the following, we will often use the short-hand notation

$$\widehat{S}_N^\kappa(\{k_i\},\mu) \equiv \widehat{S}_N^\kappa(k_a,k_b,k_1,\dots,k_N,\{\hat{q}_i\},\mu)\,, \tag{4.8}$$

and similarly for other functions that depend on all k_i, such as the anomalous dimension and counterterm for the soft function.

4.1.2 Soft-function RGE

To derive the structure of the renormalization-group equation (RGE) and anomalous dimension of the soft function $\widehat{S}_N^\kappa(k_a,...,\mu)$, we can use the fact that the factorized cross section in Eq. (4.3) is independent of the renormalization scale μ. For this purpose we can ignore the phase-space integrals and only consider the last two lines in Eq. (4.3). To simplify the notation, we suppress the index κ and the momentum dependence on the label momenta from here on.

As already mentioned, the hard Wilson coefficient $\vec{C}_N$ is a vector in the color space of the external hard partons, so its anomalous dimension $\widehat{\gamma}_N$ is a matrix in color space. For 1-jettiness (or e^+e^- 3-jettiness), the external partons are $q^\alpha\bar{q}^\beta g^a$, so the only possible color structure is $T^a_{\alpha\beta}$ and the color space becomes one-dimensional. For $q^\alpha\bar{q}^\beta g^a g^b$ there are already three different color structures $\vec{T}^{ab}_{\alpha\beta} = \{(T^aT^b)_{\alpha\beta}, (T^bT^a)_{\alpha\beta}, \delta^{ab}\delta_{\alpha\beta}\}$, and so on.

The hard Wilson coefficient $\vec{C}_N$ from matching QCD onto SCET satisfies the RGE[1]

$$\mu\frac{\mathrm{d}}{\mathrm{d}\mu}\vec{C}_N(\mu) = \widehat{\gamma}_C(\mu)\,\vec{C}_N(\mu)\,. \tag{4.9}$$

Its anomalous dimension has the general form [16, 23]

$$\widehat{\gamma}_C^\dagger(\mu) = -\Gamma_{\mathrm{cusp}}[\alpha_s(\mu)]\sum_{i<j}\overline{T}_i\cdot\overline{T}_j\ln\Big[(-1)^{\Delta_{ij}}\frac{2q_i\cdot q_j}{\mu^2}-\mathrm{i}0\Big] + \widehat{\gamma}_C^\dagger[\alpha_s(\mu)]\,, \tag{4.10}$$

where we define $\Delta_{ij}=1$ if i and j are both incoming or both outgoing partons and $\Delta_{ij}=0$ if one of them is incoming and the other one outgoing, and with our conventions $q_i\cdot q_j$ is always positive. Here, $\Gamma_{\mathrm{cusp}}(\alpha_s)$ is the universal cusp anomalous dimension [41],

$$\Gamma_{\mathrm{cusp}}(\alpha_s) = \frac{\alpha_s}{4\pi}\,4 + \mathcal{O}(\alpha_s^2)\,. \tag{4.11}$$

[1]Throughout this work we use the convention $\mathcal{L}_{\mathrm{eff}} = \vec{C}_N^\dagger\cdot\vec{\mathcal{O}}_N$ for N-jet operators in the SCET Lagrangian.

The $\overline{T}_i^a$ denotes the color charge of the ith external particle when coupling to a gluon with color a. It acts on the external color space as

$$\begin{aligned}
(\overline{T}_i^a\,\vec{T})_{\cdots\alpha_i\cdots} &= T^a_{\alpha_i\beta_i}\,\vec{T}_{\cdots\beta_i\cdots}\,,\\
(\overline{T}_i^a\,\vec{T})_{\cdots\alpha_i\cdots} &= -T^a_{\beta_i\alpha_i}\,\vec{T}_{\cdots\beta_i\cdots}\,,\\
(\overline{T}_i^a\,\vec{T})^{\cdots a_i\cdots} &= \mathrm{i}f^{a_i a b_i}\,\vec{T}^{\cdots b_i\cdots}\,,
\end{aligned} \tag{4.12}$$

where the first line is for the ith particle being an outgoing quark or incoming antiquark, the second line for an incoming quark or outgoing antiquark, and the third line for a gluon. The product

$$\overline{T}_i\cdot\overline{T}_j = \sum_a \overline{T}_i^a\overline{T}_j^a\,, \tag{4.13}$$

appearing in the first term in Eq. (4.10), thus represents a particular color-space matrix $\widehat{T}_{ij}$ for each choice of i and j. We also define the identity operator $\mathbf{1}$, which acts as

$$(\mathbf{1}\,\vec{T})^{\cdots a_i\cdots}_{\cdots\alpha_j\cdots} = \vec{T}^{\cdots a_i\cdots}_{\cdots\alpha_j\cdots}\,. \tag{4.14}$$

In particular

$$\overline{T}_i^2 = \mathbf{1}\,C_i \quad \text{where} \quad C_q = C_{\bar{q}} = C_F\,, \quad C_g = C_A\,. \tag{4.15}$$

With only three partons, $q^\alpha\bar{q}^\beta g^a$, the only possible color structure is $T^a_{\alpha\beta}$, so in this case the color matrices are just numbers,

$$\begin{aligned}
\mathbf{1} &= 1\,, & \overline{T}_q^2 = \overline{T}_{\bar{q}}^2 &= C_F\,, & \overline{T}_g^2 &= C_A\,,\\
\overline{T}_q\cdot\overline{T}_{\bar{q}} &= \frac{C_A}{2} - C_F\,, & \overline{T}_q\cdot\overline{T}_g = \overline{T}_{\bar{q}}\cdot\overline{T}_g &= -\frac{C_A}{2}\,.
\end{aligned} \tag{4.16}$$

Up to two loops [47] (and maybe more [15, 16, 27, 36]), the non-cusp term, $\widehat{\gamma}_C(\alpha_s)$, in Eq. (4.10) is diagonal in color and given by a sum over individual quark and gluon contributions,

$$\begin{aligned}
\widehat{\gamma}_C(\alpha_s) &= \mathbf{1}\sum_i \gamma_C^i(\alpha_s) + \mathcal{O}(\alpha_s^3)\,,\\
\gamma_C^q(\alpha_s) = \gamma_C^{\bar{q}}(\alpha_s) &= -\frac{\alpha_s}{4\pi}\,3C_F + \mathcal{O}(\alpha_s^2)\,,\\
\gamma_C^g(\alpha_s) &= -\frac{\alpha_s}{4\pi}\,\beta_0 + \mathcal{O}(\alpha_s^2)\,.
\end{aligned} \tag{4.17}$$

The RGEs for the beam and jet functions are

$$\mu \frac{\mathrm{d}}{\mathrm{d}\mu} B_i(t,x,\mu) = \int \mathrm{d}t'\, \gamma_B^i(t-t',\mu)\, B_i(t',x,\mu)\,,$$
$$\mu \frac{\mathrm{d}}{\mathrm{d}\mu} J_i(s,\mu) = \int \mathrm{d}s'\, \gamma_J^i(s-s',\mu)\, J_i(s',\mu)\,. \tag{4.18}$$

The beam and jet anomalous dimension are identical to all orders [56], and are given by

$$\gamma_B^i(s,\mu) = \gamma_J^i(s,\mu) = -2\, C_i\, \Gamma_{\mathrm{cusp}}[\alpha_s(\mu)]\, \frac{1}{\mu^2} \mathcal{L}_0\Big(\frac{s}{\mu^2}\Big) + \gamma_J^i[\alpha_s(\mu)]\, \delta(s)\,, \tag{4.19}$$

with

$$\gamma_J^q(\alpha_s) = \gamma_J^{\bar{q}}(\alpha_s) = \frac{\alpha_s}{4\pi}\, 6C_F + \mathcal{O}(\alpha_s^2)\,,$$
$$\gamma_J^g(\alpha_s) = \frac{\alpha_s}{4\pi}\, 2\beta_0 + \mathcal{O}(\alpha_s^2)\,, \tag{4.20}$$

and $\mathcal{L}_n(x)$ denotes the standard plus distribution,

$$\mathcal{L}_n(x) = \left[\frac{\theta(x)\ln^n x}{x}\right]_+ . \tag{4.21}$$

Taking the derivative of Eq. (4.3) with respect to μ, we now require

$$0 = \mu \frac{\mathrm{d}}{\mathrm{d}\mu} \int \Big[\prod_i \mathrm{d}s_i\, \mathcal{J}_i(s_i,\mu)\Big] \vec{C}_N^\dagger(\mu)\, \widehat{S}_N\Big(\Big\{\mathcal{T}_N^i - \frac{s_i}{Q_i}\Big\},\mu\Big) \vec{C}_N(\mu)\,, \tag{4.22}$$

where we use $\mathcal{J}_i(s_i,\mu)$ to denote either beam or jet functions (with $s_{a,b} \equiv t_{a,b}$), since their RGEs are identical, and as before $i = a, b, 1, \ldots, N$. Using Eqs. (4.9) and (4.18) together with Eq. (4.22), we get

$$\begin{aligned} 0 = \int \Big[\prod_i \mathrm{d}s_i\, \mathrm{d}s_i'\, \mathcal{J}_i(Q_i\mathcal{T}_N^i - s_i',\mu)\Big] \Bigg\{ \Big[\sum_i \gamma_J^i(s_i'-s_i,\mu) \prod_{j\neq i} \delta(s_j'-s_j)\Big] \widehat{S}_N\Big(\Big\{\frac{s_i}{Q_i}\Big\},\mu\Big) \\ + \Big[\prod_i \delta(s_i'-s_i)\Big] \Big[\widehat{\gamma}_C^\dagger(\mu)\, \widehat{S}_N\Big(\Big\{\frac{s_i}{Q_i}\Big\},\mu\Big) + \widehat{S}_N\Big(\Big\{\frac{s_i}{Q_i}\Big\},\mu\Big)\, \widehat{\gamma}_C(\mu) + \mu \frac{\mathrm{d}}{\mathrm{d}\mu} \widehat{S}_N\Big(\Big\{\frac{s_i}{Q_i}\Big\},\mu\Big)\Big] \Bigg\}\,, \end{aligned} \tag{4.23}$$

where we divided out the Wilson coefficients and shifted the integration variables $s_i \to$

$Q_i\mathcal{T}_N^i - s_i$ and $s_i' \to Q_i\mathcal{T}_N^i - s_i'$. We can now multiply by $\prod_i \mathcal{J}_i^{-1}(Q_i k_i - Q_i\mathcal{T}_N^i, \mu)$ and integrate over $\mathcal{T}_N^i$, which replaces $\mathcal{J}_i(Q_i\mathcal{T}_N^i - s_i', \mu) \to \delta(Q_i k_i - s_i')/Q_i$. Renaming $k_i' = s_i/Q_i$, we obtain

$$\begin{aligned}
&\mu\frac{\mathrm{d}}{\mathrm{d}\mu}\widehat{S}_N(\{k_i\},\mu) \\
&\quad = \int\Big[\prod_i \mathrm{d}k_i'\Big]\frac{1}{2}\Big[\widehat{\gamma}_S(\{k_i-k_i'\},\mu)\,\widehat{S}_N(\{k_i'\},\mu) + \widehat{S}_N(\{k_i'\},\mu)\,\widehat{\gamma}_S^\dagger(\{k_i-k_i'\},\mu)\Big]\,, \qquad (4.24)
\end{aligned}$$

where the soft anomalous dimension is given by

$$\begin{aligned}
&\widehat{\gamma}_S(\{k_i\},\mu) \\
&\quad = -\mathbf{1}\sum_i Q_i\gamma_J^i(Q_ik_i,\mu)\prod_{j\neq i}\delta(k_j) - 2\widehat{\gamma}_C^\dagger(\mu)\prod_i\delta(k_i) \\
&\quad = 2\Gamma_{\text{cusp}}[\alpha_s(\mu)]\Big\{\sum_i \overline{T}_i^2\,\frac{Q_i}{\mu^2}\mathcal{L}_0\Big(\frac{Q_ik_i}{\mu^2}\Big)\prod_{j\neq i}\delta(k_j) \\
&\qquad + \sum_{i<j}\overline{T}_i\cdot\overline{T}_j\ln\Big[(-1)^{\Delta_{ij}}\frac{2q_i\cdot q_j}{\mu^2} - \mathrm{i}0\Big]\prod_i\delta(k_i)\Big\} \\
&\qquad - \Big\{\mathbf{1}\sum_i\gamma_J^i[\alpha_s(\mu)] + 2\widehat{\gamma}_C^\dagger[\alpha_s(\mu)]\Big\}\prod_i\delta(k_i) \\
&\quad = -2\Gamma_{\text{cusp}}[\alpha_s(\mu)]\sum_{i\neq j}\overline{T}_i\cdot\overline{T}_j\left[\frac{1}{\sqrt{\hat{s}_{ij}}\,\mu}\mathcal{L}_0\Big(\frac{k_i}{\sqrt{\hat{s}_{ij}}\,\mu}\Big) + \frac{\mathrm{i}\pi}{2}\Delta_{ij}\,\delta(k_i)\right]\prod_{m\neq i}\delta(k_m) \\
&\qquad + \widehat{\gamma}_S[\alpha_s(\mu)]\prod_i\delta(k_i)\,, \qquad (4.25)
\end{aligned}$$

with the non-cusp part

$$\begin{aligned}
\widehat{\gamma}_S(\alpha_s) &= -\mathbf{1}\sum_i\gamma_J^i(\alpha_s) - 2\widehat{\gamma}_C^\dagger(\alpha_s) \\
&= -\mathbf{1}\sum_i\big[\gamma_J^i(\alpha_s) + 2\gamma_C^i(\alpha_s)\big] + \mathcal{O}(\alpha_s^3) \\
&= 0 + \mathcal{O}(\alpha_s^2)\,. \qquad (4.26)
\end{aligned}$$

In the last step above we rescaled the plus distribution $\lambda\mathcal{L}_0(\lambda x) = \mathcal{L}_0(x) + \ln\lambda\,\delta(x)$, and applied color identities like

$$\sum_i x_i\overline{T}_i^2 = -\sum_{i\neq j}x_i\overline{T}_i\cdot\overline{T}_j = -\sum_{i<j}(x_i+x_j)\overline{T}_i\cdot\overline{T}_j\,, \qquad (4.27)$$

which follows from color conservation, $\sum_i \overline{T}_i = 0$.

This derivation shows that factorization implies that the kinematic dependence of the soft anomalous dimension $\widehat{\gamma}_S(\{k_i\},\mu)$ on k_i is separable into individual contributions to all orders. This generalizes the same result obtained for the special case of the hemisphere (i.e. e^+e^- 2-jettiness) soft function in Ref. [34], which is reproduced by Eq. (4.25) using $\overline{T}_i \cdot \overline{T}_j = -C_F$ and $2\hat{q}_i \cdot \hat{q}_j = 1$.

Since in Eq. (4.25) $\Gamma_{\rm cusp}(\alpha_s)$, $\gamma_J(\alpha_s)$, and $\widehat{\gamma}_C(\alpha_s)$ are all known to two loops, so is $\widehat{\gamma}_S(\{k_i\},\mu)$. The general evolution formula in Eq. (4.24) leaves $\widehat{S}_N$ hermitian, which from Eq. (4.3) is the only requirement to obtain a real cross section.

4.1.3 Renormalization and One-Loop Divergences

The result for the soft anomalous dimension allows us to infer the one-loop counterterm for the soft function in $\overline{\rm MS}$, which we will need in our calculation to renormalize the bare soft function. This will provide us with a nontrivial cross check on our calculation.

The structure of the anomalous dimension implies that the bare and $\overline{\rm MS}$ renormalized soft functions are related by

$$\widehat{S}_N^{\rm bare}(\{k_i\}) = \int \Big[\prod_i \mathrm{d}k_i' \,\mathrm{d}k_i''\Big]\, \widehat{Z}_S(\{k_i'\},\mu)\, \widehat{S}_N(\{k_i - k_i' - k_i''\},\mu)\, \widehat{Z}_S^\dagger(\{k_i''\},\mu)\,. \tag{4.28}$$

The bare soft function is independent of μ, so differentiating both sides with respect to μ determines the soft anomalous dimension in terms of the counterterm,

$$\begin{aligned}\widehat{\gamma}_S(\{k_i\},\mu) &= -2\int \Big[\prod_i \mathrm{d}k_i'\Big] (\widehat{Z}_S)^{-1}(\{k_i - k_i'\},\mu)\, \mu\frac{\mathrm{d}}{\mathrm{d}\mu}\widehat{Z}_S(\{k_i'\},\mu) \\ &= -2\,\mu\frac{\mathrm{d}}{\mathrm{d}\mu}\widehat{Z}_S(\{k_i'\},\mu) + \mathcal{O}(\alpha_s^2)\,. \end{aligned} \tag{4.29}$$

Using Eqs. (4.25) and (4.26), the NLO counterterm is thus given by

$$\begin{aligned}\widehat{Z}_S(\{k_i\},\mu) = \mathbf{1}\prod_i \delta(k_i) - \frac{\alpha_s(\mu)}{2\pi}\,\frac{1}{\epsilon}\sum_{i\neq j}\overline{T}_i\cdot\overline{T}_j\bigg[-\frac{1}{2\epsilon}\,\delta(k_i) \\ + \frac{1}{\sqrt{\hat{s}_{ij}}\,\mu}\mathcal{L}_0\bigg(\frac{k_i}{\sqrt{\hat{s}_{ij}}\,\mu}\bigg) + \frac{\mathrm{i}\pi}{2}\Delta_{ij}\,\delta(k_i)\bigg]\prod_{m\neq i}\delta(k_m) + \mathcal{O}(\alpha_s^2)\,. \end{aligned} \tag{4.30}$$

Note that since $\widehat{S}_N$ is color diagonal at tree level, the imaginary part of $\widehat{Z}_S$ does not

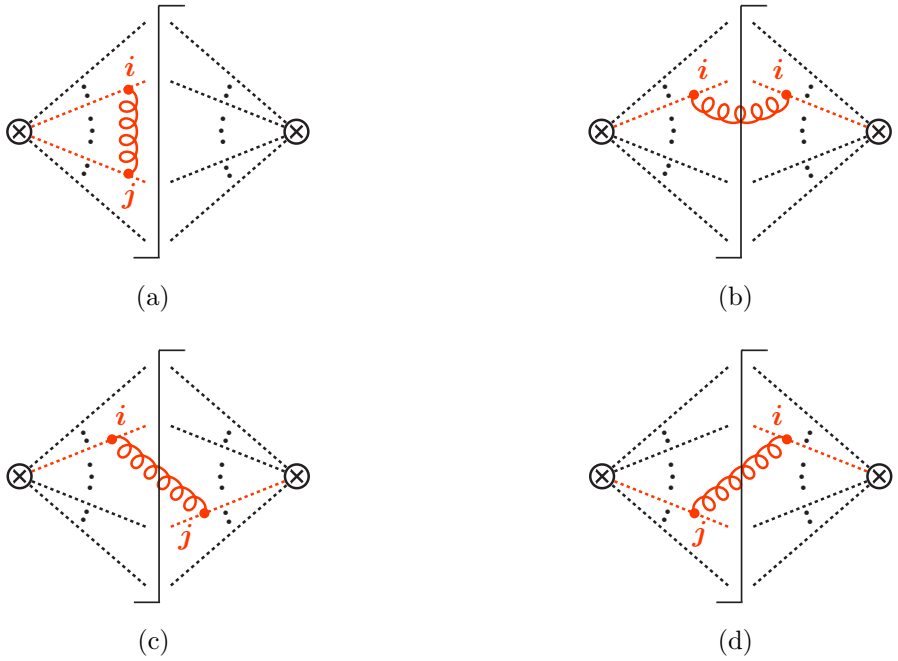

Figure 4-1: One-loop diagrams for $\widehat{S}_N$. The vertical line denotes the final-state cut. Diagrams (a) and (b) vanish. Diagrams (c) and (d) yield Eq. (4.32).

contribute in Eq. (4.28) at NLO, because it cancels between $\widehat{Z}_S$ and $\widehat{Z}_S^\dagger$. Hence, from Eq. (4.30) we expect the UV-divergent parts of the one-loop bare soft function, $\widehat{S}_N^{\text{bare}(1)}$, to have the form

$$\widehat{S}_N^{\text{bare}(1)}(\{k_i\}) = -\frac{\alpha_s(\mu)}{\pi}\frac{1}{\epsilon}\sum_{i\neq j}\overline{T}_i\cdot\overline{T}_j\,\frac{(\hat{s}_{ij}\,\mu^2)^\epsilon}{k_i^{1+2\epsilon}}\prod_{m\neq i}\delta(k_m)+\mathcal{O}(\epsilon^0)\,. \tag{4.31}$$

This implies that the UV divergences are given for any N by a simple sum over individual hemisphere contributions. We will see how this happens explicitly in the next section.

4.2 NLO Calculation

4.2.1 General Setup

Our calculation in the following applies to both hadronic and e^+e^- collisions, i.e. it is independent of whether the Wilson lines are in- or outgoing. For simplicity we use the term "jet" to refer to both beam jets and central jets.

The one-loop diagrams for the soft function are shown in Fig. 4-1, where i and j label any two Wilson lines, and we work in Feynman gauge. The virtual diagrams, which are

shown in Fig. 4-1(a), are scaleless and thus vanish in pure dimensional regularization. The real emission diagrams in Fig. 4-1(b) with the gluon attaching to the same Wilson line vanish, as it is proportional to $\hat{q}_i^2 = 0$. Hence, at one loop we can write the bare soft function as a sum over contributions where the intermediate gluon attaches to the ith and jth Wilson line as shown in Figs. 4-1(c) and 4-1(d),

$$\begin{aligned}&\widehat{S}_N^{\text{bare}(1)}(\{k_i\}) \\ &\quad = -2\sum_{i<j} \overline{T}_i \cdot \overline{T}_j \left(\frac{e^{\gamma_E}\mu^2}{4\pi}\right)^{\epsilon} g^2 \int \frac{\mathrm{d}^d p}{(2\pi)^d} \frac{\hat{q}_i \cdot \hat{q}_j}{(\hat{q}_i \cdot p)(\hat{q}_j \cdot p)} \, 2\pi\delta(p^2)\,\theta(p^0)\, F(\{k_i\}, \{2\hat{q}_i \cdot p\})\,.\end{aligned} \tag{4.32}$$

The key idea in the hemisphere decomposition method is to first fix i and j and then analyze the remaining integral. The measurement function resulting from Eq. (4.6), which measures the contribution of the gluon in the final state to k^i, is given by

$$F(\{k_i\}, \{p^i\}) = \sum_m \delta(k_m - p^m) \prod_{l \neq m} \delta(k_l)\,\theta(p^l - p^m)\,, \tag{4.33}$$

where we denote the component of the gluon momentum p^μ along the jet direction $\hat{q}_i^\mu$ as

$$p^i = 2\hat{q}_i \cdot p\,. \tag{4.34}$$

For example, for 1-jettiness (or e^+e^- 3-jettiness) we have three independent labels $i \neq j \neq m$, so

$$\begin{aligned}F(\{k_i\}, \{p^i\}) = {}& \delta(k_i - p^i)\,\delta(k_j)\,\delta(k_m)\,\theta(p^j - p^i)\,\theta(p^m - p^i) \\ &+ \delta(k_i)\,\delta(k_j - p^j)\,\delta(k_m)\,\theta(p^i - p^j)\,\theta(p^m - p^j) \\ &+ \delta(k_i)\,\delta(k_j)\,\delta(k_m - p^m)\,\theta(p^i - p^m)\,\theta(p^j - p^m)\,.\end{aligned}$$

The first two terms correspond to the case where the gluon emitted from the ith and jth Wilson line ends up in the region of jet i or jet j, respectively. In this case, p can become collinear with either $\hat{q}_i$ or $\hat{q}_j$, resulting in a double UV-IR divergence. In the last term, the gluon is in the remaining jet m. In this case, both $p^i > p^m$ and $p^j > p^m$ are bounded from below, so there is only a single soft IR divergence. The virtual diagrams, which vanish in pure dimensional regularization, turn all IR divergences into UV divergences.

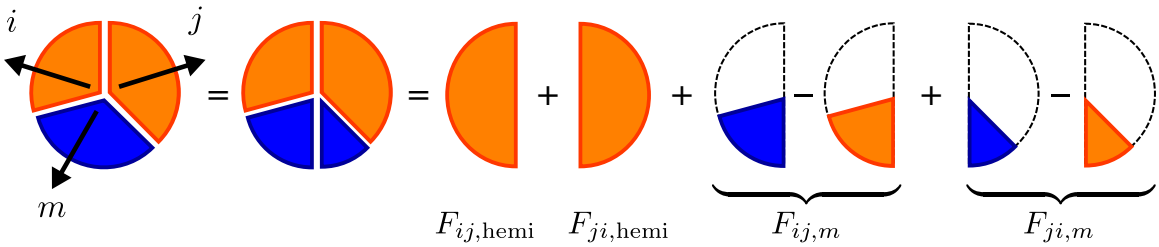

Figure 4-2: Separation of the measurement function into hemisphere and non-hemisphere measurement functions for 1-jettiness or e^+e^- 3-jettiness for a gluon emitted from the ith and jth Wilson line. The phase space is divided into i and j hemispheres into which the third jet region m is split.

To combine the divergences from the different jet regions, we split the region of jet m into the two hemispheres $p^i < p^j$ and $p^i > p^j$ defined by the directions of jets i and j,

$$\begin{aligned}
&F(\{k_i\},\{p^i\}) \\
&\quad = \theta(p^j - p^i)\Big[\delta(k_i - p^i)\,\delta(k_m)\,\theta(p^m - p^i) + \delta(k_i)\,\delta(k_m - p^m)\,\theta(p^i - p^m)\Big]\delta(k_j) + (i \leftrightarrow j) \\
&\quad = \delta(k_i - p^i)\,\delta(k_j)\,\theta(p^j - p^i)\,\delta(k_m) \\
&\qquad + \Big[\delta(k_i)\,\delta(k_m - p^m) - \delta(k_i - p^i)\,\delta(k_m)\Big]\,\delta(k_j)\,\theta(p^j - p^i)\,\theta(p^i - p^m) + (i \leftrightarrow j) \\
&\quad \equiv F_{ij,\text{hemi}}(\{k_i\},\{p^i\}) + F_{ji,\text{hemi}}(\{k_i\},\{p^i\}) + F_{ij,m}(\{k_i\},\{p^i\}) + F_{ji,m}(\{k_i\},\{p^i\})\,.
\end{aligned} \tag{4.35}$$

In the second step we replaced $\theta(p^m - p^i) = 1 - \theta(p^i - p^m)$ in the first term to extend the region for jet i to the full $p^i < p^j$ hemisphere, which gives the hemisphere measurement function

$$F_{ij,\text{hemi}}(\{k_i\},\{p^i\}) = \delta(k_i - p^i)\,\delta(k_j)\,\theta(p^j - p^i)\,\delta(k_m)\,. \tag{4.36}$$

The contribution for $p^m < p^i < p^j$, which overlaps with the region for jet m, is subtracted in the second term, which gives the non-hemisphere measurement function for region m,

$$\begin{aligned}
&F_{ij,m}(\{k_i\},\{p^i\}) \\
&\qquad = \Big[\delta(k_i)\,\delta(k_m - p^m) - \delta(k_i - p^i)\,\delta(k_m)\Big]\,\delta(k_j)\,\theta(p^j - p^i)\,\theta(p^i - p^m)\,.
\end{aligned} \tag{4.37}$$

This splitting up of the measurement function is illustrated in Fig. 4-2. The integrations over the i and j hemispheres resulting from $F_{ij,\text{hemi}}$ and $F_{ji,\text{hemi}}$ will now contain all divergences, while the integration over region m resulting from $F_{ij,m}$ and $F_{ji,m}$ will be UV

and IR finite, as we will see explicitly below. Essentially, the restriction of the emitted and measured gluon to stay away from the i and j directions, $p^{i,j} > p^m$, cuts off the UV divergence, while the subtraction of the overlapping hemisphere contribution removes the soft divergence: In the soft limit, both $p^i \to 0$ and $p^m \to 0$, and the two terms in square brackets in Eq. (4.37) cancel each other.

We will see in Sec. 4.2.5 (see Eq. (4.53) below) that this split up of the measurement function generalizes to any N. Hence, we write the renormalized soft function as

$$\widehat{S}_N(\{k_i\},\mu) = \mathbf{1}\prod_i \delta(k_i) + \sum_{i\neq j} \overline{T}_i \cdot \overline{T}_j \, S_{ij}^{(1)}(\{k_i\},\mu) + \mathcal{O}(\alpha_s^2)\,, \tag{4.38}$$

where we split the NLO contribution into a hemisphere and a non-hemisphere contribution, with the latter given by a sum over the different jet regions $m \neq i, j$,

$$S_{ij}^{(1)}(\{k_i\},\mu) = S_{ij,\mathrm{hemi}}^{(1)}(\{k_i\},\mu) + \sum_{m\neq i,j} S_{ij,m}^{(1)}(\{k_i\},\mu)\,. \tag{4.39}$$

Here, $S_{ij,\mathrm{hemi}}$ and $S_{ij,m}$ are the contributions corresponding to $F_{ij,\mathrm{hemi}}$ and $F_{ij,m}$ in Eq. (4.35).

It is instructive to compare our hemisphere decomposition with the method used in Ref. [30] to calculate the soft function for cone jets. There the authors first specify a jet region and then sum over all contributions from different gluon attachments for that fixed jet region. In the end they sum over the different jet regions. In this case there are nontrivial cancellations between the divergences (and finite terms) arising from the same gluon attachment contributing to different jets. In contrast, as seen from Eqs. (4.38) and (4.39), in the hemisphere decomposition we first specify a gluon attachment i, j and then sum over the contributions to the different jet regions m from this specific attachment. This allows us to make the cancellations explicit and to isolate the UV divergences into the hemisphere contributions. In the end we sum over all possible attachments.

4.2.2 Hemisphere Contributions

Using Eq. (4.32) and restricting the measurement function to the hemisphere contribution, $F_{ij,\mathrm{hemi}}$ in Eq. (4.35), we obtain

$$
\begin{aligned}
&S_{ij,\text{hemi}}^{\text{bare}(1)}(\{k_i\}) \\
&\quad = -2\Big(\frac{e^{\gamma_E}\mu^2}{4\pi}\Big)^{\epsilon} g^2 \int \frac{\mathrm{d}^d p}{(2\pi)^d}\, \frac{2\hat{s}_{ij}}{p^i\, p^j}\, 2\pi\delta(p^2)\,\theta(p^0)\,\delta(k_i - p^i)\,\delta(k_j)\,\theta(p^j - p^i)\,\delta(k_m) \\
&\quad = -\frac{\alpha_s(\mu)}{\pi}\,\frac{(e^{\gamma_E})^{\epsilon}}{\Gamma(1-\epsilon)}\big(\hat{s}_{ij}\,\mu^2\big)^{\epsilon} \int \mathrm{d}p^i\,\mathrm{d}p^j\,\frac{\theta(p^i)\,\theta(p^j)}{(p^i p^j)^{1+\epsilon}}\,\delta(k_i - p^i)\,\delta(k_j)\,\theta(p^j - p^i)\,\delta(k_m) \\
&\quad = -\frac{\alpha_s(\mu)}{\pi}\,\frac{1}{\epsilon}\,\frac{(e^{\gamma_E})^{\epsilon}}{\Gamma(1-\epsilon)}\big(\hat{s}_{ij}\,\mu^2\big)^{\epsilon}\,\frac{\theta(k_i)}{k_i^{1+2\epsilon}}\,\delta(k_j)\,\delta(k_m)\,. \qquad (4.40)
\end{aligned}
$$

In the second step we used the coordinate decomposition

$$
p^\mu = p^j\,\frac{\hat{q}_i^\mu}{\hat{s}_{ij}} + p^i\,\frac{\hat{q}_j^\mu}{\hat{s}_{ij}} + p_{ij\perp}^\mu \qquad (4.41)
$$

to rewrite the phase-space integral as

$$
\int \frac{\mathrm{d}^d p}{(2\pi)^d}\, 2\pi\delta(p^2)\,\theta(p^0) = \frac{(4\pi)^{\epsilon}}{(2\pi)^2\Gamma(1-\epsilon)}\,\frac{1}{4\hat{s}_{ij}} \int \mathrm{d}p^i\,\mathrm{d}p^j \Big(\frac{\hat{s}_{ij}}{p^i\,p^j}\Big)^{\epsilon}\,\theta(p^i)\,\theta(p^j)\,, \qquad (4.42)
$$

and in the last step we integrated over p^i and p^j. The result in Eq. (4.40) has the expected form in Eq. (4.31) and reproduces the correct counterterm and anomalous dimension. Expanding Eq. (4.40) and subtracting the $1/\epsilon$ divergences, we obtain the renormalized NLO hemisphere contribution

$$
S_{ij,\text{hemi}}^{(1)}(\{k_i\},\mu) = \frac{\alpha_s(\mu)}{4\pi}\left[\frac{8}{\sqrt{\hat{s}_{ij}}\,\mu}\mathcal{L}_1\Big(\frac{k_i}{\sqrt{\hat{s}_{ij}}\,\mu}\Big) - \frac{\pi^2}{6}\,\delta(k_i)\right]\delta(k_j)\,\delta(k_m)\,. \qquad (4.43)
$$

This generalizes the one-loop result for the hemisphere soft function for two back-to-back jets with equal energies from Refs. [34, 51] to general hemispheres defined by two jet directions $\hat{q}_i$ and $\hat{q}_j$. Note that, as expected from reparametrization invariance, the dependence on the jet directions only appears through the invariant $\hat{s}_{ij}$.

4.2.3 Non-Hemisphere Contributions

We now turn to the non-hemisphere contributions. The hemisphere contributions contain all the divergences but they do not include the full information about the boundaries between jet and beam regions. The effect of the boundaries is encoded in the non-hemisphere pieces.

Inserting the second part $F_{ij,m}$ in Eq. (4.35) into Eq. (4.32), we get

$$S_{ij,m}^{\mathrm{bare}(1)}(\{k_i\}) = -\frac{\alpha_s(\mu)}{\pi}\left(e^{\gamma_E} 2\hat{q}_i\cdot\hat{q}_j\mu^2\right)^{\epsilon}\int\frac{\mathrm{d}\Omega_{d-2}}{2\pi^{1-\epsilon}}\,\mathrm{d}p^i\,\mathrm{d}p^j\,\frac{\theta(p^i)\,\theta(p^j)}{(p^ip^j)^{1+\epsilon}} \tag{4.44}$$
$$\times\Big[\delta(k_i)\,\delta(k_m-p^m)-\delta(k_i-p^i)\,\delta(k_m)\Big]\delta(k_j)\,\theta(p^j-p^i)\,\theta(p^i-p^m)\,.$$

To perform the integration over p^i, we use the rescaled variable $x=p^j/p^i$, and rewrite p^m in terms of p^i, x, and the angle ϕ between $\vec{q}_{m\perp}$ and $\vec{p}_\perp$ in the transverse plane,

$$x=\frac{p^j}{p^i}\,,\qquad \frac{p^m}{p^i}=\frac{\hat{s}_{jm}}{\hat{s}_{ij}}+\frac{\hat{s}_{im}}{\hat{s}_{ij}}\,x-2\Big(\frac{\hat{s}_{jm}\hat{s}_{im}}{\hat{s}_{ij}^2}x\Big)^{1/2}\cos\phi\equiv z(x,\phi)\,. \tag{4.45}$$

The limit $p^m<p^i$ thus implies an upper limit on x, which eliminates the UV divergence for $x\to\infty$. In addition, since p^m scales like p^i, there is also no IR divergence in Eq. (4.44), because the term in square brackets vanishes in the limit $p^i\to 0$. The integral over p^i can then be performed without encountering any divergences,

$$\begin{aligned}&\mu^{2\epsilon}\int\mathrm{d}p^i\,\frac{\theta(p^i)}{(p^i)^{1+2\epsilon}}\Big[\delta(k_i)\,\delta(k_m-p^m)-\delta(k_i-p^i)\delta(k_m)\Big]\\&\quad=\delta(k_i)\,\frac{1}{\mu}\mathcal{L}_0\Big(\frac{k_m}{\mu}\Big)-\frac{1}{\mu}\mathcal{L}_0\Big(\frac{k_i}{\mu}\Big)\,\delta(k_m)-\ln[z(x,\phi)]\,\delta(k_i)\,\delta(k_m)\,.\end{aligned} \tag{4.46}$$

Note that the μ-dependence cancels between the first two terms. Taking $\epsilon\to 0$ everywhere else, we obtain the NLO non-hemisphere contribution

$$\begin{aligned}&S_{ij,m}^{(1)}(\{k_i\},\mu)\\&\quad=\frac{\alpha_s(\mu)}{\pi}\bigg\{I_0\Big(\frac{\hat{s}_{jm}}{\hat{s}_{ij}},\frac{\hat{s}_{im}}{\hat{s}_{ij}}\Big)\bigg[\frac{1}{\mu}\mathcal{L}_0\Big(\frac{k_i}{\mu}\Big)\,\delta(k_m)-\delta(k_i)\,\frac{1}{\mu}\mathcal{L}_0\Big(\frac{k_m}{\mu}\Big)+\ln\frac{\hat{s}_{jm}}{\hat{s}_{ij}}\,\delta(k_i)\,\delta(k_m)\bigg]\delta(k_j)\\&\qquad+I_1\Big(\frac{\hat{s}_{jm}}{\hat{s}_{ij}},\frac{\hat{s}_{im}}{\hat{s}_{ij}}\Big)\,\delta(k_i)\,\delta(k_j)\,\delta(k_m)\bigg\}\,.\end{aligned} \tag{4.47}$$

The remaining finite phase-space integrals are defined as (rescaling $x=y^2(\alpha/\beta)$ to simplify the integrands)

$$I_0(\alpha,\beta)=\frac{1}{\pi}\int_{-\pi}^{\pi}\mathrm{d}\phi\int\frac{\mathrm{d}y}{y}\,\theta\big(y-\sqrt{\beta/\alpha}\big)\,\theta\big(1/\alpha-1-y^2+2y\cos\phi\big)\,, \tag{4.48}$$
$$I_1(\alpha,\beta)=\frac{1}{\pi}\int_{-\pi}^{\pi}\mathrm{d}\phi\int\frac{\mathrm{d}y}{y}\,\ln(1+y^2-2y\cos\phi)\,\theta\big(y-\sqrt{\beta/\alpha}\big)\,\theta\big(1/\alpha-1-y^2+2y\,\cos\phi\big)\,.$$

In Eq. (4.47) they are evaluated at $\alpha = \hat{s}_{jm}/\hat{s}_{ij}$ and $\beta = \hat{s}_{im}/\hat{s}_{ij}$. Their numerical evaluation for fixed $\alpha > 0$ and $\beta > 0$ poses no problem. We were not able to find complete analytic expressions. Their analytic simplification to one-dimensional integrals is given in App. B, with the final result in Eq. (B.9).

4.2.4 Extension to Other Observables

As we have just seen, we can extract the divergences in the soft function by dividing up phase space into hemispheres corresponding to all possible pairings of Wilson lines. We will now generalize this decomposition to general IR-safe observables and to more than three regions (in which case the $\hat{q}_i$ are in general non-planar).

Consider a measurement that specifies a way to split up the angular phase space into non-overlapping regions. We use the notation $\Theta_i(p) = 1$ when the momentum p is inside region i and $\Theta_i(p) = 0$ otherwise. We require that the union of all regions covers all of phase space, and that each region contains at most one of the directions $\hat{q}_i$, i.e.

$$\sum_i \Theta_i(p) = 1\,, \qquad \Theta_i(\hat{q}_j) = \delta_{ij}\,. \tag{4.49}$$

We explicitly allow the possibility that there are regions that do not contain any of the $\hat{q}_i$, in which case there will be more than $N + 2$ regions.

In general, we can measure a different observable in each region. At NLO, we only need to know how the observable for each region i acts on a one-particle state with momentum p, which we denote by $f_i(p)$. We want f_i to be IR safe, which implies that $f_i(p \to 0)$ is equivalent to measuring no gluon at all. Without loss of generality we can assume that $f_i(0) = 0$. We will continue to denote the arguments of the soft function by k_i, which are now given by the soft contribution to f_i. With this notation, the generalization of the measurement function in Eq. (4.33) acting on a soft gluon with momentum p is

$$F(\{k_i\}, p) = \sum_m \delta[k_m - f_m(p)]\,\Theta_m(p) \prod_{l\neq m} \delta(k_l)\,. \tag{4.50}$$

We now want to generalize Eq. (4.35) by splitting up Eq. (4.50) into hemisphere and non-hemisphere contributions according to which Wilson lines the gluon attaches to. We continue to use the labels i and j for the directions of these two Wilson lines. The hemi-

spheres are still determined via the gluon momentum components $p^{i,j} = 2\hat{q}_{i,j} \cdot p$ by $p^j > p^i$ and $p^i > p^j$. Writing out Eq. (4.50) we now have

$$F(\{k_i\}, p) = \theta(p^j - p^i)\Big[\delta[k_i - f_i(p)] \prod_{l\neq i} \delta(k_l)\Theta_i(p) + \sum_{m\neq i} \delta[k_m - f_m(p)] \prod_{l\neq m} \delta(k_l)\,\Theta_m(p)\Big] + (i \leftrightarrow j)\,. \tag{4.51}$$

Note that region j is allowed to overlap with hemisphere i, and vice versa. Using Eq. (4.49), we have

$$\Theta_i(p) = 1 - \sum_{m\neq i} \Theta_m(p)\,, \tag{4.52}$$

which allows us to replace the regions i and j by full hemispheres analogous to Eq. (4.35), where the complement of $\Theta_i(p)$ is now split up between the remaining $\Theta_m(p)$ with $m \neq i$. Then Eq. (4.50) can be written as

$$F(\{k_i\}, p) = F_{ij,\text{hemi}}(\{k_i\}, p) + F_{ji,\text{hemi}}(\{k_i\}, p) + \sum_{m\neq i} F_{ij,m}(\{k_i\}, p) + \sum_{m\neq j} F_{ji,m}(\{k_i\}, p)\,, \tag{4.53}$$

where the hemisphere contributions are given by

$$F_{ij,\text{hemi}}(\{k_i\}, p) = \theta(p^j - p^i)\,\delta[k_i - f_i(p)] \prod_{l\neq i} \delta(k_l)\,, \tag{4.54}$$

and the non-hemisphere contributions by

$$F_{ij,m}(\{k_i\}, p) = \theta(p^j - p^i)\,\Theta_m(p) \prod_{l\neq i,m} \delta(k_l)\big\{\delta(k_i)\,\delta[k_m - f_m(p)] - \delta[k_i - f_i(p)]\,\delta(k_m)\big\}\,. \tag{4.55}$$

As in Sec. 4.2.3, all the divergences are contained in the hemisphere contributions, while the non-hemisphere contributions are UV and IR finite. The measurement of either f_i or f_m in Eq. (4.55) fixes the magnitude of p, while the restriction of the emitted gluon to region m forces it to stay away from the i and j directions. Taken together this eliminates the UV divergence. The IR-safety of f_i then ensures that in the limit $p \to 0$ the terms in

curly brackets in Eq. (4.55) cancel each other, which eliminates the IR divergence. As a result, for any set of IR-safe observables f_i all UV divergences, and hence the anomalous dimension, are contained in the hemisphere contributions determined by Eq. (4.54). Depending on the observable, these contributions can be more complicated than in Eq. (4.43). Note that this result depends on the fact that an observable f_i is measured in each region i. If we have a region u where only an angular restriction is imposed by $\Theta_u(p)$, the corresponding $\delta[k_u - f_u(p)]$ is absent (an "unmeasured jet" in the language of Ref. [29]). In this case the hemisphere contributions $S_{uj,\text{hemi}}$ are scaleless and vanish. The non-hemisphere contributions $S_{uj,m}$ and $S_{ij,u}$ are still IR-finite, but now contain a UV divergence in the term coming from region u, for which the magnitude of p is not fixed anymore. In this case, the factorization structure is different and the soft anomalous dimension depends on the parameters determining the boundary of region u, for example the cone radius as in Ref. [29].

Although we have only applied the hemisphere decomposition method at NLO, the N-jettiness factorization theorem implies that the UV divergences and soft anomalous dimensions factor into pairwise hemisphere contributions to all orders, as shown by Eq. (4.25). Hence, we believe the hemisphere decomposition will remain useful also at higher orders.

4.2.5 NLO Calculation for N-Jettiness

We now use the general arguments in the previous subsection and apply them to the case of N-jettiness. In this case the observables are simply the components of the gluon momentum along the jet directions, while the regions are determined by the smallest p^i. Hence,

$$f_i(p) = p^i = 2\hat{q}_i \cdot p\,, \qquad \Theta_i(p) = \prod_{m\neq i} \theta(p^m - p^i)\,, \tag{4.56}$$

which turns Eq. (4.50) into Eq. (4.33). From Eqs. (4.54) and (4.55) we get

$$F_{ij,\text{hemi}}(\{k_i\},\{p^i\}) = \theta(p^j - p^i)\,\delta(k_i - p^i)\,\prod_{m\neq i}\delta(k_m)\,, \tag{4.57}$$

and

$$F_{ij,m}(\{k_i\},\{p^i\}) \tag{4.58}$$
$$= \big[\delta(k_i)\,\delta(k_m - p^m) - \delta(k_i - p^i)\,\delta(k_m)\big]\theta(p^j - p^i)\,\theta(p^i - p^m)\prod_{l\neq i,m}\delta(k_l)\,\theta(p^l - p^m)\,.$$

The calculation of the hemisphere contribution for general N is identical to the 1-jettiness case in Sec. 4.2.2 with the overall replacement $\delta(k_j)\,\delta(k_m) \to \prod_{m\neq i}\delta(k_m)$ arising from Eq. (4.57). In particular, we can see immediately that this reproduces the correct NLO counterterm and soft anomalous dimension in Eqs. (4.30) and (4.25). The final result for the renormalized hemisphere contribution is given by Eq. (4.43),

$$S^{(1)}_{ij,\mathrm{hemi}}(\{k_i\},\mu) = \frac{\alpha_s(\mu)}{4\pi}\left[\frac{8}{\sqrt{\hat{s}_{ij}}\,\mu}\mathcal{L}_1\Big(\frac{k_i}{\sqrt{\hat{s}_{ij}}\,\mu}\Big) - \frac{\pi^2}{6}\,\delta(k_i)\right]\prod_{m\neq i}\delta(k_m)\,. \tag{4.59}$$

For the non-hemisphere contribution, there are now several regions m contributing. The calculation for each region proceeds as in Sec. 4.2.3, except that we now have additional $\theta(p^l - p^m)$ functions in Eq. (4.58), which separate region m from the remaining regions $l \neq i, m$. We can write p^m and p^l in terms of p^i and $x = p^j/p^i$,

$$\begin{aligned}\frac{p^m}{p^i} &= \frac{\hat{s}_{jm}}{\hat{s}_{ij}} + \frac{\hat{s}_{im}}{\hat{s}_{ij}}\,x - 2\Big(\frac{\hat{s}_{jm}\hat{s}_{im}}{\hat{s}^2_{ij}}x\Big)^{1/2}\cos\phi\,,\\ \frac{p^l}{p^i} &= \frac{\hat{s}_{jl}}{\hat{s}_{ij}} + \frac{\hat{s}_{il}}{\hat{s}_{ij}}\,x - 2\Big(\frac{\hat{s}_{jl}\hat{s}_{il}}{\hat{s}^2_{ij}}x\Big)^{1/2}\cos(\phi+\phi_{lm})\,.\end{aligned} \tag{4.60}$$

Here ϕ is again defined as the angle between $\vec{p}_\perp$ and $\vec{\hat{q}}_{m\perp}$, while ϕ_{lm} are the angles between the remaining $\vec{\hat{q}}_{l\perp}$ and $\vec{\hat{q}}_{m\perp}$. The result for $S^{(1)}_{ij,m}(\{k_i\},\mu)$ has the same form as Eq. (4.47),

$$S^{(1)}_{ij,m}(\{k_i\},\mu) \tag{4.61}$$
$$= \frac{\alpha_s(\mu)}{\pi}\bigg\{I_0\Big(\frac{\hat{s}_{jm}}{\hat{s}_{ij}},\frac{\hat{s}_{im}}{\hat{s}_{ij}},\Big\{\frac{\hat{s}_{jl}}{\hat{s}_{jm}},\frac{\hat{s}_{il}}{\hat{s}_{im}},\phi_{lm}\Big\}_{l\neq i,j,m}\Big)\bigg[\frac{1}{\mu}\mathcal{L}_0\Big(\frac{k_i}{\mu}\Big)\,\delta(k_m) - \delta(k_i)\,\frac{1}{\mu}\mathcal{L}_0\Big(\frac{k_m}{\mu}\Big)$$
$$+ \ln\frac{\hat{s}_{jm}}{\hat{s}_{ij}}\,\delta(k_i)\,\delta(k_m)\bigg] + I_1\Big(\frac{\hat{s}_{jm}}{\hat{s}_{ij}},\frac{\hat{s}_{im}}{\hat{s}_{ij}},\Big\{\frac{\hat{s}_{jl}}{\hat{s}_{jm}},\frac{\hat{s}_{il}}{\hat{s}_{im}},\phi_{lm}\Big\}_{l\neq i,j,m}\Big)\,\delta(k_i)\,\delta(k_m)\bigg\}\prod_{l\neq i,m}\delta(k_l)\,.$$

The finite phase-space integrals are now given by

$$
\begin{aligned}
&I_0(\alpha,\beta,\{\alpha_l,\beta_l,\phi_l\}) \\
&\quad= \frac{1}{\pi}\int_{-\pi}^{\pi}\mathrm{d}\phi\int\frac{\mathrm{d}y}{y}\,\theta\big(y-\sqrt{\beta/\alpha}\big)\,\theta\big(1/\alpha-1-y^2+2y\cos\phi\big) \\
&\qquad\times\prod_l\theta\Big[\alpha_l-1+(\beta_l-1)y^2-2y\big[\sqrt{\alpha_l\beta_l}\,\cos(\phi+\phi_l)-\cos\phi\big]\Big]\,, \\
&I_1(\alpha,\beta,\{\alpha_l,\beta_l,\phi_l\}) \\
&\quad= \frac{1}{\pi}\int_{-\pi}^{\pi}\mathrm{d}\phi\int\frac{\mathrm{d}y}{y}\,\ln(1+y^2-2y\cos\phi)\,\theta\big(y-\sqrt{\beta/\alpha}\big)\,\theta\big(1/\alpha-1-y^2+2y\,\cos\phi\big) \\
&\qquad\times\prod_l\theta\Big[\alpha_l-1+(\beta_l-1)y^2-2y\big[\sqrt{\alpha_l\beta_l}\,\cos(\phi+\phi_l)-\cos\phi\big]\Big]\,. \qquad (4.62)
\end{aligned}
$$

An algorithm to systematically evaluate them numerically is given in App. B. The values for the parameters in Eq. (4.61) are $\alpha=\hat{s}_{jm}/\hat{s}_{ij}$, $\beta=\hat{s}_{im}/\hat{s}_{ij}$, $\alpha_l=\hat{s}_{jl}/\hat{s}_{jm}$, and $\beta_l=\hat{s}_{il}/\hat{s}_{im}$.

In the expression for the factorized cross section in Eq. (4.3), the jet and the beam functions do not depend on how many jets there are. Only the hard and the soft function know about the global nature of the event. The necessary QCD calculations for the hard function have been performed for many processes and the last remaining ingredient for a NNLL resummed N-jet cross section has been the soft function. Our NLO calculation of the N-jet soft function enables accurate predictions for jet-mass spectra which can be compared to experimental results. In the next chapter, we shall illustrate the power of this formalism for the case of 1-jettiness.

Chapter 5

Exclusive 1-jet Plus Higgs Production at Hadron Colliders

In this chapter we combine the necessary ingredients to produce NNLL cross sections. We begin with a short theoretical discussion and then proceed to examine the dependence of the 1-jet plus Higgs ($H+1j$) cross section on several variables and parameters. The results in this chapter have not been published previously.

5.1 Cross Section Ingredients

The different ingredients of a NNLL resummed cross section are needed at different levels of perturbative expansion. Our order counting for fixed-order and resummed perturbation theory is summarized in Tab. 5.1. Most of the details necessary to produce NNLL cross sections have been explained in Refs. [17, 40]. We will mention these elements of the calculation only briefly and shall focus on the additional steps we have taken to obtain our results.

	matching (singular)	nonsingular	γ_x	$\Gamma_{\rm cusp}$	β	PDF
LO	LO	LO	-	-	1-loop	LO
NLO	NLO	NLO	-	-	2-loop	NLO
LL	LO	-	-	1-loop	1-loop	LO
NLL	LO	-	1-loop	2-loop	2-loop	LO
NNLL	NLO	-	2-loop	3-loop	3-loop	NLO

Table 5.1: The order counting we use in fixed-order and resummed perturbation theory.

We start from equation Eq. (4.3) and consider the cross section for $H + 1j$ production. This cross section is needed when analyzing the experimental data in Higgs searches. Knowing the theoretical prediction enables the experimentalists to determine what a possible signal above the expected backgrounds signifies. There are two leading-order hard processes that result in the $H + 1j$ final state: $gggH$ and $gq\bar{q}H$. In the first case, there are two initial state gluons, one from each of the protons, and they produce a third gluon and a Higgs. In the second case, there are several possible permutations. The initial state partons can be a combination of a gluon and a quark, a gluon and an antiquark, or a quark and an antiquark. We focus on the $gggH$ channel since it dominates over the $gq\bar{q}H$ channel. The necessary QCD matrix elements for both channels are given at $\mathcal{O}(\alpha_s)$ in Ref. [50].

We can specialize the factorization theorem to the case of 1-jettiness:

$$\begin{aligned}
&\frac{\mathrm{d}\sigma}{\mathrm{d}\mathcal{T}_1^a\,\mathrm{d}\mathcal{T}_1^b\,\mathrm{d}\mathcal{T}_1^J} \\
&\quad= \int \mathrm{d}x_a \mathrm{d}x_b \int \mathrm{d}^4q\,\mathrm{d}\Phi_H(q) \int \mathrm{d}\Phi_1(q_J)\, M_1(\Phi_1,\Phi_H)\,(2\pi)^4\delta^4\big(q_a+q_b-q_J-q\big) \\
&\qquad\times \sum_{i,j} H_{ij}^{H+1j}(\Phi_1,\Phi_H,\mu) \int \mathrm{d}t_a\, B_i(t_a,x_a,\mu) \int \mathrm{d}t_b\, B_j(t_b,x_b,\mu) \int \mathrm{d}s_J\, J_{ij}(s_J,\mu) \\
&\qquad\times S_1^{ij}\left(\mathcal{T}_1^a - \frac{t_a}{Q_a}, \mathcal{T}_1^b - \frac{t_b}{Q_b}, \mathcal{T}_1^J - \frac{s_J}{Q_J}, \{\hat{q}_i\}, \mu\right) ,
\end{aligned} \tag{5.1}$$

where the sum is performed over partons $i, j = \{g, u, \bar{u}, d, \ldots\}$. Since choosing the initial state partons fixes the type of the central jet, we can label the hard, jet, and soft functions with ij. We use the notation Φ_H, Φ_1 to refer to the Higgs and jet phase space, respectively.

We can use the explicit delta-function as well as the azimuthal symmetry to write the cross section as an integral over three degrees of freedom: the parton momentum fractions x_a, x_b and the jet angle with respect to the beam θ. Alternatively, we can use the jet transverse momentum p_T^J, the jet rapidity η^J, and the event rapidity Y. The definition of Y is given in Eq. (3.5).

The cross section is differential in the 1-jettiness contributions from the jet and the beams $\mathcal{T}_1^J$, $\mathcal{T}_1^a$, and $\mathcal{T}_1^b$. For simplicity, we fix $\mathcal{T}_1^a = \mathcal{T}_1^b$ and write $\mathcal{T}_1^B = \mathcal{T}_1^a + \mathcal{T}_1^b$. To include as much of the experimental data as possible, we usually integrate both $\mathcal{T}_1^{a,b}$ up to

$\mathcal{T}_1^{B,\mathrm{cut}}/2$. In that case we use the notation

$$\frac{\mathrm{d}\sigma(\mathcal{T}_1^{B,\mathrm{cut}})}{\mathrm{d}\mathcal{T}_1^J} = \int_0^{\mathcal{T}_1^{B,\mathrm{cut}}/2} \mathrm{d}\mathcal{T}_1^a \int_0^{\mathcal{T}_1^{B,\mathrm{cut}}/2} \mathrm{d}\mathcal{T}_1^b \frac{\mathrm{d}\sigma}{\mathrm{d}\mathcal{T}_1^a\,\mathrm{d}\mathcal{T}_1^b\,\mathrm{d}\mathcal{T}_1^J}. \tag{5.2}$$

In order for the factorization theorem to hold, we must restrict ourselves to a certain kinematic region. We require that $\mathcal{T}_1^i \sim \mathcal{T}_1^j$ so that there are no large logarithms inside the soft function, $\hat{q}_i \cdot \hat{q}_j \gg \mathcal{T}_1^i/Q_i$ so that jets are well separated, and $Q_i \sim Q_j$ so that we can have one consistent hard scale.

After performing the phase space integrals mentioned above, we get the expression

$$\begin{aligned}
&\frac{\mathrm{d}\sigma}{\mathrm{d}\mathcal{T}_1^a\,\mathrm{d}\mathcal{T}_1^b\,\mathrm{d}\mathcal{T}_1^J} \\
&\quad= \int \mathrm{d}x_a \mathrm{d}x_b \int \mathrm{d}\cos\theta \frac{1}{16\pi} \frac{2|\vec{p}|}{\sqrt{x_a x_b} E_{\mathrm{cm}}} \\
&\qquad\times \sum_{i,j} H_{ij}^{H+1j}(x_a, x_b, \cos\theta, \mu) \int \mathrm{d}t_a\, B_i(t_a, x_a, \mu) \int \mathrm{d}t_b\, B_j(t_b, x_b, \mu) \int \mathrm{d}s_J\, J_{ij}(s_J, \mu) \\
&\qquad\times S_1^{ij}\left(\mathcal{T}_1^a - \frac{t_a}{Q_a}, \mathcal{T}_1^b - \frac{t_b}{Q_b}, \mathcal{T}_1^J - \frac{s_J}{Q_J}, \{\hat{q}_i\}, \mu\right),
\end{aligned} \tag{5.3}$$

where $\vec{p}$ is the jet momentum and E_{cm} is the center-of-mass energy of the collider. The value of $\vec{p}$ is fully specified by the independent kinematic variables. For most plots we choose one phase space point by fixing (x_a, x_b, θ) or alternatively (p_T^J, η^J, Y). Unless otherwise specified, the plots of the cross section are given for $Y = 0$ since this region is where most of the cross section lies. The expression for the cross section at a single kinematic point is

$$\begin{aligned}
&\frac{\mathrm{d}\sigma}{\mathrm{d}\mathcal{T}_1^a\,\mathrm{d}\mathcal{T}_1^b\,\mathrm{d}\mathcal{T}_1^J\,\mathrm{d}x_a\,\mathrm{d}x_b\,\mathrm{d}\cos\theta} \\
&\quad= \sum_{i,j} H_{ij}^{H+1j}(x_a, x_b, \cos\theta, \mu) \int \mathrm{d}t_a\, B_i(t_a, x_a, \mu) \int \mathrm{d}t_b\, B_j(t_b, x_b, \mu) \int \mathrm{d}s_J\, J_{ij}(s_J, \mu) \\
&\qquad\times S_1^{ij}\left(\mathcal{T}_1^a - \frac{t_a}{Q_a}, \mathcal{T}_1^b - \frac{t_b}{Q_b}, \mathcal{T}_1^J - \frac{s_J}{Q_J}, \{\hat{q}_i\}, \mu\right) A(x_a, x_b, \cos\theta),
\end{aligned} \tag{5.4}$$

where the kinematic factor is given by $A(x_a, x_b, \cos\theta) = \frac{1}{16\pi}\frac{2|\vec{p}|}{\sqrt{x_a x_b} E_{\mathrm{cm}}}$. If we consider a single phase space point and normalize the cross section by the cumulant, A cancels out.

Much of the power of SCET comes from being able to evaluate the different fixed-order pieces at their natural scales, which we call μ_H, μ_B, μ_J, and μ_S for the hard, beam, jet, and soft scales, respectively. Since we take $\mathcal{T}_1^a = \mathcal{T}_1^b$, we have only one beam scale. We write the

fixed order components using the evolution kernels which implement the renormalization group evolution between the various natural scales and the common scale μ. We follow the notation of Ref. [17] for the kernels. Since the soft and the hard functions for 1-jet production are scalars in the color space, each of them has a scalar-valued evolution kernel. An alternate notation $t_{a,b} \equiv s_{a,b}$ simplifies some of the expressions. Then the cross section is given by

$$\begin{aligned}
&\frac{\mathrm{d}\sigma}{\mathrm{d}\mathcal{T}_1^a\,\mathrm{d}\mathcal{T}_1^b\,\mathrm{d}\mathcal{T}_1^J\,\mathrm{d}x_a\,\mathrm{d}x_b\,\mathrm{d}\cos\theta} \\
&\quad= \sum_{i,j} U_{ij}^H(x_a, x_b, \cos\theta, \mu_H, \mu)\, H_{ij}^{H+1j}(x_a, x_b, \cos\theta, \mu_H)\, A(x_a, x_b, \cos\theta) \\
&\qquad\times \int \mathrm{d}s_a \int \mathrm{d}s_a'\, U_i^B(s_a', \mu_B, \mu) B_i(s_a - s_a', x_a, \mu_B) \\
&\qquad\times \int \mathrm{d}s_b \int \mathrm{d}s_b'\, U_j^B(s_b', \mu_B, \mu) B_j(s_b - s_b', x_b, \mu_B) \\
&\qquad\times \int \mathrm{d}s_j \int \mathrm{d}s_j'\, U_{ij}^J(s_j', \mu_J, \mu) J_{ij}(s_j - s_j', \mu_J) \\
&\qquad\times \int \mathrm{d}s_a'' \int \mathrm{d}s_b'' \int \mathrm{d}s_J''\, U_{ij}(\{Q_i\mathcal{T}_N^i - s_i - s_i''\}, x_a, x_b, \cos\theta, \mu_S, \mu) S_1^{ij}\left(\left\{\frac{s_i''}{Q_i}\right\}, \{\hat{q}_i\}, \mu\right).
\end{aligned} \tag{5.5}$$

For NNLL resummation, all the fixed order pieces of the calculation—hard, beam, jet, and soft functions—are needed at $\mathcal{O}(\alpha_s)$. However, it is not a priori clear whether or not one should expand them as a series in α_s so that after the convolutions the fixed-order cross section only has terms up to $\mathcal{O}(\alpha_s)$. The effect of different ways of expanding the cross section on the normalized differential cross section is very small. We choose to expand the beam, jet, and soft functions but keep the one-loop hard function unexpanded and multiply the rest of the fixed-order expression by it.

Eq. (5.5) gives accurate results when $\mathcal{T}_1^i \approx \mathcal{T}_1^j$. However, in order to match what the experimentalists do as closely as possible, we want to plot the differential cross section as a function of $\mathcal{T}_1^J$ while keeping $\mathcal{T}_1^{B,\mathrm{cut}}$ constant. This will induce unphysical nonglobal logarithms $\ln(\mathcal{T}_1^J/\mathcal{T}_1^{B,\mathrm{cut}})$ in the soft function unless we introduce two soft scales. In order to justify this approach, we first note that the evolution of the soft function factorizes as follows

$$S_1\left(\mathcal{T}_1^J, \mathcal{T}_1^{B,\mathrm{cut}}, \mu\right) = U_{S_B}(\mu, \mu_0) U_{S_J}(\mu, \mu_0) \otimes S_1\left(\mathcal{T}_1^J, \mathcal{T}_1^{B,\mathrm{cut}}, \mu_0\right), \tag{5.6}$$

where the notation implies convolution between the evolution kernels and the soft function.

At NLO, we can also factorize the soft function as

$$S_1\left(\mathcal{T}_1^J, \mathcal{T}_1^{B,\mathrm{cut}}, \mu_0\right) = S_1^J\left(\mathcal{T}_1^J, \mu_0\right) S_1^B\left(\mathcal{T}_1^{B,\mathrm{cut}}, \mu_0\right) . \tag{5.7}$$

At the order we are working, there will not be even $\mathcal{O}(1)$ nonglobal logarithms resulting from this factorization. To implement the NNLL cross section with two soft scales, we write

$$S_1\left(\mathcal{T}_1^J, \mathcal{T}_1^{B,\mathrm{cut}}, \mu', \mu\right) = \left[U_{S_J}(\mu', \mu_{S_J}) \otimes S_1^J\left(\mathcal{T}_1^J, \mu_{S_J}\right)\right]\left[U_{S_B}(\mu, \mu_{S_B}) \otimes S_1^B\left(\mathcal{T}_1^{B,\mathrm{cut}}, \mu_{S_B}\right)\right] . \tag{5.8}$$

We can then minimize all the logarithms by choosing $\mu_{S_B} \sim \mathcal{T}_1^{B,\mathrm{cut}}$, $\mu_{S_J} \sim \mathcal{T}_1^J$. More precisely, we use the same profile functions as Ref. [17] except that in their Eq. (2.54), we replace m_H by the final-state center-of-mass energy Q and instead of τ we use the appropriate $\mathcal{T}_1^i/Q$. We also set $\mu_H = -iQ$ in order to resum the π^2-terms coming from logarithms with a negative argument. For our jet scale, we use the same profile function as for the beam scale but with the value $\tau_J = \mathcal{T}_1^J/Q$. For both of the soft scales, we use their soft scale profile function with μ_{S_J} determined from $\mathcal{T}_1^J/Q$ and μ_{S_B} from $\mathcal{T}_1^{B,\mathrm{cut}}/Q$. In order to satisfy $\mathcal{T}_1^J \sim \mathcal{T}_1^{a,\mathrm{cut}}, \mathcal{T}_1^{b,\mathrm{cut}}$ in the peak region, we choose $\mathcal{T}_1^{a,\mathrm{cut}} = \mathcal{T}_1^{b,\mathrm{cut}} = \mathcal{T}_1^{B,\mathrm{cut}}/2 = 5\,\mathrm{GeV}$ for all of the plots unless we are explicitly varying $\mathcal{T}_1^{B,\mathrm{cut}}$.

There is some ambiguity in how to split the soft function into the jet and beam components. We assign the $\mathcal{L}_n(k_i)$-terms from Eqs. (4.43) and (4.47) into the component indicated by the index i. This way, the term $\mathcal{L}_n(k_J)$ belongs to the jet component of the soft function etc. The terms which only contain delta functions are split evenly such that beam a, beam b, and the jet component include one third each. If we had only one soft scale, there would be no ambiguity and hence its effect can be quantified by introducing some correlation between the two soft scales. This is discussed in more detail above Eq. (5.10) and Fig. 5-2(d) shows that the effect is small.

The running for the different soft function components is obtained by noting that the soft running must exactly compensate for the hard, beam, and jet running. Hence, the soft evolution kernel is a combination of the inverse of those evolution kernels. Both of the beam evolution kernels contribute to the running of the beam component of the soft function and the jet evolution kernel contributes to the running of the jet component. The hard function anomalous dimension consist of dipole terms and we split each dipole in half

between the two directions it connects. Hence a dipole connecting the jet and beam a contributes equally to the running of the jet and beam components of the soft function. With the soft evolution split into the beam and jet components, we can run both of them from their respective scales $\mu_{B,J}$ to the common scale μ.

We calculate the differential jet mass spectrum by finding the cumulant of the cross section in $\mathcal{T}_1^J$ and then taking the numerical derivative. We give the cross section as a function of $m_J = \sqrt{\mathcal{T}_1^J Q_J}$ and include the necessary Jacobian factor coming from the change of variables. Unless otherwise specified, all the cross section plots use NNLL accuracy. We use MSTW NLO PDFs [46] to evaluate our beam functions and fix the values $m_Z = 91.1876\,\text{GeV}$ for the Z-mass and $\alpha_s(m_Z) = 0.12018$ for the strong coupling constant at the Z-mass. For Higgs mass we choose $m_H = 125\,\text{GeV}$. All of our plots are for the LHC so we use proton PDFs and 7 TeV for the center-of-mass energy.

5.2 Results

5.2.1 Jet Radius

In Chap. 3 we explored the shape of the jet produced by different choice for the normalization factors Q_i. Out of the three choices presented, the geometric (E) definition is most similar to jet algorithms used by experimentalists. However, we can go even further and define a geometric $R = 1$ jet by taking the geometric (E) definition and changing the jet weight factor from $Q_J = E_J$ to $Q_J(R, \eta) = \rho(R, \eta)E_J$. We define the matching parameter ρ such that the $R = 1$ geometric jet always has the same area in (η, ϕ)-plane as an $R = 1$ anti-k_t jet. The comparison between geometric $R = 1$ jets and anti-k_t jets is shown in Fig. 5-1. Figs. 5-1(a) and 5-1(b) illustrate the matching of the jet areas. We can match an anti-k_t jet (orange, background) that has $\eta^J = -1.0$ quite well with the 1-jettiness jet (blue, foreground). A perfectly central 1-jettiness jet does not have a circular shape but we have matched the areas by choosing an appropriate value for ρ.

From Figs. 5-1(c) and 5-1(d) we can see how the matching parameter behaves as a function of its two arguments. We have calculated the ρ that matches $R = 1$ anti-k_t jets for several values of η^J. We then fit the values to a curve which gives $\rho(\eta^J)$ for arbitrary η^J. The further out towards the beams a jet lies, the less there is a need to change its size. The matching parameter ρ scales as R^2 when we vary the radius R of the anti-k_t jet.

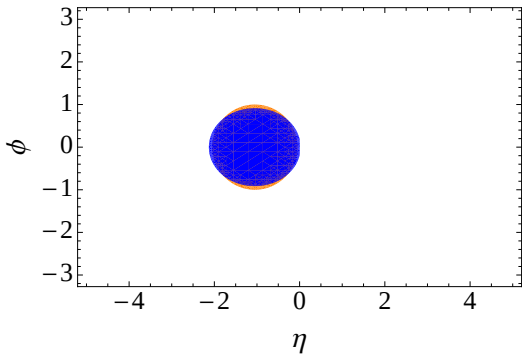

(a) An anti-k_t jet with $\eta_J = -1.0$ (orange, background) is closely matched by a 1-jettiness jet (blue,foreground).

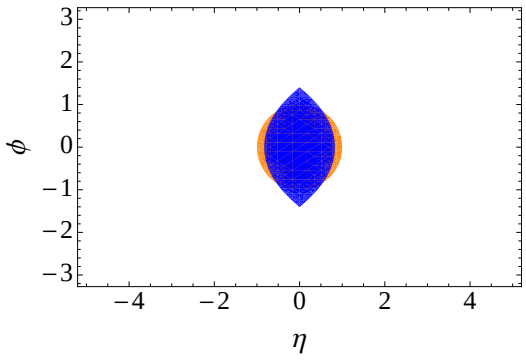

(b) A central 1-jettiness jet (blue,foreground) has a different shape than an anti-k_t jet (orange, background) but is matched to have the same area.

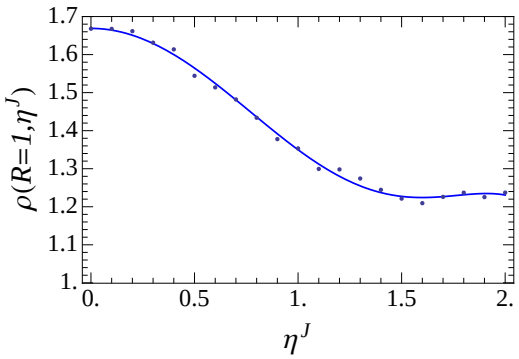

(c) Increasing the jet rapidity requires decreasing ρ in order to keep the jet area constant.

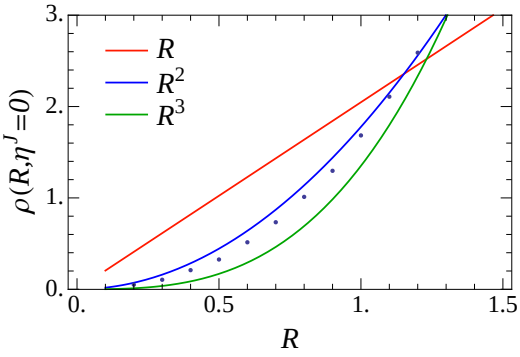

(d) The matching parameter ρ is proportional to R^2.

Figure 5-1: The areas of 1-jettiness and anti-k_t jets can be matched by introducing a variable normalization parameter $Q_J(R,\eta) = \rho(R,\eta)E_J$.

Except when otherwise noted, all the plots feature a jet with $\eta^J = 0$ which is matched to $R = 1$ by setting $\rho = 1.67$. Whenever other values for jet rapidity η^J are considered, we use the fit shown in Fig. 5-1(c) to find the right value for ρ.

5.2.2 Normalization Procedure

It is standard practice for the experimental collaborations to report their data as normalized cross sections since normalization reduces the uncertainty coming from both experimental and theoretical factors. We will follow their example for many of our plots and so it is appropriate to start by discussing the details of the normalization procedure.

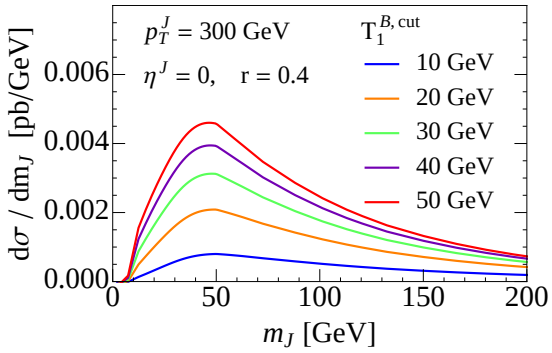

(a) Increasing $\mathcal{T}_1^{B,\text{cut}}$ increases the unnormalized cross section.

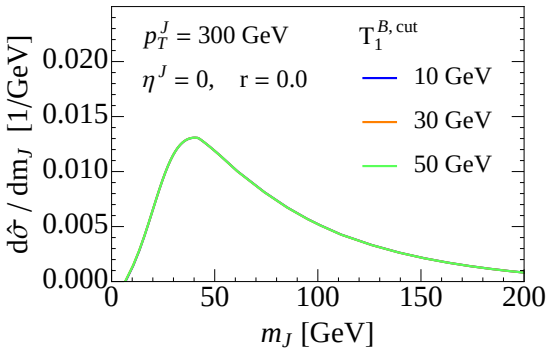

(b) Normalization removes virtually all $\mathcal{T}_1^{B,\text{cut}}$ dependence.

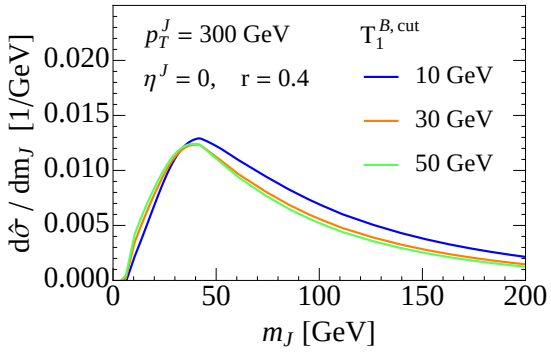

(c) Correlating soft scales reintroduces some $\mathcal{T}_1^{B,\text{cut}}$ dependence.

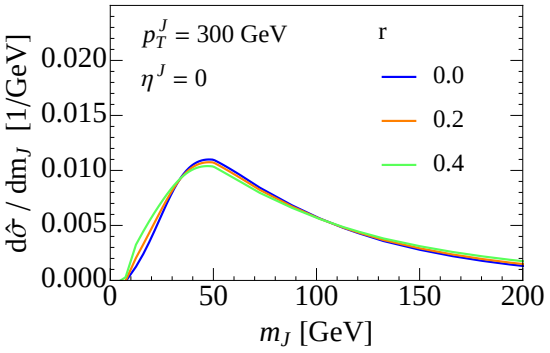

(d) Different values of the correlation parameter r have only a small effect.

Figure 5-2: Normalization removes the effect of $\mathcal{T}_1^{B,\text{cut}}$.

We define the normalized differential cross section as follows:

$$\frac{\mathrm{d}\hat{\sigma}}{\mathrm{d}m_J}(m_J, \mathcal{T}_1^{B,\text{cut}}, p_T^J, \eta^J, Y, m_J^{\text{cut}}) \equiv \frac{\mathrm{d}\sigma(m_J, \mathcal{T}_1^{B,\text{cut}}, p_T^J, \eta^J, Y)/\mathrm{d}m_J}{\int_0^{m_J^{\text{cut}}} \mathrm{d}m \left[\mathrm{d}\sigma(m, \mathcal{T}_1^{B,\text{cut}}, p_T^J, \eta^J, Y)/\mathrm{d}m\right]}, \tag{5.9}$$

where the normalization is determined by evaluating the cumulant at the value m_J^{cut}, which we choose as the end of the x-axis of the plot (200 GeV or 300 GeV). As a technical detail, it should be noted that we perform the integrals to obtain the cumulant analytically and determine the jet and soft scales μ_J, μ_{S_J} from m_J^{cut}.

The units of the normalized differential cross section $\mathrm{d}\hat{\sigma}/\mathrm{d}m_J$ are GeV^{-1}. For the unnormalized cross section $\mathrm{d}\sigma/\mathrm{d}m_J$ we give the plots in units of pb / GeV. All the unnormalized cross section plots are for a single phase space point and the units are per unit range of x_a, x_b, and $\cos\theta$. To get an expression which can be compared to experiment, the

cross section needs to be integrated against a range of these variables.

Fig. 5-2(a) shows how increasing $\mathcal{T}_1^{B,\text{cut}}$ increases the unnormalized cross section. This is as expected since we are allowing more events by integrating the cross section to higher values of $\mathcal{T}_1^{B,\text{cut}}$. In Fig. 5-2(b), we can see that the normalization removes virtually all $\mathcal{T}_1^{B,\text{cut}}$ dependence. This $\mathcal{T}_1^{B,\text{cut}}$ independence is connected to the separation of the two soft scales, μ_{S_J} and μ_{S_B}. In order to model any uncertainty coming from this factorization, we introduce a correlation parameter r ($0 \leq r \leq 1$) and define the soft scales as (with the dependence on $\mathcal{T}_1^{B,J}$ suppressed for clarity)

$$\begin{aligned} \mu_{S_J}(r) &= \bar{\mu}^r \mu_{S_J}(0)^{1-r} \,, \\ \mu_{S_B}(r) &= \bar{\mu}^r \mu_{S_B}(0)^{1-r} \,, \\ \bar{\mu} &= \mu_{S_J}(0)^{1/3} \mu_{S_B}(0)^{2/3} \,, \end{aligned} \tag{5.10}$$

where the average soft scale $\bar{\mu}$ is the single scale that minimizes the logarithms in the soft function if we do not use multiple soft scales. By setting $r = 0$ we recover the original separate soft scales. Increasing r moves the scales together towards the average value. Fig. 5-2(c) illustrates the effect of changing $\mathcal{T}_1^{B,\text{cut}}$ when we use $r = 0.4$. We see that while the curves do not overlap perfectly anymore, the overall shape and the peak position is quite stable. In Fig. 5-2(d), we compare the effects of different values of r and note that they are small.

Both experimental and theoretical uncertainties usually affect the normalization of a cross section much more than they effect the shape. Comparing normalized cross sections eliminates much of this uncertainty. We estimate the uncertainty due to higher order corrections by varying the various scales in our calculation and use a generalization of the variations in Ref. [17]. In addition to their hard, beam, and soft scale variation, we have a second soft scale and a jet scale that we also vary. Both soft variations use the same profile function but with two different arguments $\tau_{S_{J,B}}$. We combine the uncertainties from the two soft scale variations by varying both of them up and down simultaneously. The hard, jet, and beam scales are varied independently. To account for the fact that we have several comparable variations, we combine the different uncertainties in quadrature.

Figs. 5-3(a) and 5-3(b) illustrate the reduction in uncertainty achieved by the normalization procedure. In Fig. 5-3(c) we can see that several of the scale variations give comparable

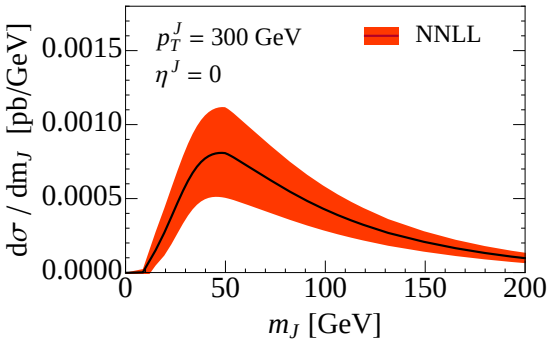

(a) The NNLL uncertainty in the unnormalized cross section is quite large.

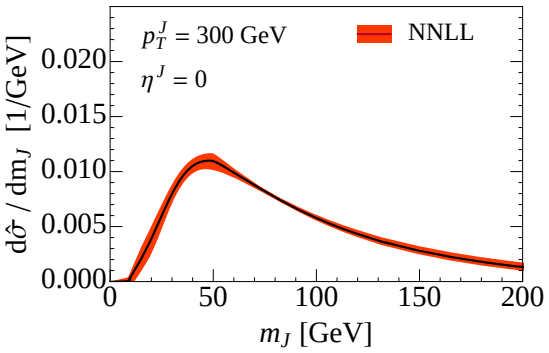

(b) Normalization reduces the uncertainty.

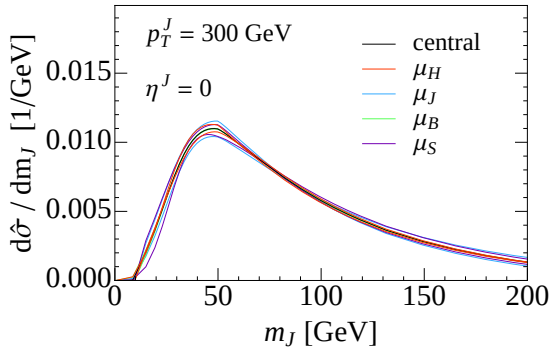

(c) Several of the scale variations have a comparable size.

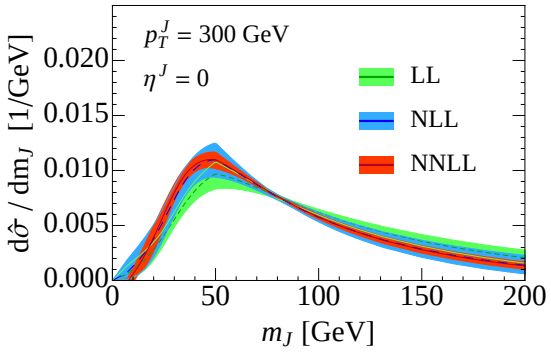

(d) The NNLL uncertainty is significantly smaller than the NLL uncertainty.

Figure 5-3: Normalization reduces the theoretical uncertainty significantly.

contributions. Finally, Fig. 5-3(d) demonstrates how the NNLL result has a much narrower uncertainty band than the NLL calculation.

We note also that the normalization procedure perfectly cancels the dependence on the hard function if we are only interested in a single phase space point. The cancellation of the hard function still takes place approximately for the integrated cross section, since the dominant contribution comes from a small volume of the phase space. Therefore, our results are expected to be representative of general jet production.

5.2.3 Kinematics

The precision of modern collider detectors such as ATLAS and CMS allows the experimentalists to extract a lot of information about the final state of a collision. For jets, the two most commonly reported quantities are the jet rapidity η^J and transverse momentum p_T^J. In this section we will explore how these variables as well as the system rapidity Y influence

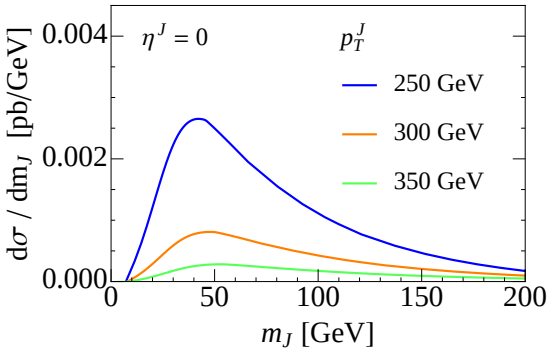

(a) There are more jets at low p_T than at high p_T.

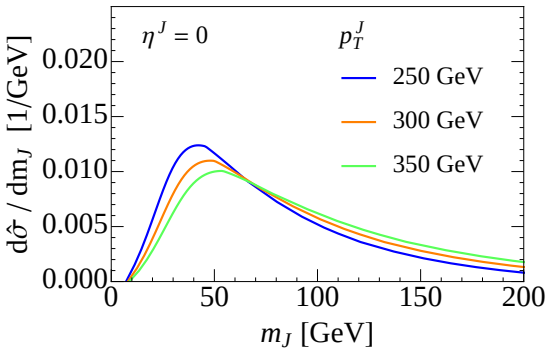

(b) Increasing p_T^J moves the peak position to higher mass.

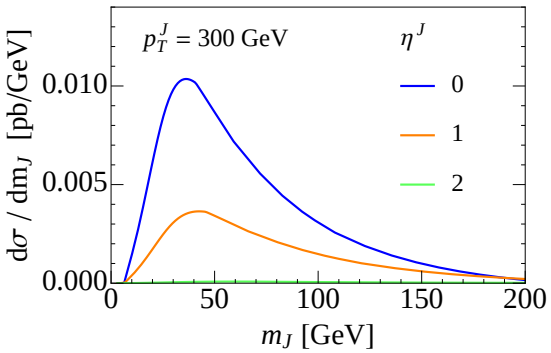

(c) There are more central jets than forward jets.

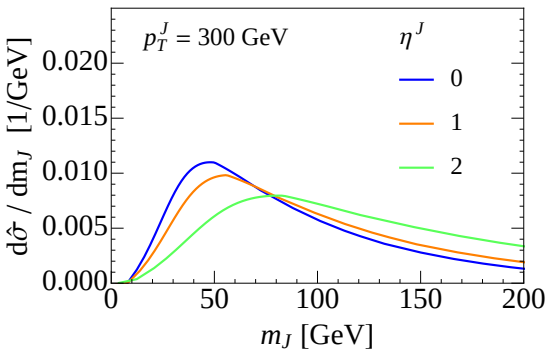

(d) Increasing η^J moves the peak position to higher mass.

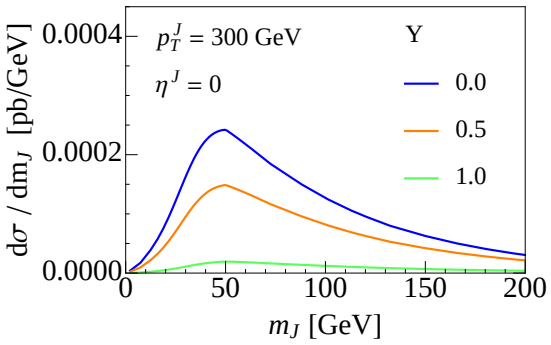

(e) Most of the cross section is at low system rapidities due to parton luminosity.

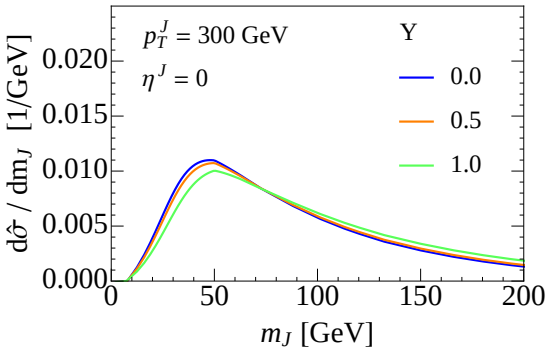

(f) Y has only a small effect on the peak position.

Figure 5-4: Changing kinematic variables (p_T^J, η^J, Y) changes both the normalization and the shape of the cross section.

the normalization and the shape of the cross section.

Since the parton luminosity is largest for small values of $x_{a,b}$, the most likely processes are those with the lowest partonic center-of-mass energy Q. Higher-p_T jets require higher Q and are produced more seldom, as shown in Fig. 5-4(a). Increasing p_T^J also moves the peak of the cross section to higher mass (Fig. 5-4(b)).

Varying the jet rapidity has a large effect both on the normalization and the shape of the cross section. Figs. 5-4(c) and 5-4(d) show how central jets are much more numerous than forward jets, and how higher η^J moves the peak of the cross section to higher mass.

As mentioned earlier, most of our plots use $Y = 0$ and Fig. 5-4(e) justifies this choice since this is where the cross section is the highest. At least one of $x_{a,b}$ has to be large to give large $|Y|$ so the PDFs will suppress the cross section at these values. The system rapidity has a smaller effect on the peak position than p_T^J or η^J, as can be seen in Fig. 5-4(f).

5.2.4 Jet Definition

In Chap. 3 we discussed the different choices for the normalization factors Q_i and how they affect the shape of the jet and beam regions. Here we will see how such changes in jet and beam regions influence the cross section. We look at three different kinematic configurations by fixing $p_T^J = 300\,\text{GeV}$ and choosing $\eta^J = \{0.0, 1.0, 2.0\}$. In the left column of Fig. 5-5 we compare the invariant mass, geometric (p_T), and geometric (E) measures. The two geometric measures agree exactly for $\eta^J = 0.0$ and differ progressively more as the jet becomes more forward. The peak position is lowest for geometric (p_T) and highest for invariant mass measure with geometric (E) lying in between. The right column of Fig. 5-5 shows that the cross section is only moderately affected by varying the matching parameter ρ defined in Sec. 5.2.1. A higher value of ρ gives a higher peak position.

5.2.5 Comparison to ATLAS Data

Having studied the effect of various kinematic variables and other parameters on the differential cross section, let us compare our calculation to experimental data from the ATLAS collaboration measuring the jet-mass spectrum. The CMS collaboration has not yet published a jet-mass spectrum analysis. A few words of explanation are in order about the differences between our calculation and their measurement. The ATLAS data is based on an inclusive jet sample which contains all jets lying in the range $|\eta^J| < 2.0$ and in the

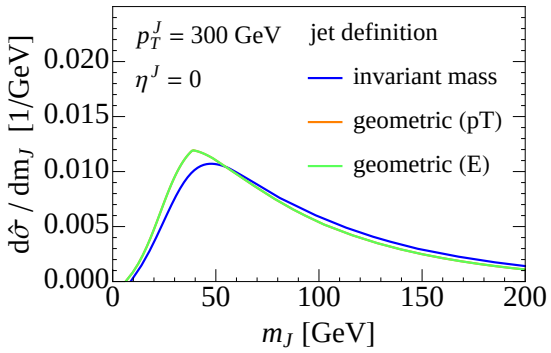

(a) Geometric (p_T) and (E) measures are identical when $\eta^J = 0$. The invariant mass measure has a peak further to the right.

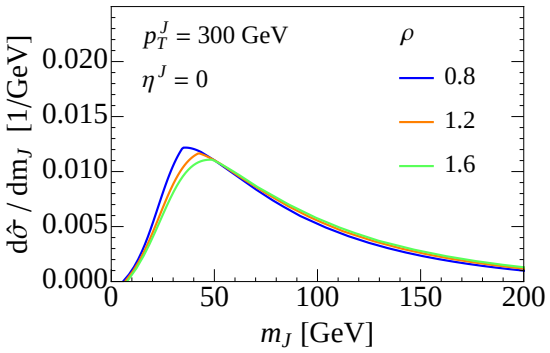

(b) Higher values of ρ make the geometric measure resemble the invariant mass measure more closely.

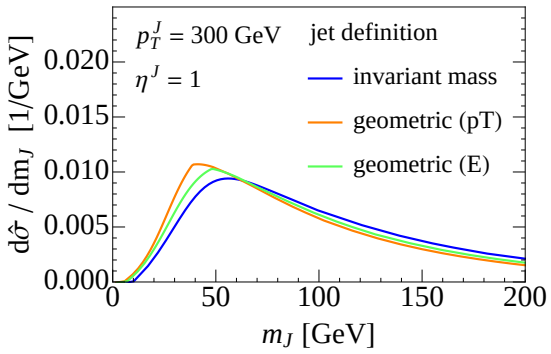

(c) The difference between geometric (p_T) and (E) measures becomes visible when $\eta^J \neq 0$.

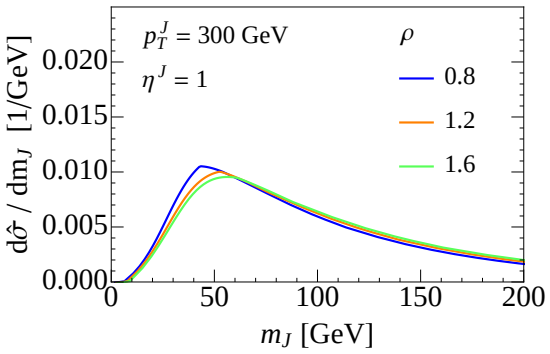

(d) Varying ρ changes the peak position only slightly.

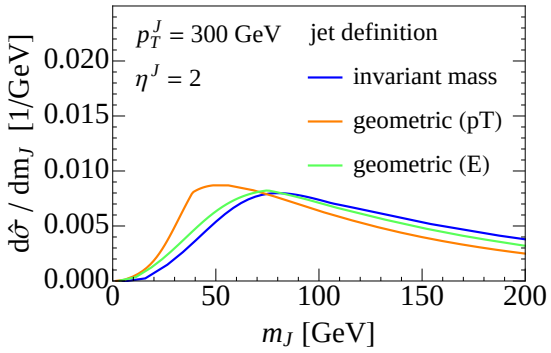

(e) The geometric (p_T) measure has the most stable peak position as a function of η^J.

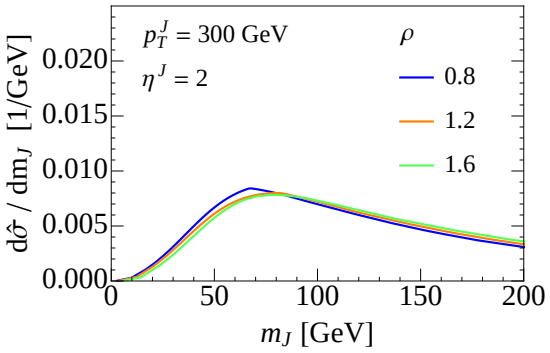

(f) For high η^J, the effect of ρ gets smaller.

Figure 5-5: Changing the jet definition changes the shape of the cross section.

given p_T-bin. This dataset is dominated by dijets which are copiously produced by QCD interactions at the LHC. Our calculation studies the production of the Higgs boson and one exclusive jet. As mentioned, normalizing $\mathrm{d}\sigma/\mathrm{d}m_J$ causes the hard function to drop out exactly for a single phase space point and approximately when integrated over phase space. To the extent that the normalized result is independent of the hard process, we can compare our calculation to the ATLAS data.

There are two main differences between the data and our calculation that do not cancel. First, our calculation includes only the $gggH$ channel which produces gluon jets, whereas the ATLAS data is comprised of a mixture of gluon and quark jets. Second, both of the major dijet channels $gg \to gg$ and $gg \to q\bar{q}$ have color flow that is different from our calculation.

In Figs. 5-6(a) and 5-6(b) we compare a single phase space point to the experimental data. The ATLAS data is denoted by black squares with the black error bars showing the combined statistical and systematic uncertainty. The theoretical NNLL calculation is given by the solid black line and the blue shaded region around it represents the uncertainty obtained from scale variation. We note that the peak positions match for both values of p_T^J but the tail is too high in our calculation. One possible explanation is that we include only the singular contribution to the cross section and the nonsingular pieces become relevant for higher values of m_J. If the nonsingular terms bring the tail down, the normalization procedure increases the peak height, making the agreement better in both regions.

Most of our plots show only a single kinematic point since the phase space integration is computationally demanding. For the final comparison to data, we performed the phase space integrations to match the ATLAS jet selection criteria precisely. Numerical integration is needed for all three kinematic variables (p_T^J, η^J, Y). The phase space integrated cross section is shown in red in Figs. 5-6(c) and 5-6(d) with the ATLAS data shown as before. We see that the effect of including the full phase space is small. The theoretical uncertainties for Figs. 5-6(c) and 5-6(d) will be similar to those in Figs. 5-6(a) and 5-6(b).

The agreement between our calculation and the data suggests that including some quark jets and changing the color flow are minor effects and that the shape of the jet mass spectrum is dominated by the evolution of gluon jets that takes place after the hard process.

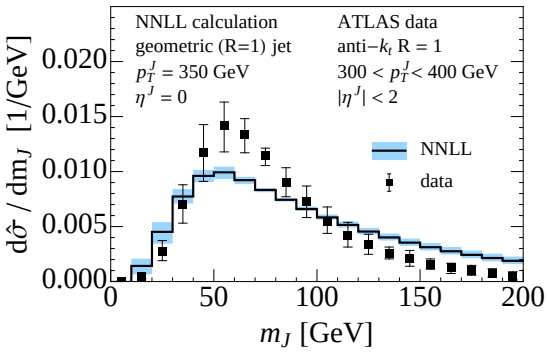

(a) The peak location is well reproduced by our calculation with $p_T^J = 350\,\text{GeV}$.

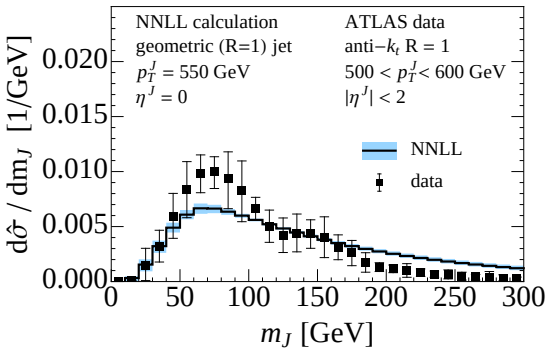

(b) The dependence of the peak location on p_T^J is similar for the data and our calculation.

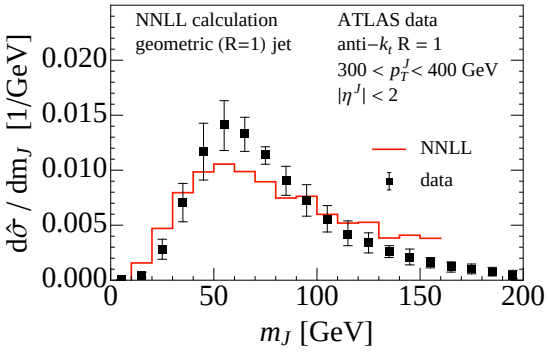

(c) Phase space integration does not change the result very much.

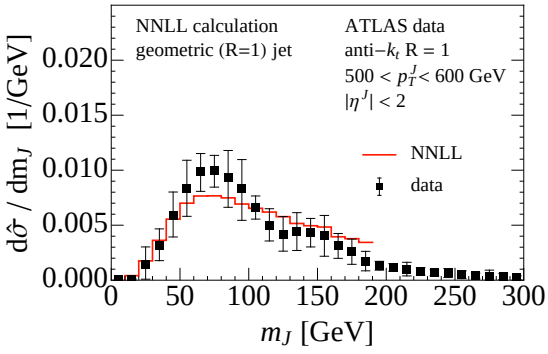

(d) Data and our calculation agree also for $500\,\text{GeV} < p_T^J < 600\,\text{GeV}$.

Figure 5-6: Our NNLL calculation for $H + 1j$ production has similar peak position as the inclusive jet sample from ATLAS which contains all jets lying in the range $|\eta^J| < 2.0$ and in the given p_T-bin

When ATLAS and CMS collaborations release jet data binned in jet rapidity η^J, it will be interesting to compare our prediction with their results. Our calculation can also be used to understand the jet-binning uncertainties in Higgs analyses.

Chapter 6

Conclusions

The recent data from the LHC has started a new era in particle physics. The search for physics beyond the Standard Model is in full swing and our understanding of the Standard Model itself continues to improve. In this thesis we have studied the production of hadronic jets and focused especially on hadron colliders. In order to better predict exclusive N-jet cross sections, we have studied a global event shape called N-jettiness. We have given a factorization theorem for the cross section fully differential in the individual N-jettiness contributions for each region, $\mathcal{T}_N^i$, which is closely connected to the mass of each jet region. We have computed the corresponding N-jettiness soft function, differential in all $\mathcal{T}_N^i$ at one loop.

In our calculation we analytically extract the UV divergences by splitting the phase space into hemispheres depending on which Wilson lines the soft gluon attaches to. The hemisphere contributions reproduce the anomalous dimension of the soft function as expected from the consistency of the factorization theorem. The remaining non-hemisphere contributions, which encode the dependence on the boundaries between the regions, are reduced to one-dimensional numerical integrals. We show that this hemisphere decomposition can be applied in general to compute soft functions for other observables, such as traditional jet algorithms and jet shapes, at one loop. We also expect that it can be generalized to two loops.

Our soft-function calculation provided the last missing ingredient to obtain the exclusive N-jet cross section resummed to NNLL for any process where the corresponding SCET hard function at NLO is known from the one-loop QCD calculation. We chose the process

$gg \to Hg$ to study the mass spectrum of an exclusive jet with 1-jettiness. The shape of the jet region as determined by 1-jettiness depends on the specific distance measure used, and our results apply to any choice of distance measure. Using a geometric measure, the jet regions yield jets with circular boundaries, which is a feature desired experimentally. We further matched the distance measure to produce geometric jets that have the same area as $R = 1$ anti-k_t jets.

A two-particle final state provides much more freedom compared to producing only the Higgs boson, and we have explored the effect of different kinematic configurations on the jet mass spectrum. We have compared our calculations to recent data from the ATLAS collaboration and noted that although their data contains mainly dijet events, the jet mass spectrum matches our calculation quite well. It is likely that the spectrum is approximately independent of the production mechanism of the jet and depends mostly on the jet transverse momentum and rapidity.

Our results can be used to improve Monte Carlo predictions for LHC data. One possibility is to take an existing event generator and reweight the events to match our jet mass spectrum. The validity of our approach can be tested by comparing our predictions for the dependence of the jet mass spectrum on the jet rapidity to future data from the LHC collaborations.

Appendix A

Zero-bin with a Jet Algorithm

The purpose of the zero-bin subtraction is to remove double counting between the jet and soft functions. As explained in Ref. [44], there is some freedom in how to define the subtraction. This can be compared to freedom in choosing between different renormalization schemes, all of which remove the UV divergences but can differ by finite constants. Similarly, all zero-bin subtraction schemes must remove the IR divergences in a universal manner but may include different constants in the result. The authors of Ref. [44] advocate for a minimal approach analogous to minimal subtraction for renormalization. We show how their approach can be extended in a consistent way to apply also in the presence of phase space restrictions, such as jet algorithms. We expect there to be other consistent zero-bin subtraction schemes but we leave their exploration to future work.

When dealing with phase space, it is convenient to think about the zero-bin scaling in terms of final state momenta instead of loop momenta. The two approaches are equivalent but the former is conceptually simpler to apply to jet algorithms. To begin with, we write down the Feynman diagrams for the desired process where an initial parton goes into a final state of several particles. The momenta of all the external particles and all the internal propagators are considered independent and momentum conservation at the vertices is implemented by explicit delta functions and integrals over the internal momenta. At any order in α_s, the zero-bin contributions for a Feynman diagram are found by taking one or more of the collinear final state momenta p_i to scale as $p_i \sim Q\lambda^2$. This only affects expressions where two different momenta are added or subtracted. In the approach advocated here such comparisons only take place at the vertices. Performing the integrals

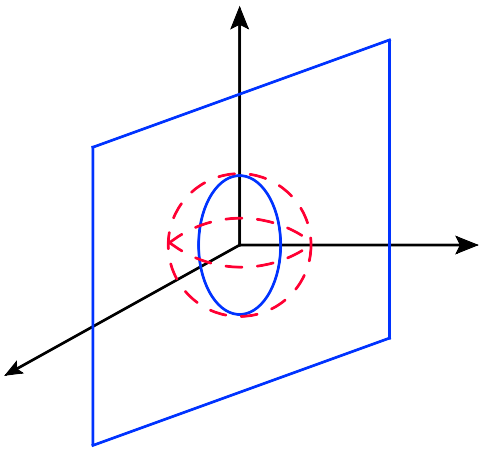

Figure A-1: Schematic representation of the phase space. The blue parallelogram represents the hypersurface defined by phase space constraints, the red dashed sphere represents the zero-bin region, and the blue oval shows the intersection of the hypersurface with the zero-bin region.

over the internal momenta conveys the information about the zero-bin scaling contained in the vertices into the rest of the diagram. The same approach can also be taken when thinking about the zero-bin scaling in loop diagrams that give the cross section via the optical theorem. As long as the momentum for every propagator is considered independent, it is possible to apply the zero-bin scaling to a single propagator and let the momentum-conserving delta functions convey the information about the scaling to the rest of the propagators. Hence, thinking about the zero-bin this way unifies the treatment of phase space integrals and loop integrals.

In order to discuss the influence of phase space restrictions, let us consider a cross section that is fully differential in N variables, i.e. no integrals over physical degrees of freedom have been performed. In this case, no zero-bin subtraction is needed since we have full control over the momenta of all particles; we can tell which region of phase space they are in and hence whether they are soft or collinear. Next, let us perform some integrals that can cause the integrand to be evaluated in the zero-bin region while keeping the cross section differential in M variables b_k. (For example, think of b_k as the invariant masses of the jets.) In this case, the integration region becomes a hypersurface in phase space, represented schematically in Fig. A-1 by the blue parallelogram. The red dashed sphere represents the zero-bin region and the blue oval is the intersection of the zero-bin region with the hypersurface on which we have restricted the final state particles. The region inside

the blue oval has to be removed by the zero-bin subtraction but there is no need to perform a subtraction outside the hypersurface. This is another way of saying that the zero-bin scaling does not act directly on the phase space constraints that specify the values for the b_k. However, the constraints can be modified indirectly by the momentum-conserving delta functions.

To state the argument more mathematically, consider two ways to perform the phase space integrals over the hypersurface. Either we integrate over all N degrees of freedom and use delta functions to enforce the M constraints or alternatively, we use the constraints to find a set of $N-M$ independent coordinates q_i and integrate over them. The two approaches can be written as

$$\int \prod_{i=1}^{N} \mathrm{d}p_i \prod_{k=1}^{M} \delta(b_k - \hat{b}_k) = \int \prod_{i=1}^{N-M} \mathrm{d}q_i. \tag{A.1}$$

If we use the right hand side of Eq. (A.1) to evaluate the cross section, we can see that the zero-bin scaling will be applied to the integrand but will not affect the phase space constraints $\delta(b_k - \hat{b}_k)$ directly. Similarly, we can apply the phase space constraints required by a jet algorithm so that the integration is performed over a region of phase space. Again, the zero-bin subtraction has to be performed on phase space region specified by the algorithm and the algorithm constraints are only modified by the effect of the zero-bin scaling on the momentum-conserving delta functions.

To give a concrete example, we look at the zero-bin subtraction for the diagrams in Fig. 2-1. The correspondence between the original momentum-conserving delta functions and the associated zero-bin scaled versions is

$$\begin{aligned} \delta\left(Q - p_q^- - p_g^-\right) &\to \delta\left(Q - p_q^-\right) \\ \delta^{d-2}\left(p_q^\perp - p_g^\perp\right) &\to \delta^{d-2}\left(p_q^\perp\right) \\ \delta\left(s/Q - p_q^+ - p_g^+\right) &\to \delta\left(s/Q - p_q^+ - p_g^+\right). \end{aligned} \tag{A.2}$$

Applying these delta functions to the on-shell condition for the quark gives

$$\delta(p_q^- p_q^+ + \left(p_q^\perp\right)^2) \to \delta(Q p_q^+). \tag{A.3}$$

Combining Eqs. (A.2) and (A.3) with the gluon on-shell condition leads to Eq. (2.8), which together with Eq. (2.10) gives Eq. (2.11).

It should be cautioned that performing the zero-bin subtraction as explained above does not give the same result as applying the scaling $p_g \sim Q\lambda^2$ directly to the jet algorithm constraints. In the latter approach, the gluon angle with respect to the jet axis would scale as λ^0 and the theta function would never be satisfied according to power counting since $\delta \sim \lambda$.

Appendix B

Finite Integrals

B.1 1-Jettiness

Here we further study the finite phase-space integrals in Eq. (4.48) that are required for 1-jettiness or e^+e^- 3-jettiness. The indefinite integrals over y can be carried out explicitly. In particular, for I_1 we have

$$G(y,\phi) = \int \frac{\mathrm{d}y}{y} \ln(1 + y^2 - 2y\cos\phi) = -2\mathrm{Re}\big[\mathrm{Li}_2(ye^{\mathrm{i}\phi})\big]\,. \tag{B.1}$$

The remaining integrals over ϕ must be be carried out numerically.[1]

What remains is to determine the ϕ-dependent integration limits on y. We use $-\pi \leq \phi \leq \pi$ as the fundamental region for ϕ. Also recall that $\alpha = \hat{s}_{jm}/\hat{s}_{ij}$ and $\beta = \hat{s}_{im}/\hat{s}_{ij}$, which are positive definite. The θ functions in Eq. (4.48) impose the conditions

$$(y - \cos\phi)^2 + \sin^2\phi \leq \frac{1}{\alpha}\,, \qquad y \geq \sqrt{\frac{\beta}{\alpha}} \geq 0\,, \tag{B.2}$$

which are illustrated in Fig. B-1. Solving for y they imply

$$\begin{aligned} \max\left\{\sqrt{\frac{\beta}{\alpha}},\, y_-(\phi,\alpha)\right\} \leq y \leq y_+(\phi,\alpha)\,, \quad \sin^2\phi \leq \frac{1}{\alpha}\,, \\ y_-(\phi,\alpha) = \cos\phi - \sqrt{1/\alpha - \sin^2\phi}\,, \\ y_+(\phi,\alpha) = \cos\phi + \sqrt{1/\alpha - \sin^2\phi}\,. \end{aligned} \tag{B.3}$$

[1] One could also think about first integrating over ϕ, since the original ϕ-integral can be done and the limits are linear in $\cos\phi$. This does not lead to any simplification, however, because the remaining numerical y-integral will then involve $\arccos[(1 + y^2 - 1/\alpha)/(2y)]$.

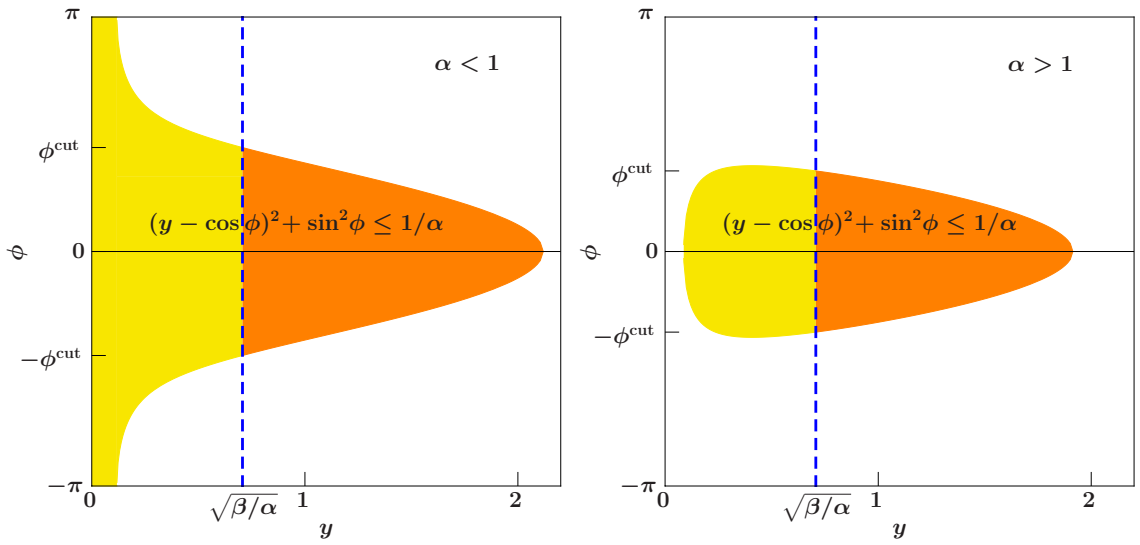

Figure B-1: Phase-space constraints from Eq. (B.3) in the ϕ-y plane for $\alpha = 0.8$ (left) and $\alpha = 1.2$ (right). In both cases $\beta/\alpha = 0.5$.

We can now distinguish the two cases $\alpha \leq 1$ and $\alpha > 1$.

Case $\alpha \leq 1$ For $\alpha \leq 1$, we have $\hat{s}_{jm} \leq \hat{s}_{ij}$, which means that $\hat{q}_j$ is closer to $\hat{q}_m$ than to $\hat{q}_i$. In this case, which is illustrated in the left panel of Fig. B-1, the roots always exist and $y_-(\phi)$ is strictly negative, so we have

$$\begin{aligned} \sqrt{\frac{\beta}{\alpha}} &\leq y \leq y_+(\phi,\alpha)\,, \\ 1 &\geq \cos\phi \geq \max\left\{\frac{\alpha+\beta-1}{2\sqrt{\alpha\beta}}, -1\right\}, \\ \sqrt{\beta} &\leq \sqrt{\alpha}+1\,. \end{aligned} \tag{B.4}$$

The lower limit on $\cos\phi$ is necessary to guarantee that $\sqrt{\beta/\alpha} \leq y_+(\phi,\alpha)$. The condition on α and β is then necessary to guarantee that $1 \geq (\alpha+\beta-1)/(2\sqrt{\alpha\beta})$, such that the lower $\cos\phi$ limit does not exceed the upper one, otherwise the integral vanishes. The lower $\cos\phi$ limit itself is only nontrivial for $\sqrt{\alpha}+\sqrt{\beta} \geq 1$ which means $\sqrt{\hat{s}_{im}}+\sqrt{\hat{s}_{jm}} \geq \sqrt{\hat{s}_{ij}}$. For a purely geometric measure this is always true, but it need not be the case for more general measures.

Case $\alpha > 1$ For $\alpha > 1$, illustrated in the right panel of Fig. B-1, the condition $\sin^2\phi \leq 1/\alpha$ for the roots to exist becomes nontrivial and forces an upper limit on $|\phi|$,

$$|\phi| \leq \arcsin\frac{1}{\sqrt{\alpha}}\,. \tag{B.5}$$

(The second solution for the arcsin is not allowed for $y \geq 0$.) Now, both lower limits on y are possible. To determine which y-limit applies at a given value of ϕ, we can distinguish two cases. First,

$$\begin{aligned}\sqrt{\frac{\beta}{\alpha}} \leq y \leq y_+(\phi,\alpha)\,,&\\ 1 \geq \cos\phi \geq \frac{\alpha+\beta-1}{2\sqrt{\alpha\beta}}\,,&\\ \sqrt{\alpha}-1 \leq \sqrt{\beta} \leq \sqrt{\alpha}+1\,,&\end{aligned} \tag{B.6}$$

where the $\cos\phi$ limits result from enforcing $y_- \leq \sqrt{\beta/\alpha} \leq y_+$ and the conditions on α and β enforce the lower limit on $\cos\phi$ to be ≤ 1. Second,

$$\begin{aligned} y_-(\phi,\alpha) \leq y \leq y_+(\phi,\alpha)\,,&\\ \min\Big\{1,\,\frac{\alpha+\beta-1}{2\sqrt{\alpha\beta}}\Big\} \geq \cos\phi \geq \sqrt{1-\frac{1}{\alpha}}\,,&\\ \beta \leq \alpha - 1\,,&\end{aligned} \tag{B.7}$$

where the upper $\cos\phi$ limit and the condition on α and β arises from requiring $\sqrt{\beta/\alpha} \leq y_-(\phi,\alpha)$, while the lower limit on $\cos\phi$ is equivalent to Eq. (B.5).

Combined Result To write the various conditions in a compact form we define the following two angles

$$\begin{aligned}\phi_{\rm max}(\alpha) &= \arcsin\frac{1}{\sqrt{\alpha}}\,,\\ \phi_{\rm cut}(\alpha,\beta) &= \begin{cases} 0 & |\sqrt{\alpha}-\sqrt{\beta}| \geq 1\,,\\ \pi & \sqrt{\alpha}+\sqrt{\beta} \leq 1\,,\\ \arccos\dfrac{\alpha+\beta-1}{2\sqrt{\alpha\beta}} & \text{otherwise}\,. \end{cases}\end{aligned} \tag{B.8}$$

The conditions for $\alpha < 1$ and the first case for $\alpha > 1$ reduce to $|\phi| \leq \phi_{\text{cut}}$. For the second case for $\alpha > 1$, which only applies for $\beta \leq \alpha - 1$, we have $\phi_{\text{cut}} \leq |\phi| \leq \phi_{\text{max}}$. Using the fact that the integrand is symmetric in ϕ, the final result for the integrals is given by

$$
\begin{aligned}
I_0(\alpha,\beta) &= 2\int_0^{\phi_{\text{cut}}(\alpha,\beta)} \frac{\mathrm{d}\phi}{\pi} \ln\frac{y_+(\phi,\alpha)}{\sqrt{\beta/\alpha}} + 2\theta(\alpha-\beta-1)\int_{\phi_{\text{cut}}(\alpha,\beta)}^{\phi_{\text{max}}(\alpha)} \frac{\mathrm{d}\phi}{\pi}\,\ln\frac{y_+(\phi,\alpha)}{y_-(\phi,\alpha)}\,, \\
I_1(\alpha,\beta) &= 2\int_0^{\phi_{\text{cut}}(\alpha,\beta)} \frac{\mathrm{d}\phi}{\pi} \left[G\big(y_+(\phi,\alpha),\phi\big) - G\big(\sqrt{\beta/\alpha},\phi\big)\right] \\
&\quad + 2\theta(\alpha-\beta-1)\int_{\phi_{\text{cut}}(\alpha,\beta)}^{\phi_{\text{max}}(\alpha)} \frac{\mathrm{d}\phi}{\pi} \left[G\big(y_+(\phi,\alpha),\phi\big) - G\big(y_-(\phi,\alpha),\phi\big)\right].
\end{aligned}
\tag{B.9}
$$

B.2 *N*-Jettiness

We now turn to the integrals $I_{0,1}(\alpha,\beta,\{\alpha_l,\beta_l,\phi_l\})$, defined in Eq. (4.62), that are needed for general N. The y-integral is the same as before and can be carried out explicitly. For a given value of ϕ, the θ functions split the y integration region into a number of mutually exclusive y-intervals, which yields

$$
\begin{aligned}
I_0(\alpha,\beta,\{\alpha_l,\beta_l,\phi_l\}) &= \int_{-\pi}^{\pi}\frac{\mathrm{d}\phi}{\pi}\sum_I \ln\frac{y^I_{\text{max}}(\phi)}{y^I_{\text{min}}(\phi)}\,\theta[y^I_{\text{max}}(\phi)-y^I_{\text{min}}(\phi)]\,, \\
I_1(\alpha,\beta,\{\alpha_l,\beta_l,\phi_l\}) &= \int_{-\pi}^{\pi}\frac{\mathrm{d}\phi}{\pi}\sum_I \big[G(y^I_{\text{max}}(\phi),\phi) - G(y^I_{\text{min}}(\phi),\phi)\big]\,\theta[y^I_{\text{max}}(\phi)-y^I_{\text{min}}(\phi)]\,.
\end{aligned}
\tag{B.10}
$$

Here, the sum runs over all intervals and $y^I_{\text{min}}(\phi)$ and $y^I_{\text{max}}(\phi)$ are the lower and upper limits of the Ith interval, and can depend on all $\alpha,\beta,\alpha_l,\beta_l,\phi_l$.

What remains is to determine the y-limits for a given ϕ. The conditions imposed by the primary θ functions involving α and β are as in the previous subsection. The additional θ functions impose the condition for each l

$$
1-\alpha_l+(1-\beta_l)\,y^2 - 2y\big[\cos\phi - \sqrt{\alpha_l\beta_l}\,\cos(\phi+\phi_l)\big] \leq 0\,. \tag{B.11}
$$

Recall that $\alpha_l = \hat{s}_{jl}/\hat{s}_{jm} \geq 0$ and $\beta_l = \hat{s}_{il}/\hat{s}_{im} \geq 0$. They essentially compare the distance between $\hat{q}_l$ and $\hat{q}_{i,j}$ with the distance between $\hat{q}_m$ and $\hat{q}_{i,j}$. The angle $\phi_l = \phi_{lm}$ is the angle between $\vec{\hat{q}}_{l\perp}$ and $\vec{\hat{q}}_{m\perp}$. The limits on y coming from Eq. (B.11) are given in terms of the

roots of the polynomial,

$$y_{\pm}(\phi,\alpha_l,\beta_l,\phi_l) = \frac{1}{1-\beta_l}\Big\{\cos\phi - \sqrt{\alpha_l\beta_l}\cos(\phi+\phi_l) \\ \pm\sqrt{\left[\cos\phi - \sqrt{\alpha_l\beta_l}\cos(\phi+\phi_l)\right]^2 - (1-\alpha_l)(1-\beta_l)}\Big\}\,. \tag{B.12}$$

To analyze the limits on y imposed by Eq. (B.11) for each l, there are three questions to ask:

1. Does the parabola open upwards or downwards?

2. Does it have real roots?

3. What are the signs of the roots?

The condition for the roots to exist is

$$\left[\cos\phi - \sqrt{\alpha_l\beta_l}\cos(\phi+\phi_l)\right]^2 \geq (1-\alpha_l)(1-\beta_l)\,. \tag{B.13}$$

The correct y limits at a given fixed value of ϕ are then determined as follows:

1. $\beta_l < 1$: The parabola opens upwards, so y must be in between the two roots, $y_- \leq y \leq y_+$.

   (a) $\alpha_l \geq 1$: Equation (B.13) is always satisfied, $y_- \leq 0$, and $y_+ \geq 0$ gives an upper limit

   $$y \leq y_+(\phi,\alpha_l,\beta_l,\phi_l)\,. \tag{B.14}$$

   (b) $\alpha_l < 1$: Equation (B.13) is nontrivial, and the roots have the same sign if they exist. Hence,

   $$y_-(\phi,\alpha_l,\beta_l,\phi_l) \leq y \leq y_+(\phi,\alpha_l,\beta_l,\phi_l)\,, \\ \cos\phi - \sqrt{\alpha_l\beta_l}\cos(\phi+\phi_l) \geq \sqrt{(1-\alpha_l)(1-\beta_l)}\,. \tag{B.15}$$

   The y-integral vanishes if the condition on ϕ is not satisfied.

2. $\beta_l > 1$: The parabola opens downwards, so y must be outside the two roots, $y \leq y_-$ or $y \geq y_+$.

(a) $\alpha_l \leq 1$: Equation (B.13) is always satisfied, $y_- \leq 0$, and $y_+ \geq 0$ gives lower limit

$$y \geq y_+(\phi, \alpha_l, \beta_l, \phi_l)\,. \tag{B.16}$$

(b) $\alpha_l > 1$: Equation (B.13) is nontrivial, and the roots have the same sign if they exist. Hence,

$$\begin{aligned} y \leq y_-(\phi, \alpha_l, \beta_l, \phi_l) \quad \text{or} \quad y \geq y_+(\phi, \alpha_l, \beta_l, \phi_l)\,, \\ \cos\phi - \sqrt{\alpha_l \beta_l}\cos(\phi + \phi_l) \geq \sqrt{(1-\alpha_l)(1-\beta_l)}\,. \end{aligned} \tag{B.17}$$

There are no constraints on y if the condition on ϕ is not satisfied.

3. $\beta_l = 1$: There is no parabola.

(a) $\alpha_l \leq 1$: The limits are

$$\begin{aligned} y \geq \frac{1-\alpha_l}{2\cos\phi - 2\sqrt{\alpha_l}\,\cos(\phi+\phi_l)}\,, \\ \cos\phi \geq \sqrt{\alpha_l}\,\cos(\phi+\phi_l)\,, \end{aligned} \tag{B.18}$$

and the y-integral vanishes if the condition on ϕ is not satisfied.

(b) $\alpha_l > 1$: The limits are

$$\begin{aligned} y \leq \frac{\alpha_l - 1}{2\sqrt{\alpha_l}\,\cos(\phi+\phi_l) - 2\cos\phi}\,, \\ \cos\phi \leq \sqrt{\alpha_l}\,\cos(\phi+\phi_l)\,. \end{aligned} \tag{B.19}$$

There are no constraints on y if the condition on ϕ is not satisfied.

In principle one can now combine all limits and determine all possible ϕ-intervals in which a particular set of lower and upper y-limits applies, as we did in Eq. (B.9). However, although this is straightforward it quickly becomes very cumbersome. Alternatively, it is easy to devise an algorithm to obtain the correct y-limits in Eq. (B.10) for a given value of ϕ in the numerical integration over ϕ. One starts with the y-limits in Eq. (B.3), call them $y_{\min}$ and $y_{\max}$. Next, one loops over all l and determines the limits imposed by each l as above. If one encounters a stronger lower or upper limit, $y_{\min}$ and/or $y_{\max}$ are updated to the new

stronger limit. If one encounters a necessary condition on ϕ that is violated, the integrand vanishes and one can stop. Case 2(b) requires special attention. If it is encountered, the y interval is split in two if necessary and one continues by maintaining two (or more) mutually exclusive y-intervals each having its own lower and upper limit. Newly encountered stronger limits are then applied to each interval. An interval is eliminated whenever its lower limit exceeds its upper limit. If the last existing interval is eliminated the integrand vanishes.

Bibliography

[1] Georges Aad et al. Combined search for the Standard Model Higgs boson using up to 4.9 fb-1 of pp collision data at sqrt(s) = 7 TeV with the ATLAS detector at the LHC. *Phys. Lett.*, B710:49–66, 2012.

[2] Andrea Banfi, Mrinal Dasgupta, Kamel Khelifa-Kerfa, and Simone Marzani. Non-global logarithms and jet algorithms in high-pT jet shapes. *JHEP*, 1008:064, 2010.

[3] Andrea Banfi, Giuseppe Marchesini, and Graham Smye. Away-from-jet energy flow. *JHEP*, 08:006, 2002.

[4] Christian W. Bauer, Sean Fleming, and Michael E. Luke. Summing Sudakov logarithms in B → X/s gamma in effective field theory. *Phys. Rev.*, D63:014006, 2000.

[5] Christian W. Bauer, Sean Fleming, Dan Pirjol, Ira Z. Rothstein, and Iain W. Stewart. Hard scattering factorization from effective field theory. *Phys. Rev.*, D66:014017, 2002.

[6] Christian W. Bauer, Sean Fleming, Dan Pirjol, and Iain W. Stewart. An effective field theory for collinear and soft gluons: Heavy to light decays. *Phys. Rev.*, D63:114020, 2001.

[7] Christian W. Bauer, Andrew Hornig, and Frank J. Tackmann. Factorization for generic jet production. *Phys. Rev.*, D79:114013, 2009.

[8] Christian W. Bauer, Christopher Lee, Aneesh V. Manohar, and Mark B. Wise. Enhanced nonperturbative effects in Z decays to hadrons. *Phys. Rev.*, D70:034014, 2004.

[9] Christian W. Bauer and Aneesh V. Manohar. Shape function effects in B → X/s gamma and B → X/u l nu decays. *Phys. Rev.*, D70:034024, 2004.

[10] Christian W. Bauer, Aneesh V. Manohar, and Mark B. Wise. Enhanced nonperturbative effects in jet distributions. *Phys. Rev. Lett.*, 91:122001, 2003.

[11] Christian W. Bauer, Dan Pirjol, and Iain W. Stewart. Soft-Collinear Factorization in Effective Field Theory. *Phys. Rev.*, D65:054022, 2002.

[12] Christian W. Bauer and Iain W. Stewart. Invariant operators in collinear effective theory. *Phys. Lett.*, B516:134–142, 2001.

[13] Thomas Becher and Guido Bell. The gluon jet function at two-loop order. *Phys. Lett.*, B695:252–258, 2011.

[14] Thomas Becher and Matthias Neubert. Toward a NNLO calculation of the anti-B $\to$ X/s + gamma decay rate with a cut on photon energy. II: Two-loop result for the jet function. *Phys. Lett.*, B637:251–259, 2006.

[15] Thomas Becher and Matthias Neubert. Infrared singularities of scattering amplitudes in perturbative QCD. *Phys. Rev. Lett.*, 102:162001, 2009.

[16] Thomas Becher and Matthias Neubert. On the Structure of Infrared Singularities of Gauge-Theory Amplitudes. *JHEP*, 06:081, 2009.

[17] Carola F. Berger, Claudio Marcantonini, Iain W. Stewart, Frank J. Tackmann, and Wouter J. Waalewijn. Higgs Production with a Central Jet Veto at NNLL+NNLO. *JHEP*, 1104:092, 2011.

[18] Geoffrey T. Bodwin. Factorization of the Drell-Yan Cross-Section in Perturbation Theory. *Phys. Rev.*, D31:2616, 1985. Revised version.

[19] Matteo Cacciari, Gavin P. Salam, and Gregory Soyez. The Anti-k(t) jet clustering algorithm. *JHEP*, 0804:063, 2008.

[20] Robert Cahn and Gerson Goldhaber. *The Experimental Foundations of Particle Physics*. Cambridge University Press, 2009.

[21] Serguei Chatrchyan et al. Combined results of searches for the standard model Higgs boson in pp collisions at sqrt(s) = 7 TeV. CMS-HIG-11-032, 2012.

[22] William Man-Yin Cheung, Michael Luke, and Saba Zuberi. Phase Space and Jet Definitions in SCET. *Phys. Rev.*, D80:114021, 2009.

[23] Jui-yu Chiu, Randall Kelley, and Aneesh V. Manohar. Electroweak Corrections using Effective Field Theory: Applications to the LHC. *Phys. Rev.*, D78:073006, 2008.

[24] John C. Collins, Davison E. Soper, and George Sterman. Soft gluons and factorization. *Nucl. Phys.*, B308:833, 1988.

[25] John C. Collins, Davison E. Soper, and George F. Sterman. Factorization for Short Distance Hadron - Hadron Scattering. *Nucl. Phys.*, B261:104, 1985.

[26] Mrinal Dasgupta and Gavin P. Salam. Resummation of non-global QCD observables. *Phys. Lett. B*, 512:323–330, 2001.

[27] Lance J. Dixon, Einan Gardi, and Lorenzo Magnea. On soft singularities at three loops and beyond. *JHEP*, 02:081, 2010.

[28] Yu. L. Dokshitzer and G. Marchesini. On large angle multiple gluon radiation. *JHEP*, 03:040, 2003.

[29] Stephen D. Ellis, Andrew Hornig, Christopher Lee, Christopher K. Vermilion, and Jonathan R. Walsh. Consistent Factorization of Jet Observables in Exclusive Multijet Cross-Sections. *Phys. Lett.*, B689:82–89, 2010.

[30] Stephen D. Ellis, Christopher K. Vermilion, Jonathan R. Walsh, Andrew Hornig, and Christopher Lee. Jet Shapes and Jet Algorithms in SCET. *JHEP*, 11:101, 2010.

[31] CMS Experiment. CMS collision events: 7 TeV collisions. Apr 2010.

[32] CMS Experiment. CMS collision events: 7 TeV multi-jet event. Jul 2011.

[33] Sean Fleming, Andre H. Hoang, Sonny Mantry, and Iain W. Stewart. Jets from Massive Unstable Particles: Top-Mass Determination. *Phys. Rev.*, D77:074010, 2008.

[34] Sean Fleming, Andre H. Hoang, Sonny Mantry, and Iain W. Stewart. Top Jets in the Peak Region: Factorization Analysis with NLL Resummation. *Phys. Rev.*, D77:114003, 2008.

[35] Sean Fleming, Adam K. Leibovich, and Thomas Mehen. Resummation of Large Endpoint Corrections to Color-Octet J/ψ Photoproduction. *Phys. Rev. D*, 74:114004, 2006.

[36] Einan Gardi and Lorenzo Magnea. Factorization constraints for soft anomalous dimensions in QCD scattering amplitudes. *JHEP*, 03:079, 2009.

[37] David Griffiths. *Introduction to Elementary Particles*. Wiley-VCH, 2008.

[38] Andrew Hornig, Christopher Lee, and Grigory Ovanesyan. Effective Predictions of Event Shapes: Factorized, Resummed, and Gapped Angularity Distributions. *JHEP*, 05:122, 2009.

[39] Teppo T. Jouttenus. Jet Function with a Jet Algorithm in SCET. *Phys. Rev.*, D81:094017, 2010.

[40] Teppo T. Jouttenus, Iain W. Stewart, Frank J. Tackmann, and Wouter J. Waalewijn. The Soft Function for Exclusive N-Jet Production at Hadron Colliders. *Phys. Rev.*, D83:114030, 2011.

[41] Gregory P. Korchemsky and Anatoly V. Radyushkin. Renormalization of the Wilson Loops Beyond the Leading Order. *Nucl. Phys.*, B283:342–364, 1987.

[42] Gregory P. Korchemsky and George F. Sterman. Power corrections to event shapes and factorization. *Nucl.Phys.*, B555:335–351, 1999.

[43] Zoltan Ligeti, Iain W. Stewart, and Frank J. Tackmann. Treating the b quark distribution function with reliable uncertainties. *Phys. Rev.*, D78:114014, 2008.

[44] Aneesh V. Manohar and Iain W. Stewart. The zero-bin and mode factorization in quantum field theory. *Phys. Rev.*, D76:074002, 2007.

[45] Sonny Mantry and Frank Petriello. Factorization and Resummation of Higgs Boson Differential Distributions in Soft-Collinear Effective Theory. *Phys.Rev.*, D81:093007, 2010.

[46] A.D. Martin, W.J. Stirling, R.S. Thorne, and G. Watt. Uncertainties on alpha(S) in global PDF analyses and implications for predicted hadronic cross sections. *Eur.Phys.J.*, C64:653–680, 2009.

[47] S. Mert Aybat, Lance J. Dixon, and George Sterman. The two-loop soft anomalous dimension matrix and resummation at next-to-next-to leading pole. *Phys. Rev.*, D74:074004, 2006.

[48] Tevatron New Phenomena and Higgs Working Group. Combined CDF and D0 Search for Standard Model Higgs Boson Production with up to 10.0 fb-1 of Data. FERMILAB-CONF-12-065-E, 2012.

[49] Gavin P. Salam and Gregory Soyez. A Practical Seedless Infrared-Safe Cone jet algorithm. *JHEP*, 0705:086, 2007.

[50] Carl R. Schmidt. H $\rightarrow$ g g g (g q anti-q) at two loops in the large M(t) limit. *Phys. Lett.*, B413:391–395, 1997.

[51] Matthew D. Schwartz. Resummation and NLO Matching of Event Shapes with Effective Field Theory. *Phys. Rev.*, D77:014026, 2008.

[52] George Sterman and Steven Weinberg. Jets from Quantum Chromodynamics. *Phys. Rev. Lett.*, 39:1436, 1977.

[53] Paul M. Stevenson. Comments on Sterman-Weinberg jet formula. *Phys. Lett.*, B78:451, 1978.

[54] Iain W. Stewart, Frank J. Tackmann, and Wouter J. Waalewijn. Factorization at the LHC: From PDFs to Initial State Jets. *Phys. Rev.*, D81:094035, 2010.

[55] Iain W. Stewart, Frank J. Tackmann, and Wouter J. Waalewijn. N-Jettiness: An Inclusive Event Shape to Veto Jets. *Phys. Rev. Lett.*, 105:092002, 2010.

[56] Iain W. Stewart, Frank J. Tackmann, and Wouter J. Waalewijn. The Quark Beam Function at NNLL. *JHEP*, 09:005, 2010.

[57] Iain W. Stewart, Frank J. Tackmann, and Wouter J. Waalewijn. The Beam Thrust Cross Section for Drell-Yan at NNLL Order. *Phys. Rev. Lett.*, 106:032001, 2011.

[58] Jesse Thaler and Ken Van Tilburg. Maximizing Boosted Top Identification by Minimizing N-subjettiness. *JHEP*, 1202:093, 2012.

[59] Michael Trott. Jets in effective theory: Summing phase space logs. *Phys. Rev.*, D75:054011, 2007.

[60] Frank Wilczek. *Fantastic Realities: 49 Mind Journeys and A Trip to Stockholm.* World Scientific, 2006.